공학박사학위논문

Synthesis and Modification of Fluorinated Polymers and Their Application to Bio-medical, Membrane, and Coating Materials

불소계 고분자의 합성 및 개질 그리고 바이오-메디컬, 분리막, 및 코팅재료로의 응용

2023년 2월

서울대학교 대학원

화학생물공학부

한 동 제

불소계 고분자의 합성 및 개질 그리고

바이오-메디컬, 분리막, 및 코팅재료로의 응용

Synthesis and Modification of Fluorinated Polymers and Their Application to Bio-medical, Membrane, and Coating Materials

지도교수 이 종 찬 박사

이 논문을 공학박사학위 논문으로 제출함.

2023년 2월

서울대학교 대학원

화학생물공학부

한 동 제

한동제의 박사학위논문을 인준함.

2023년 2월

위원장	오 준 학	(인)
부위원장	이 종 찬	(인)
위 원	유 동 원	(인)
위 원	김 태 호	(인)
위 원	손 은 호	(인)

Synthesis and Modification of Fluorinated Polymers and Their Application to Bio-medical, Membrane, and Coating Materials

by

Dong Je Han

Adviser: Professor Jong-Chan Lee, Ph. D.

Submitted in Partial Fulfillment

of the Requirements for the Degree of

DOCTOR OF PHILOSOPHY

February, 2023

School of Chemical and Biological Engineering

College of Engineering

Graduate School

Seoul National University

Abstract

This study presents synthesis and modification of fluorinated polymers and their application to bio-medical, membrane, and coating materials. Firstly, perfluorinated methacrylates with short side groups (−$CF_2CF_2CF_3$, −CF_2CF_3, and −CF_3) are grafted onto poly(vinylidene fluoride-co-chlorotrifluoroethylene) (P(VDF-CTFE)) by single step atom transfer radical polymerization (ATRP). Depending on the fluorinated side groups, the surface energies of the graft copolymers are controlled in the range of 11.1−18.7 mN m^{-1}. With the albumin pretreatment strategy, the graft copolymer with the lowest surface energy (with −$CF_2CF_2CF_3$) showed the lowest fibrinogen adsorption of 5.6 ng cm^{-2}. This indicates that the graft copolymer is suitable for blood-contacting devices since fibrinogen adhesion induces blood coagulation. Also, its blood compatibility was further corroborated by platelet adhesion tests.

Secondly, quaternary ammonium grafted (PVDF-QDMA) and quaternary pyridinium grafted PVDF (PVDF-Q4VP) were synthesized by grafting cationic monomers onto P(VDF-CTFE). Owing to antimicrobial cationic groups, resulting polymers could effectively kill gram-positive *S. aureus*, gram-negative *E. coli*, and the pathogenic yeast *C. albicans* (antimicrobial rates > 99.99%). For efficient utilization from an economical perspective, the cationic polymers were

strategically blended with PVDF. Despite the small contents of the cationic polymers (i.e., 1 and 5 wt%), blend films exhibited notable antimicrobial performances. Furthermore, their mechanical properties and biocompatibility is superior to or comparable with pristine PVDF film.

Thirdly, two different PVDF-based ionic polymers which contains only cationic part (PVDF-QDMA) or zwitterionic-co-cationic part (PVDF-MPC/QDMA) were synthesized by ATRP. 5 wt% or 10 wt% of synthetic polymers were blended with PVDF and were fabricated into PVDF blend membranes via non-solvent induced separation. The physicochemical properties of membranes such as morphology, wettability, and surface charge were firstly investigated, and then the investigation was continued focusing on antifouling and bactericidal properties. In consequence, the interplay between the biofouling mitigation and the influence of the ionic groups on blend membranes were correlated. Among the membranes, the membrane with 10 wt% of PVDF-MPC/QDMA exhibits superb properties in terms of both antifouling (FRR ~100%) and bactericidal properties (>99.9%).

Fourthly, P(VDF-CTFE) is functionalized with various thiols in effort to introduce the functionality onto VDF-based fluoropolymer. Using tertiary amines as the sole catalyst, various functional groups (hydroxyl, alkyl, aryl, sulfonate, carboxyl, amino and perfluorinated group) are introduced via facile one-pot reaction. Internal double bond formation and consecutive thiol-Michael addition,

and nucleophilic substitution to halogens are simultaneously observed. Careful adjustment of reaction conditions over the reagent input, time, and solvent reveals the controllability and versatility of this reaction. Furthermore, the film properties of functionalized fluoropolymers were investigated.

Finally, the nonafluoro-tert-butyl (NFtB) group was incorporated into the methacrylic backbone and its influence was examined. Copolymers of methyl methacrylate and 2-hydroxyethyl methacrylate were used as substrate polymer and they were fluorinated by nonafluoro-tert-butanol. The developed fluorination could be performed under mild conditions, and the content of NFtB groups was controlled by adjustment of the monomeric ratio. It was found that the surface composition, intermolecular distances, and mechanical properties of polymer films were profoundly affected by fluorination. In other words, fluorinated films exhibited outstanding mechanical property, high optical transparency, and low surface energy while preserving the solubility in common solvents.

Keywords: Fluorinated polymer, Graft copolymer, Poly(vinylidene fluoride) (PVDF), Blood compatibility, Antimicrobial property, Water treatment membrane, Functionalization, Surface property

Student Number: 2017-29807

Table of Contents

Chapter 1

Introduction

Chapter 2

Fluorinated Methacrylate-Grafted P(VDF-CTFE) and Albumin Layers for Reducing Fibrinogen Adsorption

Chapter 3

Poly(vinylidene fluoride)-Based Film with Strong Antimicrobial Activity

Chapter 4

Design of an ionic PVDF-based additive for PVDF water purification membranes with anti-fouling and bactericidal activities

Chapter 5

Versatile Functionalization of Fluoropolymer via One-pot Thiol Incorporation

Chapter 6

Access to Fluorinated Polymer Surfaces with Outstanding Mechanical Property, High Optical Transparency, and Low Surface Energy via Nonafluoro-*tert*-Butyl Group

Introduction

List of Tables

List of Figures

Chapter 1

Introduction

1.1. Fluorinated polymers

After the discovery of the polytetrafluoroethylene by Dr. Plunkett in 1938,[1] fluorinated polymers have been of interest as a special class of materials. Specialty of these polymers are originated from peculiar properties of fluorine atom: the highest electronegativity (4.0), the lowest polarizability, and small atomic radius (1.32Å).[2] These features make the C–F bond the strongest single bond (bond dissociation energy ~ 485 kJ mol^{-1}) in organic chemistry.[3] Benefiting from the high stability of the C-F bond, fluorine-containing polymers show excellent thermal stability, chemical inertness, and weatherability. Furthermore, low refractive index and low surface energy are observed in this class of materials due to the small polarizability of fluorine.[4,5]

Fluorinated polymers include perfluorinated polymers and semi-fluorinated polymers,[6,7] which are divided into two main categories according to their molecular structure: i) fluorinated groups are located in the polymer backbone, ii) fluorinated groups are located in the side chain. Generally, the former is synthesized by the polymerization of fluoroalkenes such as tetrafluoroethylene, vinylidene fluoride, and hexafluoropropylene, and the latter is usually synthesized by the polymerization of fluorinated (meth)acrylates.[2,8,9] Although their properties vary according to the molecular structure and composition, fluorinated

polymers are regarded as irreplaceable owing to their distinctive combination of properties, finding suitable applications in various field such as everyday goods,[4] outdoor coating,[10] fiber,[11] coating,[12] automotive,[13] fuel cell,[14] rechargeable battery,[16] and energy harvesting.[17]

1.2. Synthesis and modification of fluorinated polymers

Fluorine-based polymers are known to exhibit fascinating properties such as excellent thermal stability, chemical inertness, low dielectric constant, and low surface energy. From the other side of view, however, these characteristics cause ineluctable disadvantages like poor processibility, low miscibility, and difficulty in tuning the properties for on-demand applications.[7,17] Therefore, to compensate for the ascribed drawbacks or broaden the field of use, various studies for preparing novel fluorinated polymers with desired properties have been conducted.

One approach is the utilization of functional co-monomers and copolymerization with fluorinated monomers. Since copolymerization is a common approach in the field of polymer chemistry owing to its facileness and economic benefits, various copolymers containing fluoroalkenes or fluorinated acrylates have been reported. [18–20] However, restricted scope of co-monomers is depicted as a problem owing to the distinct reactivity ratio of fluorinated monomers.[6,21]

Second approach is fluorination of common polymers using direct fluorination agents such as F_2 and HF [22,23] or fluoro-functionalization via introduction of fluorinated groups.[24,25] Direct fluorination is known to be very effective because it can easily fluorinate common organic compounds. However, the use of direct fluorination agents may not be recommended as they cause toxicity and

environmental concerns.[26,27] In contrast, fluoro-functionalization has many advantages of mild reaction conditions, wide applicability, and control of functionality.[21,25] Nevertheless, it still needs to overcome obstacles which caused from the complex procedure and limited type of fluorinated moieties.[28]

Third approach is modification of commercial fluoropolymers by chemical pathway. This approach broaden the scope of introducible functionality and also offers the advantages of facile synthetic process and economic affordability.[21] Therefore, this method has been widely utilized to prepare the on-demand polymers while retaining their original properties.[29] Numerous methods have been used, among which graft modification using atom transfer radical polymerization (ATRP) has received attention since the report by Hester *et. al*.[30] Because various fluoropolymers can be involved, this approach have been widely employed to prepare functional fluoropolymers.[31,32] Nevertheless, immanent disadvantages make this process uncompetitive: sensitive reaction conditions, ambiguous mechanism, and residual catalyst.[21,33] Besides ATRP, the utilization of nucleophiles is being studied as a promising strategy. In this method, nucleophiles are introduced into the fluoropolymer backbone, which have been frequently used to crosslink fluoropolymers.[34,35] However, since the nucleophile can causes dehydrofluorination [33] and multi-step is sometimes required,[36] a facile and mild reaction routes need to be further studied.

1.3. Motivation

Although fluorine-based polymers are currently utilized in various fields, appropriate improvements are required to further enhance their performance or broaden the field of use. Based on the understanding of their distinctive features, we designed novel fluorinated polymers for various applications. To meet the requirements of each application, on-demand properties such as blood compatibility, wettability, bactericidal activity, antifouling property, and mechanical integrity were incorporated into fluorinated polymers by a single step reaction.

Firstly, fluorinated methacrylates with short side chains are grafted onto poly(vinylidene fluoride-co-chlorotrifluoroethylene) (P(VDF-CTFE)) by ATRP. By grafting polymerization, two different fluorinated polymers (i.e., backbone fluorinated, and side chain fluorinated polymer) were integrated to tune the surface wettability, and applied to the blood compatible surfaces through appropriate pretreatment. Secondly, antimicrobial properties were incorporated into the PVDF-based polymer for the application in the medical and healthcare fields. For the above purpose, cationic monomers were grafted via ATRP method, and PVDF-based cationic copolymers were successfully synthesized. Resulting copolymers exhibited excellent biocidal properties, and it was also confirmed that

the resulting polymers exhibited significant antimicrobial properties even when blended with PVDF homopolymer. Thirdly, to improve the biofouling properties of PVDF water treatment membranes, the PVDF-based ionic polymer which contains zwitterionic-co-cationic parts were synthesized and utilized as membrane additives. Benefiting from the enhanced hydrophilicity and neutral surface charge, fabricated membrane show superb biofouling repellency, and the interplay between the biofouling mitigation properties and the ionic groups on membranes were discussed. Fourthly, to compensate for the innate disadvantages of ATRP, novel fluoropolymers were prepared by thiol-Michael reaction. Via facile one-pot reaction under mild condition, various functional groups (i.e., hydroxyl, alkyl, aryl, sulfonate, carboxyl, amino, and perfluorinated group) were introduced into P(VDF-CTFE) substrate. Multiple reactions such as internal double bond formation, thiol-Michael addition, and nucleophilic substitution occur consecutively or independently, and are involved in the functionalization of fluoropolymers. Finally, the nonafluoro-tert-butyl (NFtB) group was incorporated into the non-fluorinated methacrylic backbone. The proposed fluorination pathway is a method that can easily and effectively make fluorinated polymers under mild conditions.

1.4. References

[1] R.J. Plunkett, The history of polytetrafluoroethylene: discovery and development, *High Performance Polymers: Their Origin and Development*, 1986.

[2] B. Ameduri, Fluoropolymers: The Right Material for the Right Applications, *Chem. - A Eur. J.*, 2018, *24*, 18830–18841.

[3] J. Lv, Y. Cheng, Fluoropolymers in biomedical applications: State-of-the-art and future perspectives, *Chem. Soc. Rev.*, 2021, *50*, 5435–5467.

[4] J. Gardiner, Fluoropolymers: Origin, Production, and Industrial and Commercial Applications, *Aust. J. Chem,.* 2015, *68*, 13–22.

[5] R. Koguchi, K. Jankova, M. Tanaka, Fluorine-containing bio-inert polymers: Roles of intermediate water, *Acta Biomater.,* 2022, *138*, 34–56.

[6] A. Hirao, K. Sugiyama, H. Yokoyama, Precise synthesis and surface structures of architectural per- and semifluorinated polymers with well-defined structures, *Prog. Polym. Sci.,* 2007, *32*, 1393–1438.

[7] W. Yao, Y. Li, X. Huang, Fluorinated poly(meth)acrylate: Synthesis and properties, *Polymer*, 2014, *55*, 6197–6211.

[8] B. Améduri, The Promising Future of Fluoropolymers, *Macromol. Chem. Phys.*, 2020, *221,* 1–14.

[9] H. Teng, Overview of the development of the fluoropolymer industry, *Appl.*

Sci., 2012, *2*, 496–512.

[10] I. Karapanagiotis, P.N. Manoudis, Superhydrophobic and superamphiphobic materials for the conservation of natural stone: An overview, *Constr. Build. Mater.,* 2022, *320*, 126175.

[11] K.E. Perepelkin, Fluoropolymer Fibres: Physicochemical Nature and Structural Dependence of their Unique Properties, Fabrication, and Use. A Review, *Fibre Chemisty*, 2004, *36*, 43–58.

[12] P. Kianfar, R. Bongiovanni, B. Ameduri, A. Vitale, Electrospinning of Fluorinated Polymers: Current State of the Art on Processes and Applications, *Polym. Rev.*, 2022, 1–73.

[13] B. Améduri, B. Boutevin, G. Kostov, Fluoroelastomers: Synthesis, properties and applications, *Prog. Polym. Sci.*, 2001, *26*, 105–187.

[14] K.A. Mauritz, R.B. Moore, State of understanding of Nafion, *Chem. Rev.,* 2004, *104*, 4535–4585.

[15] Y. Wu, Y. Li, Y. Wang, Q. Liu, Q. Chen, M. Chen, Advances and prospects of PVDF based polymer electrolytes, *J. Energy Chem.*, 2022, *64*, 62–84.

[16] N.A. Shepelin, A.M. Glushenkov, V.C. Lussini, P.J. Fox, G.W. Dicinoski, J.G. Shapter, A. V. Ellis, New developments in composites, copolymer technologies and processing techniques for flexible fluoropolymer piezoelectric generators for efficient energy harvesting, *Energy Environ. Sci*., 2019, *12*, 1143–1176.

[17] B. Ameduri, From vinylidene fluoride (VDF) to the applications of VDF-Containing polymers and copolymers: Recent developments and future trends, *Chem. Rev.,* 2009, *109*, 6632–6686.

[18] T. Soulestin, V. Ladmiral, F.D. Dos Santos, B. Améduri, Vinylidene fluoride- and trifluoroethylene-containing fluorinated electroactive copolymers. How does chemistry impact properties?, *Prog. Polym. Sci.,* 2017, *72*, 16–60.

[19] Y. Patil, B. Ameduri, Advances in the (co)polymerization of alkyl 2-trifluoromethacrylates and 2-(trifluoromethyl)acrylic acid, *Prog. Polym. Sci.,* 2013, *38*, 703–739.

[20] Y. Zhang, A. Takahara, Synthesis and surface properties of amphiphilic copolymer consisting of hydrophobic perfluorocarbon and hydrophilic zwitterionic blocks, *Polymer*, 2021, *230*, 124029.

[21] S. Tan, J. Li, G. Gao, H. Li, Z. Zhang, Synthesis of fluoropolymer containing tunable unsaturation by a controlled dehydrochlorination of P(VDF-co-CTFE) and its curing for high performance rubber applications, *J. Mater. Chem*., 2012, *22*, 18496–18504.

[22] J.H. Lee, K.H. Kim, M. Choi, J. Jeon, H.J. Yoon, J. Choi, Y.S. Lee, M. Lee, J.J. Wie, Rational molecular design of polymeric materials toward efficient triboelectric energy harvesting, *Nano Energy*, 2019, *66*, 104158.

[23] T. Fuchigami, S. Inagi, Recent Advances in Electrochemical Systems for

Selective Fluorination of Organic Compounds, *Acc. Chem. Res*., 2020, *53*, 322–334

[24] J.S. Chung, B.G. Kim, E.H. Sohn, J.C. Lee, Molecular structure and surface properties of comb-like fluorinated poly(oxyethylene)s having different content of fluoroalkyl side group, *Macromolecules*, 2010, *43*, 10481–10489.

[25] Y. Ogura, M. Takenaka, M. Sawamoto, T. Terashima, Fluorous Gradient Copolymers via in-Situ Transesterification of a Perfluoromethacrylate in Tandem Living Radical Polymerization: Precision Synthesis and Physical Properties, *Macromolecules*, 2018, *51*, 864–871.

[26] J.J. Reisinger, M.A. Hillmyer, Synthesis of fluorinated polymers by chemical modification, *Prog. Polym. Sci.,* 2002, *27*, 971–1005.

[27] Y. Dong, Z. Wang, C. Li, Controlled radical fluorination of poly(meth)acrylic acids in aqueous solution, *Nat. Commun*., 2017, *8*, 1–5.

[28] E.H. Discekici, A. Anastasaki, R. Kaminker, J. Willenbacher, N.P. Truong, C. Fleischmann, B. Oschmann, D.J. Lunn, J. Read De Alaniz, T.P. Davis, C.M. Bates, C.J. Hawker, Light-Mediated Atom Transfer Radical Polymerization of Semi-Fluorinated (Meth)acrylates: Facile Access to Functional Materials, *J. Am. Chem. Soc*., 2017, *139*, 5939–5945.

[29] B. Peng, J. Wang, M. Li, M. Wang, S. Tan, Z. Zhang, Activation of different C-F bonds in fluoropolymers for Cu(0)-mediated single electron transfer radical

polymerization, *Polym. Chem.,* 2021, *12*, 3132–3141.

[30] J.F. Hester, P. Banerjee, Y.Y. Won, A. Akthakul, M.H. Acar, A.M. Mayes, ATRP of amphiphilic graft copolymers based on PVDF and their use as membrane additives, *Macromolecules,* 2002, *35*, 7652–7661.

[31] S.A. Mohammad, S. Shingdilwar, S. Banerjee, B. Ameduri, Macromolecular engineering approach for the preparation of new architectures from fluorinated olefins and their applications, *Prog. Polym. Sci.,* 2020, *106*, 101255.

[32] J. Dai, Y. Dong, C. Yu, Y. Liu, X. Teng, A novel Nafion-g-PSBMA membrane prepared by grafting zwitterionic SBMA onto Nafion via SI-ATRP for vanadium redox flow battery application, *J. Membr. Sci.*, 2018, *554*, 324–330.

[33] M. Guerre, M. Semsarilar, V. Ladmiral, Grafting from Fluoropolymers Using ATRP: What is Missing?, *Eur. J. Inorg. Chem*., 2022, e202100945.

[34] A. Taguet, B. Ameduri, B. Boutevin, Crosslinking of vinylidene fluoride-containing fluoropolymers, *Adv. Polym. Sci.,* 2005, *184*, 127–211.

[35] D. Zou, Y.M. Lee, Design strategy of poly(vinylidene fluoride) membranes for water treatment, *Prog. Polym. Sci*., 2022, *128*, 101535.

[36] J. Sierke, A. V. Ellis, Cross-linking of dehydrofluorinated PVDF membranes with thiol modified polyhedral oligomeric silsesquioxane (POSS) and pure water flux analysis, *J. Membr. Sci.,* 2019, *581*, 362–372.

Chapter 2

Fluorinated Methacrylate-Grafted P(VDF-CTFE) and Albumin Layers for Reducing Fibrinogen Adsorption

2.1. Introduction

With an increase in the population of elderly people, the prevalence of cardiovascular and kidney diseases has rapidly increased,[1-3] leading to an upsurge in the demand for blood-contacting medical devices such as extracorporeal membrane oxygenator (ECMO) and hemodialysis equipment. Consequently, the performance of blood-contacting materials has become a serious issue.[4, 5] Commercially available polymers like polytetrafluoroethylene (PTFE),[6] polyureathanes (PU),[7] and polyethylene terephthalate (PET) [8] are the most widely used for blood-contacting materials. However, they are still faced with serious problems caused by blood-material interaction which can aggravate the performance of the devices, eventually endangering the patient's life.

Non-specific protein adsorption is considered a critical factor that triggers blood coagulation at the material surface.[9-11] Among the many proteins in plasma, fibrinogen attracts more attention than the abundant albumin (60%) and globulin (35%) despite its lower concentration (4%) [12] because it plays a crucial role in blood clotting by mediating platelets and triggering the coagulation cascade. It has been reported that even 10 ng cm^{-2} of fibrinogen adsorption on a material surface can coagulate whole blood. Hence, the fibrinogen adsorption

behavior has been extensively studied to develop a long lasting blood-compatible material.[13-15]

Over the decades, some progresses have been reported in the development of blood-compatible materials. One of the most popular approaches is utilization of hydrophilic polymers, such as poly(ethylene glycol) (PEG) [16-19] and zwitterionic polymers,[20-23] as they can disturb protein adsorption by the water barrier on their surfaces.[15, 24] However, these materials have some limitations such as their unstable behaviors under water (i.e., oxidative degradation) and higher sensitivity to pH, ionic strength, and temperature.[5, 25] Even though hydrophobic materials have been suggested to overcome these limitations, some studies reported that hydrophobic-hydrophobic interactions facilitate protein adsorption on surfaces under aqueous conditions.[26-29] Therefore, hydrophobic materials have limited applications for inhibiting protein adsorption despite their high demands in biomedical device industry.[13, 30]

Some fluorinated polymers are known to have good blood compatibility.[31-33] Among them, poly(vinylidene fluoride) (PVDF) and its copolymers have been used in biomedical applications such as surgical meshes [34] and dressing matrices [35] owing to its biocompatible characteristic as well as their outstanding physical properties. In spite of these advantages, the use of PVDF in blood-contacting devices remains challenging because of its inherent

hydrophobicity.[36-38] In this study, however, the highly hydrophobic PVDF-based polymers were strategically designed to create blood-inert surfaces by pre-occupations of albumin layer on the surfaces. Poly(vinylidene fluoride-co-chlorotrifluoroethylene) (P(VDF-CTFE)) was selected as the starting material because of the convenience of modification with the hydrophobic poly(fluorinated methacrylates) (PFMMA), by atom transfer radical polymerization (ATRP). The protein adsorption properties of the modified P(VDF-CTFE) were precisely estimated and the results were correlated with their surface properties. This study presents an effective strategy for the development of blood-contacting devices with enhanced blood-compatibility.

2.2. Experimental

Materials

2,2,2-Trifluoroethyl methacrylate (TFEMA; 98%), 2,2,3,3,3-pentafluoropropyl methacrylate (PFPMA; 97%), and 2,2,3,3,4,4,4-heptafluorobutyl methacrylate (HFBMA; 97%) were purchased from Alfa Aesar. Tetrahydrofuran (THF; 99.9%), α,α,α-trifluorotoluene (99%), Cu(I)Cl (99.99 %), 2,2'-bipyridine (BPy; 99 %), *N*-methylpyrrolidinone (NMP), acetone-d_6 (99.9%), phosphate buffer saline (PBS) tablets, PMMA (M_w = 120,000), bovine serum albumin (BSA), basic alumina, fibrinogen from human plasma, and glutaraldehyde solution (Grade I) were purchased from Sigma-Aldrich. All the chemicals were used as received without further purification. All aqueous solutions were prepared with Milli-Q purified water (Millipore) with a resistivity of 18.2 MΩ cm.

Preparation of P(VDF-CTFE) and graft copolymers

Ultrapure water (400 g) and 1.17 g of ammonium perfluorooctanoate (APFO) were introduced into a 1 L jacketed stainless steel autoclave at ambient temperature. After closing and deaerating the reactor, mechanical stirring was initiated, and the reactor was heated to 82 °C. Then, the reactor was pressurized to

19.6 atm with a VDF/CTFE gas mixture (75:25 mole ratio). The polymerization reaction was started by injecting an initiator solution that consisted of 0.93 g of sodium persulfate ($Na_2S_2O_8$, Sigma-Aldrich) and 100 g of ultrapure water. The pressure was maintained at 19.6 bar by continuously feeding the gas mixture. After introducing 250 g of the VDF/CTFE gas mixture, the monomer feed was stopped, and the pressure was evacuated. The resulting P(VDF-CTFE) had a composition of 73:27 mol%. Graft copolymers were synthesized by ATRP with P(VDF-CTFE) used as macroinitiator. First, 1 g of P(VDF-CTFE) containing 3.45 mM of chlorine was dissolved in 30 mL of NMP at 25 °C, and the solution was stirred at 50 °C under vacuum for 60 min. Then, 25 mM of monomer (TFEMA, PFPMA, or HFBMA) and copper catalyst (CuCl, 1.8 mM) were introduced. After a few vacuum-nitrogen cycles, 2.5 mM of bipyridine was added to the solution. The reaction vessel was then transferred to a 90 °C preheated reactor and the reaction was carried out under a nitrogen atmosphere. After 24 h, the polymerization was stopped by cooling to room temperature and adding a few drops of methanol. The resulting solution was diluted with acetone and passed through basic alumina to remove the copper catalyst, followed by precipitation in water. The precipitate was further purified by re-dissolving in THF and re-precipitating in water. The resulting graft copolymer was washed with methanol and dried for 48 h at 50 °C under reduced pressure.

Polymer Characterization

NMR spectra were obtained using a Bruker AVANCE 500 MHz NMR spectrometer with acetone-d_6 as the solvent and the chemical shifts reported in ppm relative to that of TMS used as an internal standard. All spectra were recorded at room temperature. The molecular weights and molecular weight distributions of the polymers were measured at 40 °C using Waters gel permeation chromatography (GPC) with a differential refractometer as the detector. THF and monodisperse polystyrene were used as the solvent and standard, respectively. Thermogravimetric analysis (TGA, Q5000, TA Instruments) was performed to determine the thermal properties from room temperature (RT) to 600 °C at a heating rate of 10 °C min^{-1} under N_2 purging. Differential scanning calorimetry (DSC) (TA Q1000) was conducted to determine the T_g in the temperature range of -50 to 200 °C at a heating rate of 10 °C·min^{-1} after initially heating for 5 min at 100 °C.

Surface Property Measurement

Silicon wafers were preliminarily cleaned with detergent (Deconex) and then ultrasonicated in water, acetone, and ethanol. Polymer films were prepared by spin coating 1 wt% α,α,α-trifluorotoluene solutions onto the cleaned silicon wafers at 3000 rpm for 60 s. To remove the residual solvent, the polymer films

were placed on a 100 °C hot plate for 2 h. The advancing and receding contact angles of water, DIM, and EG were measured at room temperature and ambient relative humidity using a DSA 100 contact angle analyzer with drop shape analysis software (Krüss). Dynamic contact angle measurements were performed by dispensing or aspiring liquid onto or from the polymer surface at the slowest possible rate using a motorized syringe device to eliminate the dynamic effect on the contact angle; the constant contact angles in the equilibrium region were reported. For each sample, the contact angles were measured more than six times on three different films, and the values were averaged. Surface roughness was determined using the non-contact mode atomic force microscopy (AFM, Park Systems) with a silicon nitride cantilever. Analysis was conducted with a scanning rate of 1 Hz for 5 μm × 5 μm and data were processed using XEI software. X-ray photoelectron spectroscopy (XPS) was performed using an UHV surface analysis system (AXIS NOVA, KRATOS). The photoelectron spectra were acquired in the constant analyzer energy (CAE) mode with a pass energy of 40 eV and step of 0.1 eV at a takeoff angle of 90°.

Determination of Protein Adsorption or Platelet Adhesion

All protein adsorption studies were performed on a Q-Sense E4 instrument (BiolinScientific, Sweden) using gold-coated AT-cut quartz sensors with a

fundamental frequency of 4.95 MHz (QSX 301, BiolinScientific). Prior to use, the sensors were exposed to ultraviolet radiation for 10 min, and then heated for 10 min in a base piranha solution (hydrogen peroxide:ammonia:deionized water = 1:1:5) at 75 °C for 5 min. Finally, the sensors were washed with DI water, acetone, and ethanol and dried under a flow of nitrogen. The sensors were spin coated with graft copolymers, followed by drying at 100 °C for 2 h. After mounting the sensors on the instrument, PBS was passed over the sensors to equilibrate the signal. Subsequently, protein solutions were passed over the surface at 0.1 mL min^{-1} to recode the frequency and dissipation signals. The protein solutions of 5 mg mL^{-1} albumin and 0.3 mg mL^{-1} fibrinogen were prepared based on the concentration ratios in human blood [39] and they were used to determine the absorption behavior at 37 °C. For each sample, the experiment was repeated at least three times and averaged. After the experiment, all the systems were cleaned by rinsing with a sodium dodecyl sulfate solution followed by PBS and DI water. In the case of viscoelastic or soft films such as the protein layer, viscoelastic modeling based on ΔF and ΔD is required to calculate the layer thickness or adsorbed mass. In our study, overtones n = 5, 7, and 11 were selected and their raw data was fitted by the Voigt viscoelastic model using Qtools software (Q-sense) to obtain the corrected values. The density of all the adsorbed layers was set as 1250 kg m^{-3} (between the densities of water (1000 kg m^{-3}) and protein

(1400 $kg \cdot m^{-3}$)). The density and viscosity of the liquid phase were set as 1000 kg m^{-3} and 0.0071 Pa s, respectively, and the model was optimized toward a lower χ^2 value by inputing the layer viscosity, layer shear modulus, and layer thickness. PRP(platelet rich plasma) was prepared from centrifugation of whole human blood (obtained from Innovative Research, Inc., Michigan) at 1200 rpm for 10 min. P(VDF-CTFE)-g-HFBMA and PMMA coated surfaces were prepared according to the method as shown in the section 4.5 and they were firstly soaked with 2 mL of PBS or BSA solution (5 mL mg^{-1}) for 60min. Then PRP absorption on the sample surfaces was accomplished by performing the following steps in sequence: first, incubation in 2 mL platelet-rich plasma (PRP) for 60 min at 37 °C, second, three times rinsing with PBS, third, immersion into 1 % solution of glutaraldehyde for 120 min at 37 °C, fourth, washing with PBS, PBS/DI water mixture (1:1, v/v), and DI water twice. After dried in air, the samples were observed by optical microscope (eclipse lv100nd, Nikon) and then TESCAN MIRA 3 SEM with 10kV after being sputter-coated with platinum. The numbers of adhered platelets were counted by SEM images obtained from the six different points of several samples and they were averaged.

2.3. Results and discussion

P(VDF-CTFE) was prepared by emulsion polymerization using a gas mixture of VDF and CTFE under the reaction conditions described in the Experimental Section. By comparing the integrals of the characteristic peaks of VDF and CTFE in the ^{19}F NMR spectrum, the molar ratio of VDF and CTFE in the resulting P(VDF-CTFE) was estimated as VDF:CTFE = 73:27 (mol%). The chlorine in P(VDF-CTFE) serves as an active site for graft-ATRP, and three kinds of FMMA monomers with different numbers (n) of fluorocarbon (i.e., trifluoromethyl methacrylate (TFEMA, n=1), pentafluoropropyl methacrylate (PFPMA, n=2), and heptafluorobutyl methacrylate, (HFBMA, n=3)) were used as branches of the graft copolymers for lowering the surface energy. The monomers with these short fluorocarbon chains ($n \leq 3$) were strategically selected so that the resulting polymers do not have limitations in terms of solubility in common solvents, compatibility with other polymers, and environmental friendliness. It has been reported that long fluorocarbon chains (i.e., $n \geq 6$) drastically reduce the solubility in common solvents and pose the potential environmental risk of bioaccumulation in wildlife despite their very low surface energies.[40-42]

Figure 2.1 show the structures of the graft copolymers, P(VDF-CTFE)-g-PFMMAs, which were prepared by ATRP method.[43, 44] Figure 2.2a shows the

^{1}H NMR spectra of P(VDF-CTFE) and the graft copolymers. For P(VDF-CTFE), the peak signals *a* at 2.3–2.5 ppm and 2.7–3.5 ppm correspond to the VDF unit. On the other hand, new peaks *b*, *c*, and *d* were observed at 0.8–1.5, 1.6–2.2, and 4.4–4.8 ppm for all the P(VDF-CTFE)-g-PFMMA samples, which were assigned to the methyl (–CH_3), methylene (–CH_2–), and methylene groups near the ester (–OCH_2–) of PFMMA, respectively. Furthermore, weak and broad peaks were observed around 6.5 ppm, which is attributed to the internal double bond on the backbone. Under the ATRP reaction conditions, internal unsaturation can occur by the β-hydrogen elimination mechanism, as previously reported.[45, 46] By comparing the peak integrals in the ^{1}H NMR spectra, the chemical compositions of P(VDF-CTFE)-g-PFMMAs were obtained, and are listed in Table 2.1; these were further confirmed from the ^{19}F NMR spectra (Figure 2.2b). The mole fraction of reacted CTFE and the average numbers of attached monomers in a side chain ranged from 9.3 to 11.1 mol% and 10.6 to 13.8 mol%, respectively, although the mole fraction of the generated double bond was in the range of 4.0–7.0 mol%. This led to higher PFMMA/VDF mole ratios, which are more than one. In addition, the fractions of the grafted PFMMAs were over 73%, as determined by converting the mole content to weight percent. On the other hand, the initial decomposition temperature decreased to 199.5, 230.4, and 226.0 °C for P(VDF-CTFE)-g-TFEMA, P(VDF-CTFE)-g-PFPMA, and P(VDF-CTFE)-g-HFBMA,

respectively, compared with that of P(VDF-CTFE) (405.5 °C) based on a mass loss of 1 wt% (Figure 2.3). This is because the PFMMA segments in the graft copolymers degraded first at these temperatures. The large difference in the degradation temperatures of the grafted parts (PFMMA) and polymer backbone (P(VDF-CTFE)) enabled the calculation of the PFMMA weight fraction, as shown in the TGA data. Therefore, the weight fractions of all the samples shown in Table 2.1 are comparable with those calculated from the ^{1}H NMR spectra.

Table 2.2 shows the advancing contact angles (θ_{adv}) and receding contact angles (θ_{rec}) of water, diiodomethane (DIM), and ethylene glycol (EG) on the surfaces of P(VDF-CTFE)-g-PFMMA films. The effect of surface roughness on the contact angle and hysteresis (θ_{hys}; θ_{adv} - θ_{rec}) could be ignored because all the sample surfaces were reasonably smooth ($R_{rms} \leq 2$). The θ_{adv} values of water, DIM, and EG were in the ranges of 101.4°–114.8°, 79.2°–94.4°, and 81.8°–95.7°, respectively, in the order of P(VDF-CTFE)-g-TFEMA < P(VDF-CTFE)-g-PFPMA < P(VDF-CTFE)-g-HFBMA, which coincides with the number of fluorocarbon on each monomer. Even though the θ_{adv} of water on the P(VDF-CTFE) film surface (103.2°) was slightly larger than that on the P(VDF-CTFE)-g-TFEMA (101.4°) surface, its θ_{hys} (≈ 54°) was considerably higher than that of the other samples; all the P(VDF-CTFE)-g-PFMMA samples showed similar θ_{hys} values in the ranges of 19°–21°, 13°–14°, and 9°–11° for water, DIM, and EG,

respectively. The θ_{hys} values for DIM and EG on P(VDF-CTFE) could not be obtained because of stick-slip behavior[47-49] and the instability of the film surface, respectively.

The surface energies of P(VDF-CTFE)-g-PFMMAs were calculated using the Owens–Wendt–Rabel–Kaelble (OWRK) equation using the θ_{adv} values of water, DIM, and EG (Table 2.2). P(VDF-CTFE)-g-PFMMAs have very low surface energies in the range of 11.1–19.0 mN m^{-1} because they contain considerable amounts of grafted methacrylates with fluorocarbon. Particularly, taking into account the surface energies of Teflon (18–20 mN m^{-1}) and PFMMAs with long fluorocarbon chains (8–10 mN m^{-1}), the surface energy value of P(VDF-CTFE)-g-HFBMA is sufficiently low.[50, 51] Even though the surface energies of pure PFMMA polymers were similar to those of P(VDF-CTFE)-g-PFMMAs,[52] film fabrication was not possible due to their brittle nature. The bendable free-standing films of the graft copolymers were shown on Figure 2.4 demonstrating the effect of P(VDF-CTFE) backbone. Therefore, the combination of P(VDF-CTFE) and grafted PFMMA are believed to be suitable for practical applications.

XPS analysis was conducted to investigate the surface compositions of P(VDF-CTFE)-g-PFMMAs. To compare the fluorocarbon surface composition of the P(VDF-CTFE) backbone and the grafted PFMMAs, the $–CF_3/–CF_2–$ carbon ratios were calculated by the relative areas of their C_{1s} peaks because only the PFMMA

segment contains the CF_3 moiety, while all the other parts contain the $–CF_2–$ moiety. The C_{1s} spectra of all the P(VDF-CTFE)-g-PFMMA surfaces between 280 eV and 296 eV were resolved into 8 peaks by the deconvolution fitting method (Figure 2.5a). The C_{1s} peaks corresponding to $–CF_3$ and $–CF_2–$ moieties appeared at 293.4 eV and 291.0 eV, respectively, and the other six peaks corresponded to the VDF, CTFE, and FMMA segments.[53] Figure 2.5b shows that a longer fluorocarbon chain of FMMA leads to a lower $–CF_3/–CF_2–$ ratio (both experimental and theoretical ratios) due to the increased number of $–CF_2–$ moiety on the grafted molecular structures. However, the differences between the experimental and theoretical ratios depended on the fluorocarbon number of FMMA. The experimental ratios of P(VDF-CTFE)-g-PFPMA and P(VDF-CTFE)-g-HFBMA were higher than their theoretical ratios, while for P(VDF-CTFE)-g-TFEMA, an opposite trend was observed. This indicates that unlike PTFEMA, PPFPMA and PHFBMA grafted on P(VDF-CTFE) tend to preferentially orient toward the top surface owing to the their lower surface energies than that of P(VDF-CTFE) (Table 2.2).[52] The XPS results are consistent with previous reports in that the polymer surfaces are mainly occupied by the fluorinated side groups with low surface energies,[54, 55] and are in good agreement with the contact angle and surface energy data discussed above.

The protein adsorption properties of P(VDF-CTFE)-g-PFMMAs were compared with those of the control polymers, P(VDF-CTFE) and PMMA. However, we failed to obtain the reliable results from P(VDF-CTFE) surfaces because it became easily unstable during the measurement. This might be due to its molecular flexibility at the experimental temperature (37 ºC) as reflected in its low glass transition temperature. Among the many proteins present in human blood, albumin and fibrinogen were chosen as the model proteins since they play an important role in the adsorption process in the circulatory system.[11, 56] Albumin is the most abundant protein in blood plasma and tends to adhere preferentially on foreign surfaces owing to its higher mobility. However, other proteins with a higher surface affinity can replace the albumin adsorbed on a surface by the "Vroman effect." [57, 58] It is known that the surface affinity of fibrinogen is much stronger than that of albumin, and it is the key glycoprotein that causes blood coagulation by binding the platelets. On the other hand, albumin is not directly involved in the coagulation cascade.[24]

The adsorption properties of the two model proteins on our fluorinated polymer surfaces were examined by quartz crystal microbalance with dissipation (QCM-D) monitoring. QCM-D measurements provide both frequency changes (ΔF) and dissipation changes (ΔD) for the adsorption of proteins on a surface as a function

of time, which are related to the additional mass and viscoelastic property of the surface, respectively.[25, 59, 60]

Figure 2.6a, b shows the ΔF and ΔD profiles for protein adsorption on P(VDF-CTFE)-g-HFBMA. The QCM signals were first equilibrated with a phosphate-buffered saline (PBS), and then the protein solution was injected. ΔF and ΔD sharply decreased and increased immediately after the injection of protein for a few minutes. Then, ΔF and ΔD stabilized with minor fluctuations. This indicates that protein adsorption occurred intensively in the first few minutes; however, the weakly bound albumin molecules were subsequently removed from surface upon rinsing with PBS. During the rinsing process, ΔF increased only slightly, which indicates that protein is stably attached onto the surface, while a small amount move reversibly between the surface and the albumin solution. In contrast, ΔD significantly decreased to near the reference level upon rinsing with PBS, indicating a more rigid coupling between the sensor surface and the additional layer under a low-viscosity PBS environment.[15, 51]

The thicknesses of the protein layers were calculated from the ΔF and ΔD profiles using the Voigt viscoelastic mode. Adhered protein masses and thicknesses are described in Table 2.3. The adsorbed albumin layer on all the P(VDF-CTFE)-g-PFMMAs were thinner than on the PMMA (> 5 nm), which was beyond the experimental error range; this is also reflected in the mass of adsorbed

albumin, i.e., the mass of adsorbed albumin decreased depending on the grafted polymers. Despite the small differences in the albumin layer thicknesses of the grafted copolymers, P(VDF-CTFE)-g-HFBMA evidently has the thinnest albumin layer. Considering the size of albumin (14 nm × 4 nm × 4 nm), it is expected that most of the albumins are arranged with their long axis parallel to the polymer surface to form the monolayers. Particularly, the albumin molecules on P(VDF-CTFE)-g-HFBMA were expected to form a more closely fitted structure on the surface. Probably, albumin plays a decisive role in lowering the interface energy between the water-based albumin solution and the graft copolymers by preferentially attaching on the surface. As the surface energy of the graft copolymers decreased, this tendency intensified, leading to an increase in contact area between albumin and the polymer surface.

Compared with albumin adsorption, fibrinogen adsorption exhibited significantly increased ΔD and ΔF, indicating the formation of a much thicker fibrinogen layer (16–25 nm) for all the samples. Considering that the short and long axes of fibrinogen are approximately 4 and 47 nm, respectively, the resulting layer thicknesses indicate that most of the fibrinogen were attached in a standing position with a tilted orientation [60, 61] although the degree of its orientation might depend on the polymer type. The higher thickness indicates a higher density of fibrinogen, which is attributed to a large amount of fibrinogen with its long axis

oriented perpendicular to the surface. Therefore, the low-surface energy fluorinated polymers, i.e., P(VDF-CTFE)-g-HFBMA and PVDF-g-PFPMA having thinner fibrinogen layers are effective in inhibiting fibrinogen adsorption compared with PMMA, regarding the amounts of adsorbed fibrinogen as shown in Table 2.3. Unexpectedly, P(VDF-CTFE)-g-TFEMA adsorbed the highest amount of fibrinogen, which is higher than that adsorbed by PMMA. This result is in agreement with previous reports in that the amount of adsorbed proteins reaches a pinnacle at moderately hydrophobic surfaces [56, 62] because the surface energy of P(VDF-CTFE)-g-TFEMA (18.7 mN m^{-1}) is higher and much lower than those of other fluorinated polymers (12.8 and 11.1 mN m^{-1}) and PMMA (44.3 mN m^{-1}),[63] respectively. In common clinical situations, blood-contacting instruments were firstly protected with buffer solutions to avoid the direct contact between blood and bare surface of devices. For example, during cardiopulmonary bypass, the major volume is pre-filled with buffer solution including albumin to stabilize the intravascular osmotic pressure.[64, 65] During the pretreatment process, an albumin layer is naturally formed on the surfaces of the circuit and oxygenator, which can act as a protective layer against fibrinogen adsorption. Therefore, we strategically applied this method to our materials, based on the results on single protein experiments. Figure 2.6c shows the representative ΔF and ΔD profiles of the P(VDF-CTFE)-g-HFBMA surfaces, which was obtained by a process

including albumin pretreatment, PBS rinsing, and subsequent fibrinogen adsorption. The adsorption thicknesses of fibrinogen were calculated from the ΔF and ΔD profiles of all the samples, as also displayed in Table 2.3. The amounts of adsorbed fibrinogen for all the samples remarkably decreased after albumin pretreatment. This was attributed to the beneficial effect of the albumin buffer solution, which led to mitigation of platelet loss and inhibition of inflammatory response, as reported after a practical surgical experiment.[66, 67] More surprising was the extremely low amount of fibrinogen adsorption of 5.6 ng cm^{-2} on the P(VDF-CTFE)-g-HFBMA surface, as compared with a high fibrinogen adsorption of 2069 ng cm^{-2} without albumin treatment. Hydrophobic graft copolymers prevented fibrinogen adsorption more effectively with albumin treatment than PMMA did; the amounts of fibrinogen adsorbed on P(VDF-CTFE)-g-TFEMA and P(VDF-CTFE)-g-PFPMA surfaces were 2.4 and 3.3 times less than that adsorbed by the PMMA surface, respectively.

Figure 2.7 provides an insight into the overwhelming effect of P(VDF-CTFE)-g-HFBMA on the basis of arrayed structures of adsorbed albumins. The larger contact area between P(VDF-CTFE)-g-HFBMA and albumin might have led to a higher content of albumin lying on the surface with its long axis parallel to the polymer surface, giving rise to an ordered array, as hypothesized based on the albumin layer thickness. Such a conformation of albumin can generate a rigid

coupling between albumin and the surface, resulting in the inhibition of blood coagulation by preventing the replacement of albumin by fibrinogen.

The platelet adhesion test was further conducted to prove the blood compatible character of P(VDF-CTFE)-g-HFBMA with albumin layer, which can suppress the adhesion of platelet as well as fibrinogen. The samples were incubated with PRP for 60 min at 37 °C in vitro, and observed by scanning Electron microscope (SEM). Even though the highest number of platelets was observed on P(VDF-CTFE)-g-HFBMA surface (Figure 2.8a) due to its hydrophobic nature,[32] the albumin treatment changed it into the new surface with the lowest platelet adhesion (Figure 2.8b). Some spreaded platelets were also observed for P(VDF-CTFE)-g-HFBMA and PMMA without albumin treatment (Figures 2.8a and c), indicating the platelet activation.[21] Even though the albumin passivation was also highly effective for PMMA surface (Figure 2.8d), P(VDF-CTFE)-g-HFBMA surface had the lower number of attached platelets than PMMA surface according to the quantitative analysis as shown in Figure 2.8e. Therefore, we believe that the combination of the graft copolymer with a low surface energy and albumin treatment is an ideal strategy that can be applied to various blood-contacting devices without blood damage.

2.4. Conclusion

P(VDF-CTFE) (VDF:CTFE = 73:27 mol%) was modified by grafting PFMMAs with fluorinated side chains (-$(CF_2)_{n-1}CF_3$, n = 1, 2, 3) by ATRP to lower the surface energy. NMR analysis revealed that the mole fractions of the reacted CTFE and the average number of PFMMAs in a side chain were in the range of 9.3–11.1 mol% and 10.6–13.8 mol%, respectively. Therefore, the weight fractions of the grafted PFMMAs were more than 73%, which indicated that they are the major constituents of the polymers. Nevertheless, the bendable free-standing films could be easily fabricated from all the grafted polymers because of the effect of P(VDF-CTFE) backbone. The surface energies of the graft copolymers were in the range of 11.1–18.7 mN m^{-1} depending on the number of fluorocarbons in PFMMA (n), and they correlated well with the surface compositions. The graft copolymer with the lowest surface energy, P(VDF-CTFE)-g-HFBMA (n=3), was more effective in inhibiting albumin and fibrinogen adsorptions compared with the other graft copolymers and PMMA. However, surprisingly, P(VDF-CTFE)-g-HFBMA remarkably reduce the amount of fibrinogen adsorption from 2069 ng cm^{-2} to 5.6 ng cm^{-2} after albumin pretreatment. Although the other copolymers demonstrated this phenomenon, the amount of adsorbed fibrinogen was considerably higher than 5.6 ng cm^{-2}. This

outstanding effect of P(VDF-CTFE)-g-HFBMA could be explained by the rigid coupling between albumin and the polymer surface, which resulted in the albumin layer blocking fibrinogen adsorption. Considering that fibrinogen is the key glycoprotein that causes blood coagulation, our grafted copolymer system with an albumin layer is very promising for application in various extracorporeal blood-contacting devices, which require a higher performance and safety.

2.5. References

[1] S. S. Hayek, S. Sever, Y.-A. Ko, H. Trachtman, M. Awad, S. Wadhwani, M. M. Altintas, C. Wei, A. L. Hotton, A. L. French, L. S. Sperling, S. Lerakis, A. A. Quyyumi, J. Reiser, *N. Engl. J. Med.,* 2015, *373*, 1916-1925.

[2] D. Abrams, D. Brodie, *Chest,* 2017, *152*, 639-649.

[3] M. Schmidt, H. Wunsch, D. Brodie, *Intensive Care Med.,* 2018, *44*, 2219-2221.

[4] J. Seo, J.-H. Seo, *ACS Appl. Mater. Interfaces,* 2017, *9*, 19591-19600.

[5] I. Banerjee, R. C. Pangule, R. S. Kane, *Adv. Mater.,* 2011, *23*, 690-718.

[6] D. Kiaei, A. S. Hoffman, T. A. Horbett, *J Biomater Sci Polym Ed.,* 1992, *4*, 35-44.

[7] L.-C. Xu, C. A. Siedlecki, *J. Biomed. Mater. Res*., 2010, *92A*, 126-136.

[8] S. Ravi, E. L. Chaikof, *Regen Med,* 2010, *5*, 107-120.

[9] E. Ostuni, R. G. Chapman, R. E. Holmlin, S. Takayama, G. M. Whitesides, *Langmuir,* 2001, *17*, 5605-5620.

[10] L.-C. Xu, C. A. Siedlecki, *Biomaterials,* 2007, *28*, 3273-3283.

[11] I. H. Jaffer, J. C. Fredenburgh, J. Hirsh, J. I. Weitz, *J. Thromb. Haemost.,* 2015, *13*, S72-S81.

[12] Q. Chen, G. Thouas, *Biomaterials: A Basic Introduction*, Taylor & Francis, Florida, USA, 2018.

[13] J. L. Harding, M. M. Reynolds, *Trends Biotechnol.,* 2014, *32*, 140-146.

[14] P. Roach, D. Farrar, C. C. Perry, *J. Am. Chem. Soc.,* 2005, *127*, 8168-8173.

[15] S. Chen, L. Li, C. Zhao, J. Zheng, *Polymer,* 2010, *51*, 5283-5293.

[16] D.-G. Kim, H. Kang. S. Han, J.-C. Lee, *ACS Appl. Mater. Interfaces,* 2012, *4*, 5898-5906.

[17] D. Shen, B. Xu, X. Huang, Q. Zhuang, S. Lin, *Polym. Chem.,* 2018, *9*, 2821-2829.

[18] L. Li, B. Yan, L. Zhang, Y. Tian, H. Zeng, *Chem. Commun.,* 2015, *51*, 15780-15783.

[19] Y. Chang, Y.-J. Shih, C.-Y. Ko, J.-F. Jhong, Y.-L. Liu, T.-C. Wei, *Langmuir,* 2011, *27*, 5445-5455.

[20] Y. Xia, V. Adibnia, R. Huang, F. Murschel, J. Faivre, G. Xie, M. Olszewski, G. De Crescenzo, W. Qi, Z. He, R. Su, K. Matyjaszewski, X. Banquy, *Angew. Chem. Int. Ed.* 2019, *58*, 1308-1314.

[21] Y. Chang, Y.-J. Shih, C.-J. Lai, H.-H. Kung, S. Jiang, *Adv. Funct. Mater.,* 2013, *23*, 1100-1110.

[22] H. J. Kwon, Y. Lee, L. T. Phuong, G. M. Seon, E. Kim, J. C. Park, H. Yoon, K. D. Park, *Acta Biomater,.* 2017, *61*, 169-179.

[23] P. Bengani-Lutz, E. Converse, P. Cebe, A. Asatekin, *ACS Appl. Mater. Interfaces,* 2017, 9, 20859−20872.

[24] X. Liu, L. Yuan, D. Li, Z. Tang, Y. Wang, G. Chen, H. Chen, J. L. Brash, *J.*

Mater. Chem. B, 2014, *2*, 5718-5738.

[25] Q. Wei, T. Becherer, S. Angioletti-Uberti, J. Dzubiella, C. Wischke, A. T. Neffe, A. Lendlein, M. Ballauff, R. Haag, *Angew. Chem. Int. Ed.,* 2014, *53*, 8004-8031.

[26] E. Ostuni, B. A. Grzybowski, M. Mrksich, C. S. Roberts, G. M. Whitesides, *Langmuir,* 2003, *19*, 1861-1872.

[27] A. Sethuraman, M. Han, R. S. Kane, G. Belfort, *Langmuir,* 2004, *20*, 7779-7788.

[28] M. Yaseen, X. Zhao, A. Freund, A. M. Seifalian, J. R. Lu, *Biomaterials,* 2010, *31*, 3781-3792.

[29] M. V. Pergal, V. V. Antic, G. Tovilovic, J. Nestorov, D. Vasiljevic-Radovic, J. Djonlagic, *J. Biomat. Polym. Sci. Polym. Ed.,* 2012, *23*, 1629-1657.

[30] I. S. Bayer, M. K. Tiwari, C. M. Megaridis, *Appl. Phys. Lett.,* 2008, *93*, 173902.

[31] D. E. Newton, *Chemistry of New Materials*. Facts On File, Incorporated: 2009.

[32] S. Nie, H. Qin, C. Cheng, W. Zhao, S. Sun, B. Su, C. Zhao, Z. Gu, *J. Mater. Chem. B,* 2014, *2*, 4911-4921.

[33] F. Ai, H. Li, Q. Wang, W. Z. Yuan, X. Chen, L. Yang, J. Zhao, Y. Zhang, *J. Mater. Sci.,* 2012, *47*, 5030-5040.

[34] U. Klinge, B. Klosterhalfen, A. P. Öttinger, K. Junge, V. Schumpelick, *Biomaterials,* 2002, *23*, 3487-3493.

[35] T. He, J. Wang, P. Huang, B. Zeng, H. Li, Q. Cao, S. Zhang, Z. Luo, D. Y. B. Deng, H. Zhang, W. Zhou, *Colloids Surf. B,* 2015, *130*, 278-286.

[36] Y. Sui, Z. Wang, X. Gao, C. Gao, *J. Membr. Sci,.* 2012, *413–414*, 38-47.

[37] A. Venault, J.-R Wu, Y. Chang, P. Aimar, *J. Membr. Sci.,* 2014, *470*, 18-29.

[38] S. Ozcan, P. Kaner, D. Thomas, P. Cebe, A. Asatekin, *ACS Appl. Mater. Interfaces,* 2018, 10, 18300-18309.

[39] R. K. Roy, H. W. Choi, J. W. Yi, M. W. Moon, K. R. Lee, D. K. Han, J. H. Shin, A. Kamijo, T. Hasebe, *Acta Biomater.,* 2009, 5, 249-256

[40] J. Liu, S. M. Avendaño, A Review. *Environ. Int.,* 2013, *61*, 98-114.

[41] C. A. Ng, K. Hungerbühler, *Environ. Sci. Technol.,* 2014, *48*, 4637-4648.

[42] L. Xiao, Y. Ling, A. Alsbaiee, C. Li, D. E. Helbling, W. R. Dichtel, *J. Am. Chem. Soc.,* 2017, *139*, 7689-7692.

[43] M. Zhang, T. P. Russell, *Macromolecules,* 2006, *39*, 3531-3539.

[44] F. Guan, L. Yang, J. Wang, B. Guan, K. Han, Q. Wang, L. Zhu, *Adv. Funct. Mater.,* 2011, *21*, 3176-3188.

[45] S. Tan, J. Li, G. Gao, H. Li, Z. Zhang, *J. Mater. Chem.,* 2012, *22*, 18496.

[46] X. Hu, S. Tan, G. Gao, Y. Xie, Q. Wang, N. Li, Z. Zhang, *J. Polym. Sci., Part A: Polym. Chem.,* 2014, *52*, 3429-3440.

[47] E.-H. Sohn, J. Ahn, B. G. Kim, J.-C. Lee, *Langmuir,* 2011, *27*, 1811-1820;

[48] E.-H. Sohn, B. G. Kim, J.-S. Chung, J.-C. Lee, *J. Colloid Interface Sci,.* 2010, *343*, 115-124.

[49] E.-H. Sohn, S. H. Kim, M. Lee, J.-C. Lee, K. Song, *J. Colloid Interface Sci.,* 2011, *360*, 623-632.

[50] Y. Tamada, Y. Ikada, *J. Colloid Interface Sci.,* 1993, *155*, 334-339.

[51] W. Yao, Y. Li, X. Huang, *Polymer,* 2014, *55*, 6197-6211.

[52] E.-H. Sohn, J.-W. Ha, S.-B. Lee, I. J. Park, Chains. *Langmuir,* 2016, *32*, 9748-9756.

[53] G. Beamson, D. Briggs, *High Resolution XPS of Organic Polymers: The Scienta ESCA300 Database*, Wiley, Chichester, UK 1992.

[54] A. F. Thünemann, A. Lieske, B.-R. Paulke, *Adv. Mater.,* 1999, *11*, 321-324.

[55] S. Y. Heriot, R. A. L. Jones, *Nat. Mater.* 2005, *4*, 782-786.

[56] C. P. Stallard, K. A. McDonnell, O. D. Onayemi, J. P. O'Gara, D. P. Dowling, *Biointerphases* 2012, *7*, 31.

[57] E. F. Leonard, L. Vroman, *J. Biomater. Sci. Polym. Ed.,* 1992, *3*, 95-107.

[58] S.-Y. Jung, S.-M. Lim, F. Albertorio, G. Kim, M. C. Gurau, R. D. Yang, M. A. Holden, P. S. Cremer, *J. Am. Chem. Soc.,* 2003, *125*, 12782-12786.

[59] I. Reviakine, D. Johannsmann, R. P. Richter, *Anal. Chem.,* 2011, *83*, 8838-8848.

[60] A. Doliška, V. Ribitsch, K. S. Kleinschek, S. Strnad, *Carbohydr. Polym.,* 2013, *93*, 246-255.

[61] A. C. H. Pape, B. D. Ippel, P. Y. W. Dankers, *Langmuir,* 2017, *33*, 4076-4082.

[62] S. H. Baxamusa, K. K. Gleason, *Adv. Funct. Mater.,* 2009, *19*, 3489-3496.

[63] E.-H. Sohn, J. Kim, B. G. Kim, J. I Kang, J.-S. Chung, J. Ahn, J. Yoon, J.-C. Lee, *Colloids Surf. B,* 2010, *77*, 191-199.

[64] L. Chen, L. Lv, C. Long, S. Lou, *Perfusion,* 2016, *31*, 576-583.

Table 2.1. Compositions of P(VDF-CTFE)-g-PFMMA graft copolymers

	Chemical composition (VDF:$CTFE_{rea}$[a]:$CTFE_{un}$[b]:DB[c])	VDF/ PFMMA[d]	DP_{PFMMA}	$Wt\%_{PFMMA}$[e]	$Wt\%_{PFMMA}$[f]
P(VDF-CTFE) -g-TFEMA	71.0:11.1:11.9:6.0	1 / 2.4	13.8	78.1	80.9
P(VDF-CTFE) -g-PFPMA	71.0:9.5:12.5:7.0	1 / 1.4	10.6	73.6	74.2
P(VDF-CTFE) -g-HFBMA	72.0:9.3:14.7:4.0	1 / 1.5	13.3	79.4	82.4

[a] Reacted CTFE

[b] Unreacted CTFE

[c] Double bond

[d] Mole ratio

[e] Calculated from ^1H NMR spectra

[f] Calculated from TGA.

.

Table 2.2. Contact angles of P(VDF-CTFE) and P(VDF-CTFE)-g-PFMMA

Sample	Contact angle degree (STD) [a]						Surface energy (mN m^{-1}) [f]
	Water		Diiodomethane		Ethylene glycol		
	θ_{adv} [b]	θ_{rec} [c]	θ_{adv} [b]	θ_{rec} [c]	θ_{adv} [b]	θ_{rec} [c]	
P(VDF-CTFE)	103.2(0.9)	49.0(0.6)	75.7(1.3)[d]	[d]	[e]	[e]	20.1
P(VDF-CTFE) -g-TFEMA	101.4(1.4)	81.5(1.1)	79.2(0.8)	66.4(1.3)	81.8(0.7)	70.9(0.7)	18.7
P(VDF-CTFE) -g-PFPMA	110.7(1.1)	91.4(1.9)	90.7(1.2	76.6(0.3)	91.7(1.0)	77.7(1.5)	12.8
P(VDF-CTFE)-g-HFBMA	114.8(0.5)	93.9(1.1)	94.4(0.9)	80.3(1.2)	95.7(0.9)	86.3(0.5)	11.1

[a] The standard deviations are indicated in parentheses

[b] Advancing contact angle

[c] Receding contact angle

[d] Stick-slip behavior

[e] The polymer films were damaged

[f] Owens–Wendt–Rabel–Kaelble method

Table 2.3. Adsorbed protein masses on the surfaces of P(VDF-CTFE)-g-PFMMAs and PMMA

	Amount of adsorbed protein (ng cm^{-2})		Adhered fibrinogen after albumin coating (ng cm^{-2})	Thickness of protein layer (nm)		Fibrinogen thickness after albumin coating (nm)
	BSA	Fibrinogen		BSA	Fibrinogen	
P(VDF-CTFE)-g-TFEMA	604 ± 28	3021 ± 70	26.7 ± 5.9	4.5 ± 0.1	24.2 ± 0.6	0.21 ± 0.05
P(VDF-CTFE)-g-PFPMA	576 ± 7	2013 ± 32	19.2 ± 2.6	4.5 ± 0.1	16.1 ± 0.3	0.15 ± 0.02
P(VDF-CTFE)-g-HFBMA	523 ± 15	2069 ± 119	5.6 ± 2.7	4.3 ± 0.1	16.6 ±1.0	0.05 ± 0.02
PMMA	656 ± 13	2542 ± 77	62.8 ± 8.0	5.1 ± 0.2	20.3 ± 0.6	0.50 ± 0.06

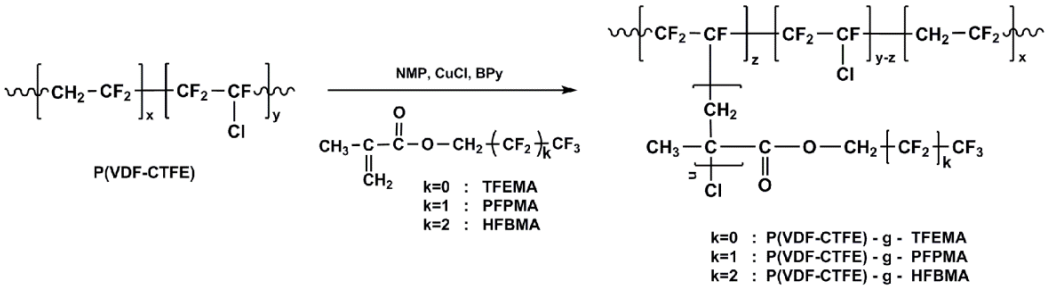

Figure 2.1. Synthetic route of P(VDF-CTFE)-based graft copolymers via ATRP

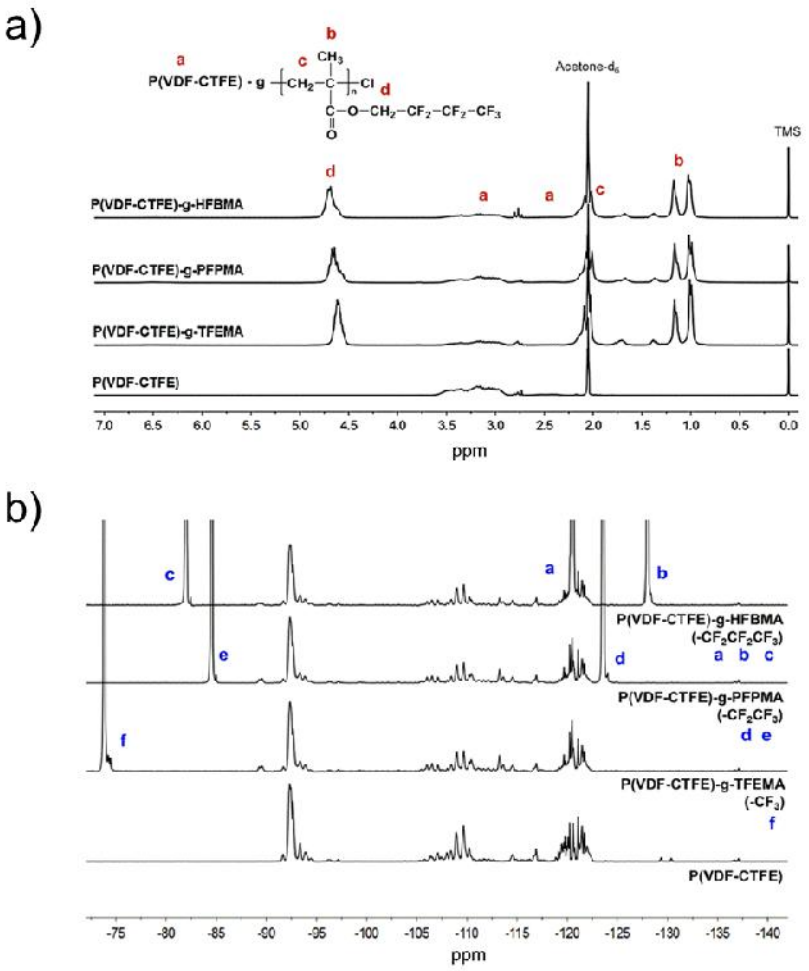

Figure 2.2. (a) ^{1}H NMR and (b) ^{19}F NMR spectra of P(VDF-CTFE)-g-PFMMA graft copolymers.

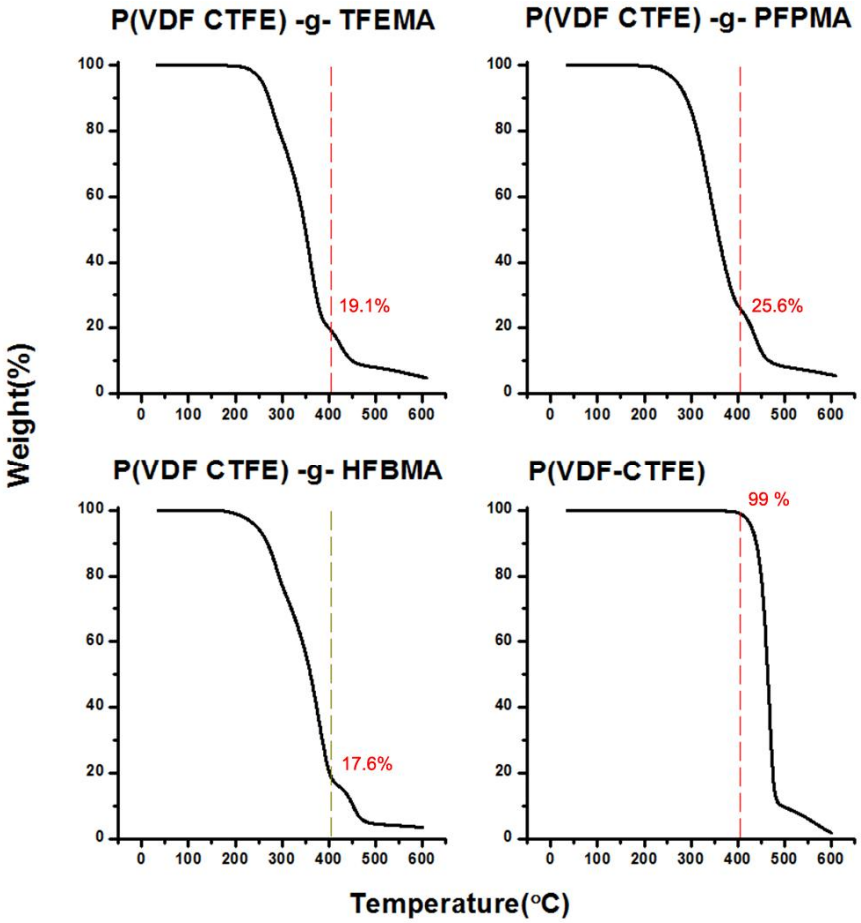

Figure 2.3. TGA curves of P(VDF-CTFE) and P(VDF-CTFE)-g-PFMMAs, and weight proportions of residues at 405.5 ºC

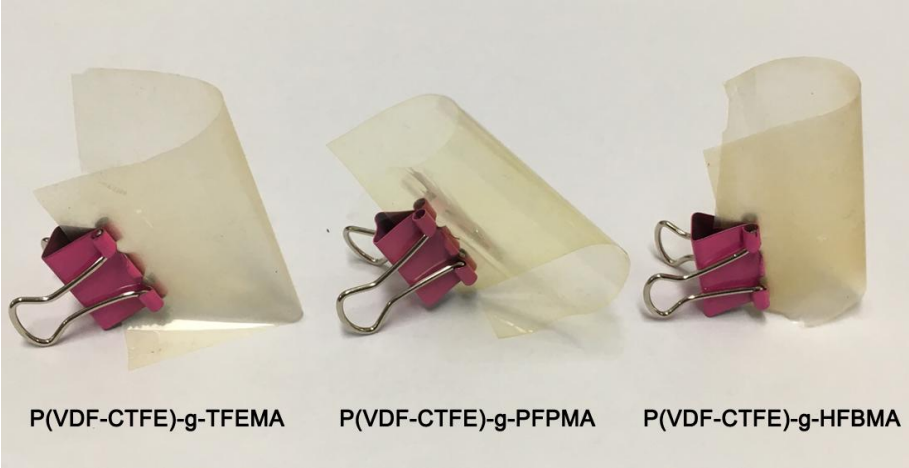

Figure 2.4. Flexible, free-standing films of P(VDF-CTFE)-PFMMA graft copolymers

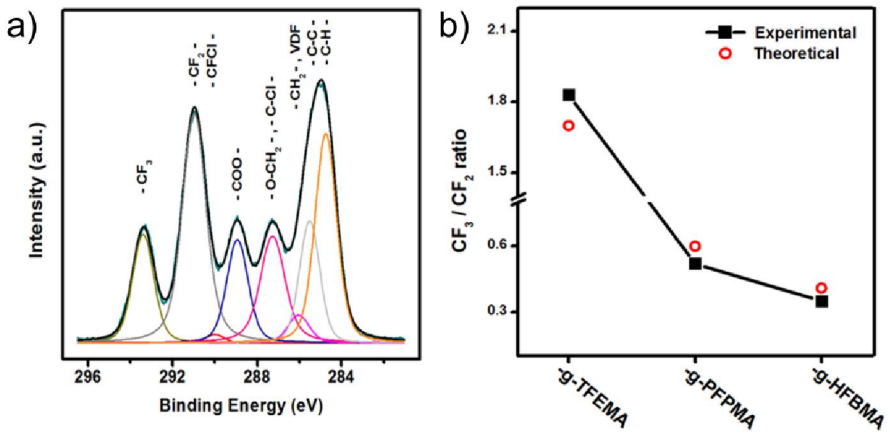

Figure 2.5. (a) XPS C_{1s} narrow spectra of P(VDF-CTFE)-g-HFBMA surface, and (b) CF_3/CF_2 ratio of P(VDF-CTFE)-g-PFMMA

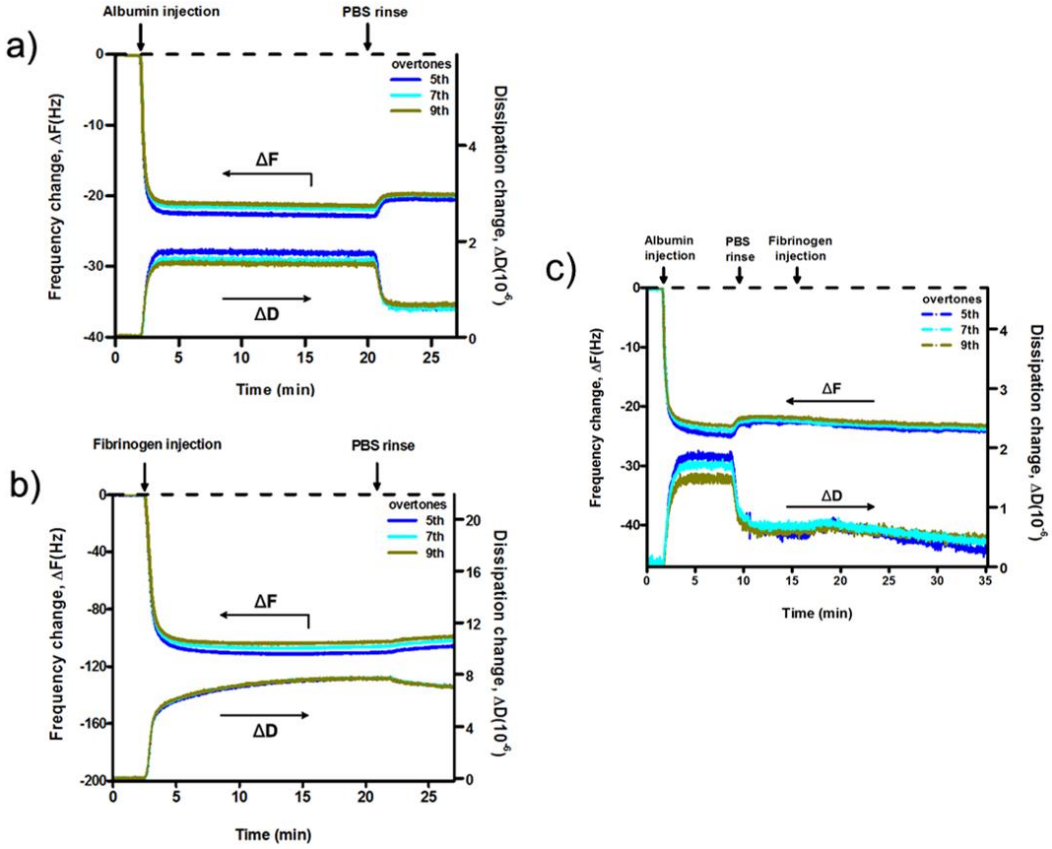

Figure 2.6. Representative traces of frequency and dissipation changes for P(VDF-CTFE)-g-HFBMA of (a) albumin, (b) fibrinogen, and (c) fibrinogen after albumin pretreatment

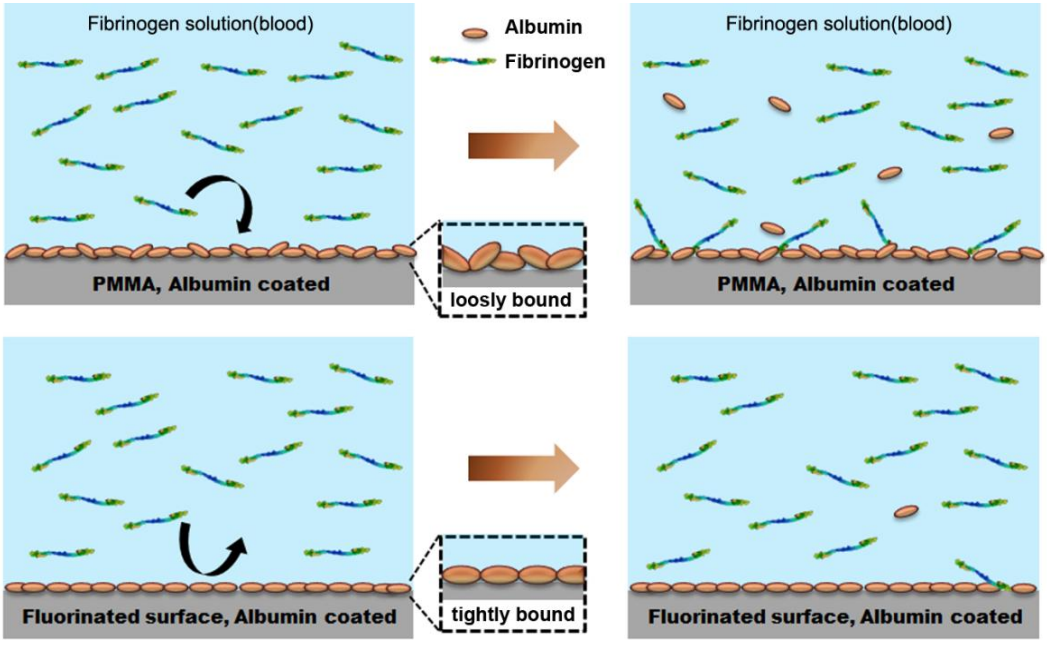

Figure 2.7. Schematic illustration explaining the different behaviors of albumin-fibrinogen replacement on PMMA and P(VDF-CTFE)-g-HFBMA surfaces

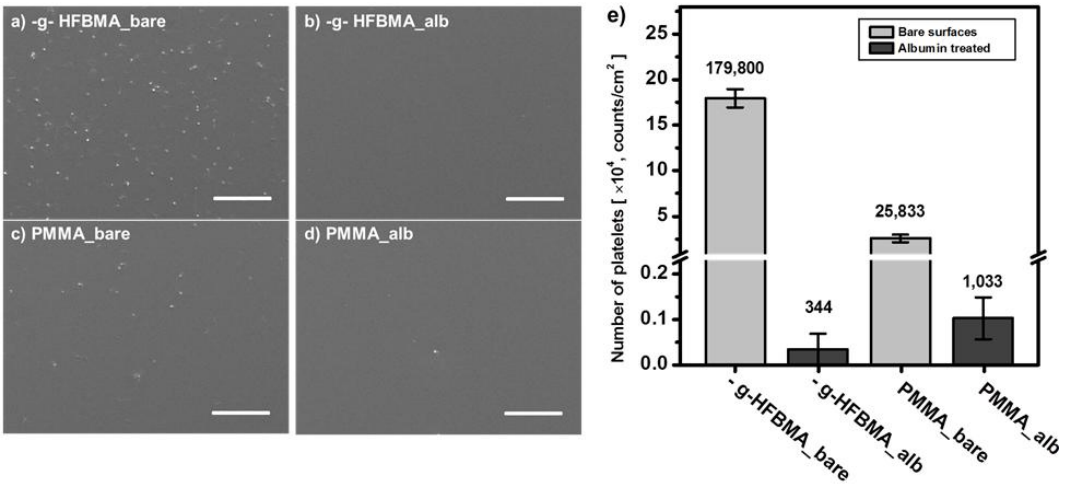

Figure 2.8. SEM images of platelets adhered on the surfaces of (a) bare P(VDF-CTFE)-g-HFBMA, (b) albumin-treated P(VDF-CTFE)-g-HFBMA, (c) bare PMMA, (d) albumin-treated PMMA (Scale bar = 50μm), and (e) the number of platelets on the surfaces

Chapter 3

Poly(vinylidene fluoride)-Based Film with Strong Antimicrobial Activity

3.1. Introduction

Poly(vinylidene fluoride) (PVDF) and its copolymers have gained tremendous attention owing to their distinctive properties based on their unique molecular structure.[1,2] Consequently, they have been widely applied in various areas, such as in rechargeable batteries,[3,4] dielectric devices,[5,6] water treatment systems,[7–9] and particularly for biomedical devices.[10–12] Due to their excellent biocompatibility, they were allowed for use in food, biochemical, and pharmaceutical industries by the Federal Drug Administration.[13] However, in order to utilize fluoropolymers in the medical and healthcare fields, they will inevitably require antimicrobial functions because it has been reported that PVDF surfaces could be easily bio-contaminated with microbial colonization and biofilm formation.[14,15]

To impart antimicrobial properties onto PVDF-based polymers, numerous studies have been conducted as categorized into three types of processes: i) embedment (or blend) of antimicrobial substances,[8,9,13,16,17] ii) surface modification,[18–20] and iii) covalent immobilization.[21–23] Regarding the embedding method, easy preparation process is its greatest advantage. However, embedded antimicrobial substances can be leaked out from the polymers that cause environmental and drug-resistance problems [9,17,23] and the lifetime to

shorten.[19,24] It has been reported that the surface modification method also suffers from the wash-out of antimicrobial surface modifier [18] as well as from a challenging large-scale application.[20] Covalent immobilization methods have been estimated to have strong advantages, including stable attachment of antimicrobial moieties and enhanced antibacterial properties with long-term durability.[22,23,25] However, this method still has drawbacks originated form the complex synthetic processes.

To achieve microbial resistance, various kinds of antimicrobial substances were introduced into PVDF. Among them, cationic groups including ammonium,[17] pyridinium,[14] guanidinium,[23] and imidazolium [22] have been widely studied owing to their excellent antimicrobial activities. They are known to exert antimicrobial activity through electrostatic interactions [17] and contact-killing mechanism, [24] which can act for a long time when they are immobilized on the surface. Especially, ammonium and pyridinium moieties were frequently utilized due to their accessibility from commercial sources and relatively facile reaction pathway.[7,20]

In this work, cationic monomers bearing quaternary ammonium or quaternary pyridinium groups were covalently grafted onto poly(vinylidene fluoride-co-chlorotrifluoroethylene) (P(VDF-CTFE)) by the one-step chlorine-initiated atom transfer radical polymerization (ATRP) method. The antimicrobial activities of the

resulting polymers were estimated using three strains of *Escherichia coli*, *Staphylococcus aureus*, and *Candida albicans,* which are listed as the most common pathogenic bacteria or yeast causing infections in the United States Centers for Disease Control and Prevention (CDC).[26,27] Further, the cationic grafted polymers were strategically blended with PVDF because their structural similarity can induce a strong attraction between their polymer chains. In addition, the antimicrobial performances of the blends were optimized by including a small amount of the cationic grafted polymers (i.e., 1 wt%, 5 wt%) for efficient utilization from an economical perspective

3.2. Experimental

Materials

P(VDF-CTFE) (M_n =149,000, PDI = 1.8) with 15 wt% CTFE was purchased from Polyk Technologies (USA) and PVDF (Kynar 761) was provided by Arkema (France). Iodomethane (99%), CuCl (99.99%), basic alumina, (dimethylamino)ethylmethacrylate (DMAEMA, 98%), phosphate buffer saline (PBS) tablets, and glutaraldehyde solution were obtained from Sigma-Aldrich (USA). 4-vinyl pyridine (4VP, 96%) was purchased from Alfa Aesar (USA) and N,N,N',N'',N''-pentamethyldiethylenetriamine (PMDTA, 99%) was provided from TCI Chemicals (Japan). Dimethyl sulfoxide (DMSO, HPLC grade) and dimethylformamide (DMF, HPLC grade) were purchased from Duksan Chemicals (South Korea), and all the NMR solvents were obtained from Euriso-top (France). The monomers were passed through a column of basic alumina before use, and all other reagents were used as received.

Synthesis of cationic grafted copolymers

Graft copolymers were synthesized by ATRP, in which the Cl atoms on P(VDF-CTFE) were used as the initiation sites. In a 100 mL Schlenk flask, 3.18 mM of DMAEMA (3.8 mM of 4VP) in 30 mL DMSO was first reacted with

iodomethane (1.1 equiv. to monomer) at 50 °C to form a quaternized monomer. After 24 h, the solution was stirred for 90 min at elevated temperature under vacuum to eliminate unreacted iodomethane. Then, 1.5 g of P(VDF-CTFE) dissolved in 30 mL DMSO was poured into the flask and degassed under vacuum. Following the degassing process, CuCl (2.0 mM) was introduced and the solution was further degassed by several vacuum-nitrogen cycles until 2.0 mM of PMDTA was added. The flask was then transferred to a preheated reactor (90 °C) and the reaction proceeded under a nitrogen atmosphere. After 24 h, the solution was cooled to 25 °C and precipitated in a 1:1 ethanol/hexane mixture (v/v). The precipitate was further purified by washing in ethanol and an excess amount of DI water several times. Approximately 2 g of the polymers was obtained and named PVDF-g-QDMA or PVDF-g-Q4VP depending on whether DMAEMA or 4VP was added during the synthesis.

Blend film fabrication

Polymer films were solvent-casted from blends of the synthesized graft copolymers and PVDF. The ratios of the graft copolymer to PVDF were fixed at 1:99 and 5:95 by mass and dissolved in a DMF/DMSO mixture (1:1 v/v) to obtain 18 wt% casting solutions. The prepared solutions were cast onto glass plates or PET films at 80 °C to make antibacterial PVDF films with thicknesses of ~15 μm

(for antibacterial characterization) or 70 μm (for analyzing mechanical properties). The fabricated films were denoted as Blend-QDMA-# or -Q4VP-#, where # is the content of each graft copolymer.

Characterization

The chemical structures of the graft copolymers were confirmed by 500 MHz ^{1}H NMR spectroscopy (AVANCE 500, Bruker, USA) using DMSO-d_6 as the solvent and TMS as an internal standard. In specific analysis, a small amount of trifluoroacetic acid was added to the DMSO solvent to shift the H_2O peak. Fourier transform infrared (FTIR) spectra were obtained using a spectrophotometer (FT/IR-4100, JASCO, USA). KBr pellets were used as a reference, and signals were obtained by co-addition of 32 scans at a resolution of 2 cm^{-1}. Differential scanning calorimetry (DSC, Q1000, TA Instruments, USA) was conducted to determine the thermal properties in the temperature range of -50 to 200 °C at a heating rate of 10 °C min^{-1}. Thermogravimetric analysis (TGA, Q5000, TA Instruments, USA) was carried out from room temperature (RT) to 600 °C at a heating rate of 10 °C·min^{-1} under N_2 purging. Spin-coated films were prepared from 2 wt% DMF solutions of graft polymers (3000 rpm for 150 s) on pre-cleaned silicon substrates (for 2D X-ray diffraction analysis) or glass slides (for antimicrobial analysis). Two-dimensional grazing incidence wide-angle X-ray

diffraction (2D GIWAXD) and transmission wide-angle X-ray diffraction analyses were performed using a high-power X-ray beam from a synchrotron source (3C beamline, Pohang Accelerator Laboratory, Korea).[28] The mechanical properties of the polymer films were tested using a universal testing machine (UTM, MultiTest 2.5-I, Mecmesin, UK) at a tensile speed of 10 mm min^{-1}. The samples were cut into dog-bone shapes, in which the part tested had a width of 10 mm. Scanning electron microscope (SEM) images were obtained by MAGNA FEG SEM (Tescan, Czech) with 5 kV after platinum-coated. X-ray photoelectron spectroscopy (XPS) analysis was conducted using a multipurpose surface analysis system (AXIS Nova/Supra, Kratos, UK). The water contact angles were measured at room temperature and ambient relative humidity using a DSA 100 goniometer with ADVANCE software (Krüss, Germany).

Antimicrobial properties

Antimicrobial properties were measured using film attachment tests. *Staphylcococcus aureus* (*S. aureus*, ATCC 6538), *Escherichi coli* (*E. coli*, ATCC 8739), and *Candida albicans* (*C. albicans*, ATCC 10231) were chosen for representative gram positive bacteria, gram negative bacteria, and pathogenic yeast, respectively. To prepare the strain suspensions, *S. aureus* and *E. coli* were grown in nutrient agar (NA) and *C. albicans* was grown in potato dextrose agar

(PDA) at 32 °C for 24 h. After cultivation, bacteria or yeast suspensions were prepared by appropriate dilution. To evaluate the antimicrobial characteristics, 0.4 mL of each suspension was dropped on a 5 cm × 5 cm film (spin coated on glass slides or casted on PET film) and the surface was covered with a sterilized film of the same size for the contact between the microbial suspension and the surface at 32 °C. After 24 h, the cover film was peeled off and 10 mL of nutritional broth was added into the Petri dish to elute the bacteria on the substrates. Subsequently, the strain solutions were serially diluted and spread on the culture medium. After 24 h at 32 °C, the remaining colonies were counted to analyze antimicrobial activity. Results were obtained from more than three different measurements and averaged. Antimicrobial rate (AR, %) was calculated as $AR= (1 - CFU_{experimental}/CFU_{control}) \times 100\ \%$, where $CFU_{control}$ and $CFU_{experiment}$ are the numbers of viable microbe on positive control and sample film, respectively.[23,29] The morphologies of microbes on the films were examined through SEM analysis. After incubation of the strains, fixation (2.5 % glutaraldehyde, 120 min) and dehydration (series of EtOH solution of 25%, 50%, 70%, 90%, 95%, and 100%) processes were conducted on the sample films. After dried in air, the samples were coated by platinum and then they were observed by SEM (TESCAN MIRA 3, 10 kV). The inhibition zone test was conducted as following procedure. NA (for *S. aureus* and *E. coli*) or PDA (for *C. albicans*)

plates were inoculated with 0.1 mL of strain suspensions with a concentration of 10^6 CFU/mL. Then, circular films with a diameter of 1.5 cm were placed on the plates. Samples were cultured at 32 °C for 24 h (for *S. aureus* and *E. coli*) or 25 °C for 48 h (for *C. albicans*) in an incubator.

To assess the environmental stability of the antimicrobial ability, Blend-QDMA-5 and Blend-Q4VP-5 films are placed in the temperature - humidity chamber (LH-TP50). Temperature and relative humidity were set as 85 °C and 85%, respectively. After 72h, blend films are dried in air and subjected to film attachment antimicrobial tests.

Cell viability

Cell viability was characterized using a LIVE/DEAD Cell Imaging Kit (ThermoFisher Scientific, USA). Live cells were stained with non-fluorescent cell-permeant calcein acetoxymethyl (AM) (ex/em: 488 nm/515 nm), which is enzymatically converted to intense green fluorescent calcein within live cells. The cell-impermeable BOBO-3 iodide (ex/em: 570 nm/602 nm) can enter through the damaged cell membranes and bind to DNA, indicating dead cells by generating red fluorescence. The labeled cells were observed using an automated microscope (Lionheart LX, BioTek, USA) with a 4X objective lens. The live-cell area was quantified to measure cell confluency by analyzing the green/red fluorescent

microscopic images using Fiji Image processing software (Image J, National Institute of Health, USA). In addition, luminescence-based adenosine triphosphate (ATP) was measured using the CellTiter-Glo luminescent cell viability assay (Promega, USA). Since ATP provides energy to various biological processes in living cells, it can show living and metabolically active cells.

3.3. Results and discussion

Two different cationic monomers with quaternary ammonium moiety (QDMA) or quaternary pyridinium moiety (Q4VP) were prepared by the reaction of iodomethane and DMAEMA or 4VP, respectively, according to a previously reported procedure.[30,31] The cationic monomers were graft-polymerized in the P(VDF-CTFE) backbone to form cation-functionalized polymer chains by the ATRP method (Figure 3.1a).[2] Molecular structures of the resulting polymers, PVDF-g-QDMA and PVDF-g-Q4VP, were identified by ^{1}H NMR and FTIR spectroscopy (Figures 3.1b and c). All samples revealed identical ^{1}H NMR peaks at 2.7–3.5 ppm and 2.3–2.5 ppm, which were attributed to the VDF unit (head-to-tail and tail-to-tail sequences, respectively). The methylene units between the ester and quaternized amine groups of PVDF-g-QDMA produced signals around 4.4 and 3.9 ppm, and a strong signal at 3.3 ppm was assigned to nine identical protons in quaternary ammonium ($–N^{+}(CH_3)_3$).[30] Conversely, the characteristic peaks of the Q4VP group were observed at 4.2 and 7.5–9.0 ppm, which were identified as the N-methyl proton and aromatic pyridine in PVDF-g-Q4VP, respectively.[32] This successful graft polymerization was finally verified by measuring the ability of the cation functional groups to be quantitatively quaternized, through the carful investigation of NMR (Figure 3.2a) and N_{1s} XPS spectra (Figure 3.2b).

Furthermore, the amount of grafted monomers could be calculated by comparing the peak integrals of the VDF part and the grafted parts of QDMA and Q4VP. Therefore, the grafted parts of PVDF-g-QDMA and PVDF-g-Q4VP were determined to be 36 wt% and 33 wt%, respectively; the weight fractions were also comparable with the results obtained by the thermogravimetric method shown in Figure 3.3. Additionally, FTIR analysis provided evidence of the grafted molecular structures, as shown in Figure 3.1c. In the PVDF-g-QDMA spectrum, the peak at 1732 cm^{-1} was attributed to the carbonyl group, and peaks around 884 and 1402 cm^{-1} were assigned to quaternary ammonium,[33] while the peaks at 1476, 1521, 1573, and 1643 cm^{-1} arose from the grafted methyl pyridinium group in PVDF-g-Q4VP.[32,34]

As displayed in the DSC thermograms of the P(VDF-CTFE) and graft copolymers (Figure 3.4a), the heats of fusion (ΔH_f) of the graft copolymers were noticeably lower than that of P(VDF-CTFE), indicating reduced crystallinity, although that of P(VDF-CTFE) was known to be significantly lower than that of the PVDF homopolymer, owing to the bulky chlorine atom, which acts as a defect.[1,6] More specifically, their crystalline structures on the thin film surface were analyzed by GIWAXD experiments, yielding 2D diffractograms. The line profiles of q-values were extracted from the in-plane direction of the 2D images (Figure 3.4b) and P(VDF-CTFE) displayed diffraction related to the α-form

crystal structure of PVDF, which could be indexed as $(100)_\alpha$, $(110)_\alpha$, and $(120)_\alpha$.[5,6] However, the grafted copolymer samples exhibited lower intensities of the $(100)_\alpha$ and $(110)_\alpha$ peaks, and no peaks in the $(120)_\alpha$ region. Instead, the $(200)_\beta$ peak related to the β-form crystal structure was prominent in both PVDF-g-QDMA and PVDF-g-Q4VP profiles. This is attributed to the reduction of α-PVDF and enhanced polarity by grafted charged moieties (Figure 3.4c).[5,35] The FTIR spectra support these results; peaks from α-phase PVDF (i.e., 615, 764, 796, and 976 cm^{-1}) in P(VDF-CTFE) were hardly observed after grafting QDMA and Q4VP (Figure 3.1c).

The antimicrobial performances of PVDF-g-QDMA and PVDF-g-Q4VP were investigated by the film attachment method, which counts the colony forming units after cultivation of microorganisms.[36,37] This experiment was conducted using three different types of pathogenic microorganisms, namely, gram-positive bacteria, *S. aureus* (Figure 3.5a), gram negative-bacteria, *E. coli* (Figure 3.5b), and opportunistic fungi, *C. albicans* (Figure 3.5c). When the antimicrobial activity of P(VDF-CTFE) was initially measured, it unexpectedly exhibited considerable bactericidal property against gram negative *E. coli* (c.a. 80%) compared with the control sample (without any treatment, 100% live bacteria), although there was no effect against *C. albicans.* Interestingly, ideal antimicrobial activities were produced by introducing QDMA and Q4VP moieties into P(VDF-CTFE) despite

the relatively small contents of their grafted cationic parts (~35 wt%); both PVDF-g-QDMA and PVDF-g-Q4VP exhibited inhibition rates greater than 99.99% against all the microorganisms. It is believed that these polymers, with complete antimicrobial properties, could be extensively applied in various fields based on the verified performance of PVDF-based polymers.[10,14]

PVDF has been widely utilized in water treatment membranes,[9,38] piezoelectric polymer scaffolds,[16] energy harvesting devices,[5,39] and medical devices [10,11] due to its outstanding properties.[1,40] In most of these applications, there is a growing need for incorporating antimicrobial functions because of serious threats of bio-contaminants such as viruses, bacteria, and fungi.[41,42] Therefore, the PVDF-based cationic polymers were incorporated into PVDF as additives using a solution blending method and the preparation process is schematically displayed on Figure 3.6a. Strategically, the antimicrobial activity of the PVDF blend films was optimized by only a small amount of our cationic polymers (i.e., 1 wt%, 5 wt%) to prevent the growth of phase-separated domains, giving rise to a sustained film uniformity. Figure 3.6b shows the highly flexible free-standing films of PVDF blends containing a small amount of cationic polymers. As the cationic polymer content increased, the PVDF blend films became more yellowish from the intrinsic color of the cationic polymers.[43] In order to estimate the practicality of the PVDF blend films, their film properties

were preferentially analyzed in terms of their crystalline structure, mechanical properties, surface composition, and wettability.

Figure 3.6c shows the WAXD diffraction profiles of pristine PVDF and the blend films. The X-ray diffraction profiles of all the blend films were almost identical to those of the pristine PVDF film, indicating no influence of our grafted cationic polymers on the crystalline structure of PVDF,[44] although there were significant differences in their crystalline structures, as shown in Figure 3.4b. This result was also supported by DSC measurements, which showed no clear changes in T_m values (Figure 3.7). The ΔH_f values of the blend films were slightly decreased depending on the proportion of PVDF-g-QDMA and PVDF-g-Q4VP contents; nevertheless, the values (44.7–46.6 J/g) remained comparable with that of the pristine PVDF film (48.1 J/g). This suggests that the polymer chains of PVDF-g-QDMA and PVDF-g-Q4VP were well dispersed in the PVDF matrix below the nanometer scale when their contents were within 5 wt%. SEM images in Figure 3.8 also showed that there was no macro (or micro)-phase separation for any of the blend films.

Figure 3.6d shows the typical stress–strain curves of pristine PVDF and blend films with 1 wt% and 5 wt% of the grafted cationic polymers, and their values for tensile stress and elongation at break are summarized in Figure 3.6e. Interestingly, 1 wt% of the grafted cationic copolymers, despite it being a small addition, could

enhance the tensile stress of pristine PVDF (25 MPa) in the range of 3–5 MPa; further, the 5 wt% addition led to the much higher values of 33 MPa (Blend-QDMA-5) and 30 MPa (Blend-Q4VP-5). This result can be explained by intensified internal interactions caused by the high polarity of the cationic moieties in PVDF-g-QDMA and PVDF-g-Q4VP.[22,35] For the elongation at break, adding 1 wt% of the grafted cationic polymers was somewhat better than the 5 wt% addition for both blend samples. This is probably because of the brittle nature of the ionic parts.[22,45] Nonetheless, all the blend films demonstrated similar or better elongation properties than those of pristine PVDF, leading to the conclusion that the grafted cationic polymers are also valuable in enhancing mechanical properties.

XPS analysis was employed to investigate the surface compositions of the polymer blend films; the C_{1s} core-level spectra for PVDF, Blend-Q4VP-5, and Blend-QDMA-5 are shown in Figure 3.9a. The C_{1s} spectra of the blend films were observed in the ranges of 293–283 eV, which could be separated into five peaks by a deconvolution method [2,22] and assigned to CF_2, C=O, C–O/C–N, CH_2, and C–H/C–C species at 290.3 eV, 287.6 eV, 286.4 eV, 285.8 eV, and 284.8 eV, respectively. The CF_2 and CH_2 peaks originated from the integrated PVDF, while C–C/C–H peaks were observed only for the blend films with cationic moieties. C=O and C–O/C–N peaks were observed for all samples, although pristine PVDF

should not contain these species. However, this observation coincided with a previous result that some commercially available PVDFs (including Kynar 761 used in this study) revealed the presence of C=O and C–O/N/S groups.[38] In order to compare the quantitative compositions of the cationic parts, the area ratios of the deconvoluted spectra were further calculated for each sample (Table 3.1). C–C/C–H peaks only corresponded to the grafted cationic parts [22] and their area ratios demonstrated a clear dependence on the feed content of PVDF-g-QDMA and PVDF-g-Q4VP. Moreover, increased proportion of C–O/C–N peak areas also corroborate the result as shown in Figure 3.9b. This indicates the exposure of cationic additives to the surfaces, which can affect the film surface wettability (Figure 3.9c). Therefore, the water contact angle of PVDF decreased from 91° to ~82° by including only 1 wt% of cationic polymers, and it was further reduced by the 5 wt% addition. The water contact angle of Blend-Q4VP-5 was lower than that of Blend-QDMA-5; this result is strongly related to the amount of the cationic parts on their surfaces, as shown in the XPS analysis. Importantly, the cationic parts on the surface also affected the antimicrobial activity of the blend films, as discussed below.

The antimicrobial activities of the blend films were investigated based on the survival rate of bacteria or yeast on the film surfaces, and they were compared with those of the control and pristine PVDF. As shown in Figure 3.10a, all the

blend films exhibited excellent bactericidal performance against gram-positive bacteria, *S. aureus* (> 99.99%), even when the films contained only 1 wt% of the cationic polymers. However, this antibacterial activity was weakened for gram-negative bacteria, *E. coli* (Figure 3.10b), because neither cationic polymer was sufficient to deactivate *E. coli* with 1% additive content, although the proportions of live bacteria were only about 20–30%. When the blend film contained 5% of the cationic polymers, they demonstrated more than 99% bactericidal activity, similar to the antimicrobial activity of pure cationic polymers; in particular, the Blend-QDMA-5 film exhibited over 99.99% bactericidal activity. This definite difference in bactericidal ability against *S. aureus* and *E. coli* could be derived from the structural difference of the cytomembrane or cell wall;[23,29,31] gram-negative bacteria have a protective membrane outside the cell wall, which can reduce damage from contact killing surfaces compared to gram-positive bacteria.[7,46] Furthermore, the antifungal ability was also estimated against the pathogenic yeast, *C. albicans*, possessing layered wall structure and more components (glucans, chintin, and manoproteins) compared with bacteria.[42,47,48] Figure 3.10c shows that PVDF-g-Q4VP with a pyridinium group was comparatively effective in achieving sufficient antimicrobial activity of > 99% for both 1 wt% and 5 wt%. In contrast, PVDF-g-QDMA with a quaternary ammonium group only displayed an antimicrobial activity of 83% even when the

blend included 5 wt% of the cationic polymer. Overall, Blend-QDMA-5 is the best selection, providing the ideal antimicrobial property against both *S. aureus* and *E. coli*, whereas Blend-Q4VP-5 is quite useful against a wide range of species, including both bacteria and fungi.

The strong antimicrobial actions of the blend films were verified by observing the morphologies of the strains, as shown in SEM images of Figure 3.10d and Figure 3.11. Microbes cultivated on pristine PVDF show relatively intact profiles which were enveloped by outer wall. However, the spherical shape of *S. aureus* was completely destroyed on Blend-Q4VP-5 film surface.[49] In case of *E. coli* and *C. albicans*, the cell surface was severely deformed or burst, implying that the cell wall has been destroyed.[29,48] although their shapes still remained. Thereby, the major mechanism of the antibacterial ability was supposed to electrostatic interaction between cationic moieties and negatively charged microbes[47,50] that cause the disruption of cell wall by contact-killing.[17,24] Moreover, Figure 3.10e displayed that there were no inhibition zones on Blend-Q4VP-5 film against all microbes, implying the non-leaching characteristic of the antimicrobial materials. Based on the results, the proposed contact killing mechanism[23,24,50] was diagrammatically displayed on Figure 3.10f.

To assess the environmental stability, the antimicrobial activities of Blend-QDMA-5 and Blend-Q4VP-5 films were further measured after exposing to harsh

environment conditions at T=85ºC and RH=85% for 72h. Figure 3.12 showed that both blend samples still showed almost perfect antibacterial activity against *S. aureus* and *E. coli* (AR> 99.9%), indicating no influence on the biocidal effect against the bacterial species. On the other hand, the ARs against *C. albicans* decreased to 20.4 % and 90.5 % for Blend-QDMA-5 and Blend-Q4VP-5 films, respectively. Although this result may indicate the transformation in molecular conformation, Blend-Q4VP-5 sample still showed more than 90% of activity, attributable to stable aromatic structure of Q4VP.[51] From these results, PVDF blend films with non-leaching, thermostable, and good antimicrobial activities will be applicable in broad environments for long-term use.

Figure 3.13 shows the bright-field (BF) and immunofluorescence images of the Human Cardiac Microvascular Endothelial (HCME) cells cultured without and with the prepared films for 2 days in a 6-well plate. Regardless of the existence and type of the films, cellular architectures such as the cytoskeleton and nucleus were well-formed and maintained during cultivation. No apparent differences were observed between the cells cultured without and with the films. Viability of the HCME cells was also characterized by Live/Dead cell imaging and ATP measurement, as depicted in Figure 3.14. According to the Live/Dead fluorescence images, the HCME cells adhered to and proliferated on the surface of the culture plate, despite being cultured with the films (Figure 3.14a). The

Live/Dead cell ratio was also calculated from the fluorescent images, which indicated that a very high cell viability was maintained during the 2 day cultivation, revealing approximately a 99% live cell ratio from all experimental groups (Figure 3.14b). Moreover, no significant reduction was observed in the ATP content of the cells cultured with films in comparison to the control, which cultured the HCME cells only (Figure 3.14c). These results demonstrate that the films did not have a critical effect on cell viability, indicating their potential as biocompatible materials.

3.4. Conclusion

Cationic graft polymers were successfully prepared by graft-polymerization of QDMA and Q4VP monomers in P(VDF-CTFE) through a one-step chlorine-initiated ATRP method, resulting in attachments of 36 wt% and 33 wt%, respectively. These polymers, PVDF-g-QDMA and PVDF-g-Q4VP, demonstrated perfect antibacterial or antifungal abilities (antimicrobial rate > 99.99%) against common bacteria and pathogenic yeast (*E. coli*, *S. aureus*, *C. albicans*) on their coated surfaces. Furthermore, small amounts of the cationic graft polymers were also effective in providing their strong antimicrobial activities in pristine PVDF when they were added in amounts of only 1 wt% and 5 wt% in pristine PVDF by the solution blending method. In particular, Blend-Q4VP-5 exhibited an antimicrobial rate higher than 99% against *E. coli*, *S. aureus*, and *C. albicans*, while all blend films displayed excellent biocompatibility. Because these cationic graft polymers can enhance the mechanical strength of pristine PVDF with no influence on its crystalline structure and film flexibility, it is believed that they can be widely used in biomedical applications.

3.5. References

[1] B. Ameduri, *Chem. Rev.,* 2009, 109, 6632–6686.

[2] D.J. Han, H.J. Heo, I.J. Park, H.S. Kang, S.G. Lee, S.-B. Lee, J.-C. Lee, E.-H. Sohn, *ACS Appl. Polym. Mater.,* 2020, *2*, 178–188.

[3] X. Hao, H. Wenren, X. Wang, X. Xia, J. Tu,. *Colloid Interface Sci.,* 2019, *558*, 145–154.

[4] W.J. Song, S.H. Joo, D.H. Kim, C. Hwang, G.Y. Jung, S. Bae, Y. Son, J. Cho, H.K. Song, S.K. Kwak, S. Park, S.J. Kang, *Nano Energy,* 2017, *32*, 255–262.

[5] C. Wan, C.R. Bowen, *J. Mater. Chem. A,* 2017, *5*, 3091–3128.

[6] Y. Huang, J.Z. Xu, T. Soulestin, F.D. Dos Santos, R. Li, M. Fukuto, J. Lei, G.J. Zhong, Z.M. Li, Y. Li, L. Zhu, *Macromolecules,* 2018, *51*, 5460–5472.

[7] M. Mukherjee, S. De, *Environ. Sci. Water Res. Technol.,* 2018, *4* (8), 1078–1104.

[8] T. Li, F. Liu, H. Lin, Z. Xiong, H. Wang, Y. Zhong, L. Xiang, A. Wu, *J. Colloid Interface Sci.,* 2018, *517*, 93–103.

[9] Z. Wang, Y. Tang, T. Wang, K. Liang, *J. Hazard. Mater.,* 2019, *368*, 421–428.

[10] A. Park,Y. Song, E. Yi, B. T. D. Nguyen, D. Han, E. H. Sohn, Y. I. Park, J. T. Jung, Y. M. Lee, Y. H. Cho, *ACS Biomater. Sci. Eng.*, 2020, *6*, 6424–6434.

[11] V.R. Sastri, *Plastics in Medical Devices: Properties, Requirements, and*

Applications; William Andrew, Norwich, 2013.

[12] M. Spasova, N. Manolova, N. Markova, I. Rashkov, *Appl. Surf. Sci.,* 2016, *363*, 363–371.

[13] A. Muñoz-Bonilla, A. Kubacka, M. Fernández-García, M. Ferrer, M. Fernández-García, M.L. Cerrada, *Eur. Polym. J.,* 2015, *71*, 412–422.

[14] C. Yao, X. Li, K.G. Neoh, Z. Shi, E.T. Kang, *Appl. Surf. Sci.,* 2009, *255*, 3854–3858.

[15] S.B. Kumar, P. Sharnagat, P. Manna, A. Bhattacharya, S. Haldar, *Environ. Sci. Pollut. Res.,* 2017, *24*, 5831–5840.

[16] Y. Yang, S. Peng, F. Qi, J. Zan, G. Liu, Z. Zhao, C. Shuai, *Mater. Sci. Eng. C,* 2020, *116*, 111195.

[17] X. Zhang, J. Ma, C.Y. Tang, Z. Wang, H.Y. Ng, Z. Wu, *Environ. Sci. Technol.,* 2016, *50*, 5086–5093.

[18] E. Koh, Y.T. Lee, *J. Ind. Eng. Chem.,* 2017, *47*, 260–271.

[19] M. Ping, X. Zhang, M. Liu, Z. Wu, Z. Wang, *J. Membr. Sci.,* 2019, *570–571*, 286–293.

[20] W. Sun, W. Liu, Z. Wu, H. Chen, *Macromol. Rapid Commun.,* 2020, *41*, 1900430.

[21] Y. Sui, Z. Wang, C. Gao, *Desalin. Water Treat.,* 2014, *52*, 6377–6388.

[22] J. Guan, Y. Wang, S. Wu, Y. Li, J. Li, *Biomacromolecules,* 2017, *18*, 4364–

4372.

[23] F. Chen, X. Ding, Y. Jiang, Y. Guan, D. Wei, A. Zheng, X. Xu, *ACS Omega,* 2020, *5*, 10481–10488.

[24] R. Kaur, S. Liu, *Prog. Surf. Sci.,* 2016, *91*, 136–153.

[25] C. Ergene, K. Yasuhara, E.F. Palermo, *Polym. Chem.,* 2018, *9*, 2407–2427.

[26] J.K. Oh, X. Lu, Y. Min, L. Cisneros-Zevallos, M. Akbulut, *ACS Appl. Mater. Interfaces,* 2015, *7*, 19274–19281.

[27] CDC, *Antibiotic Resistance Threats in the United States, 2019*; Atlanta, GA: U.S. Department of Health and Human Services, CDC, 2019.

[28] D.J. Han, S. Kim, H.J. Heo, I.J. Park, H.S. Kang, S.G. Lee, J.-C. Lee, E.-H. Sohn, *ACS Appl. Polym. Mater.,* 2020, *2*, 3957–3965.

[29] J. Du, Y. Li, J. Wang, C. Wang, D. Liu, G. Wang, S. Liu, *ACS Appl. Mater. Interfaces,* 2020, 12, 26966–26972.

[30] D. Roy, J.S. Knapp, J.T. Guthrie, S. Perrier, *Biomacromolecules,* 2008, *9*, 91–99.

[31] J. Lin, X. Chen, C. Chen, J. Hu, C. Zhou, X. Cai, W. Wang, C. Zheng, P. Zhang, J. Cheng, Z. Guo, H. Liu, *ACS Appl. Mater. Interfaces,* 2018, *10*, 6124–6136.

[32] Y. Xue, H. Xiao, *Polymers,* 2015, *7*, 2290–2303.

[33] A. Skandalis, S. Pispas, *Polym. Chem.,* 2017, *8,* 4538–4547.

[34] N. Sahiner, O. Ozay, *Colloids Surf. A Physicochem. Eng. Asp.,* 2011, *378*, 50–59.

[35] C. Xing, M. Zhao, L. Zhao, J. You, X. Cao, Y. Li, *Polym. Chem.,* 2013, *4*, 5726–5734.

[36] S. Ghamrawi, J.P. Bouchara, O. Tarasyuk, S. Rogalsky, L. Lyoshina, O. Bulko, J.F. Bardeau, *Mater. Sci. Eng. C.,* 2017, 75, 969–979.

[37] S. Ferraris, S. Perero, P. Costa, G. Gautier di Confiengo, A. Cochis, L. Rimondini, F. Renaux, E. Vernè, M. Ferraris, S. Spriano, *Appl. Surf. Sci.,* 2020, 508, 144707.

[38] P. Kaner, A. V. Dudchenko, M.S. Mauter, A. Asatekin, *J. Mater. Chem. A,* 2019, *7*, 4829–4846.

[39] T. Li, Z.Q. Feng, K. Yan, T. Yuan, W. Wei, X. Yuan, C. Wang, T. Wang, W. Dong, J. Zheng, *J. Mater. Chem. B,* 2018, *6*, 5343–5352.

[40] P. Pladis, A.H. Alexopoulos, C. Kiparissides, *Ind. Eng. Chem. Res.* 2014, *53*, 7352–7364.

[41] A.A. Dundas, O. Sanni, J.F. Dubern, G. Dimitrakis, A.L. Hook, D.J. Irvine, P. Williams, M.R. Alexander, *Adv. Mater.,* 2019, *31*, 1903513.

[42] C. Vallieres, A.L. Hook, Y. He, V.C. Crucitti, G. Figueredo, C.R. Davies, L. Burroughs, D.A. Winkler, D.A. Winkler, D.A. Winkler, D.A. Winkler, R.D. Wildman, D.J. Irvine, M.R. Alexander, S. V. Avery, *Sci. Adv.,* 2020, *6*, eaba6574.

[43] X. Hu, J. Li, H. Li, Z. Zhang, *J. Polym. Sci. A Polym. Chem.*, 2012, 50, 3126-3134.

[44] C. Xing, Y. Wang, C. Zhang, L. Li, Y. Li, J. Li, *Ind. Eng. Chem. Res.,* 2015, 54, 9351–9359.

[45] G. Godeau, L. Navailles, F. Nallet, X. Lin, T.J. McIntosh, M.W. Grinstaff, *Macromolecules,* 2012, *45*, 2509–2513.

[46] C. Schwechheimer, M.J. Kuehn, *Nat. Rev. Microbiol.,* 2015, *13* (10), 605–619.

[47] H.H. Lara, D.G. Romero-Urbina, C. Pierce, J.L. Lopez-Ribot, M.J. Arellano-Jiménez, M. Jose-Yacaman, *J. Nanobiotechnology*., 2015, 13, 1–12.

[48] F.X. Hu, K.G. Neoh, L. Cen, E.T. Kang, *Biotechnol. Bioeng.,* 2005, 89, 474–484.

[49] A. Kanazawa, T. Ikeda, T. Endo, *J. Polym. Sci. Part A Polym. Chem.,* 1993, 31, 1467–1472.

[50] Q. Song, R. Zhao, T. Liu, L. Gao, C. Su, Y. Ye, S.Y. Chan, X. Liu, K. Wang, P. Li, W. Huang, *Chem. Eng. J.*, 2021, 418, 1–10.

[51] S.H. Tang, A. Venault, C. Hsieh, G.V. Dizon, C.T. Lo, Y. Chang, *J. Membr. Sci,.* 2020, 598, 117655.

Table 3.1. Deconvoluted area ratios from C_{1s} XPS curve of PVDF and blend films

	CF_2 (PVDF)(%)	*CH_2 (PVDF)(%)*	*C=O(%)*	*C-O/C-N (%)*	*C-C/C-H (%)*
PVDF	47.25	46.40	1.28	5.08	-
Blend-QDMA-1	47.04	43.71	1.31	6.11	1.83
Blend-QDMA-5	46.45	42.14	1.44	7.51	2.46
Blend-Q4VP-1	47.99	42.63	1.05	6.16	2.17
Blend-Q4VP -5	46.75	38.74	1.08	10.07	3.35

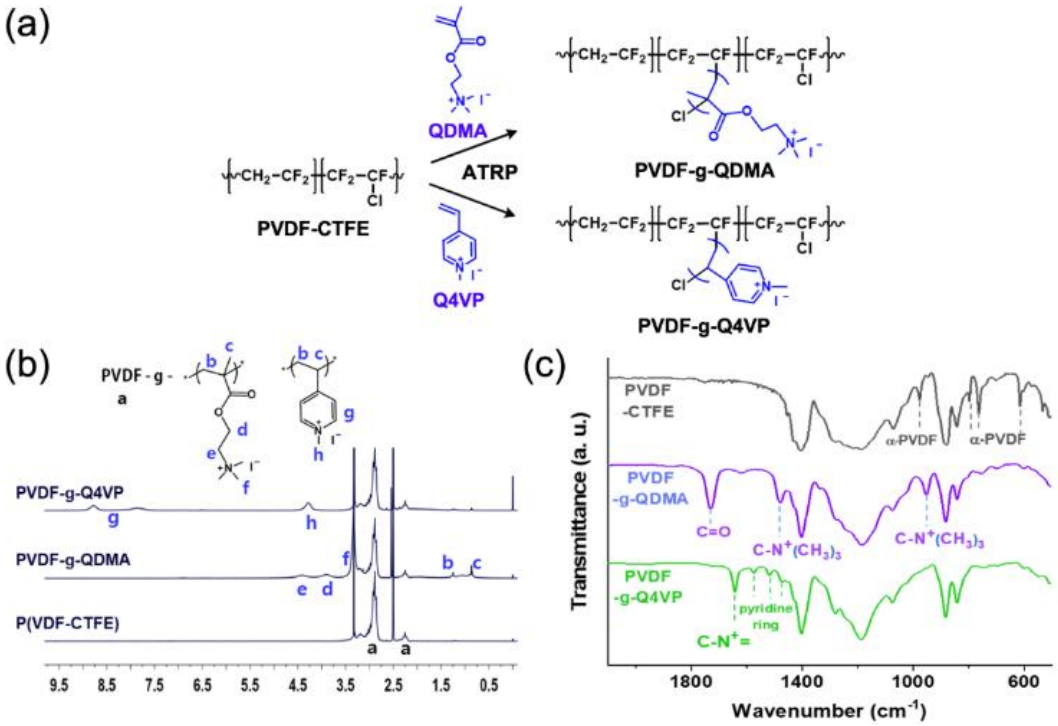

Figure 3.1. (a) Synthetic route, (b) ^{1}H NMR, and (c) FT-IR spectra of PVDF-g-QDMA, PVDF-g-Q4VP, and P(VDF-CTFE)

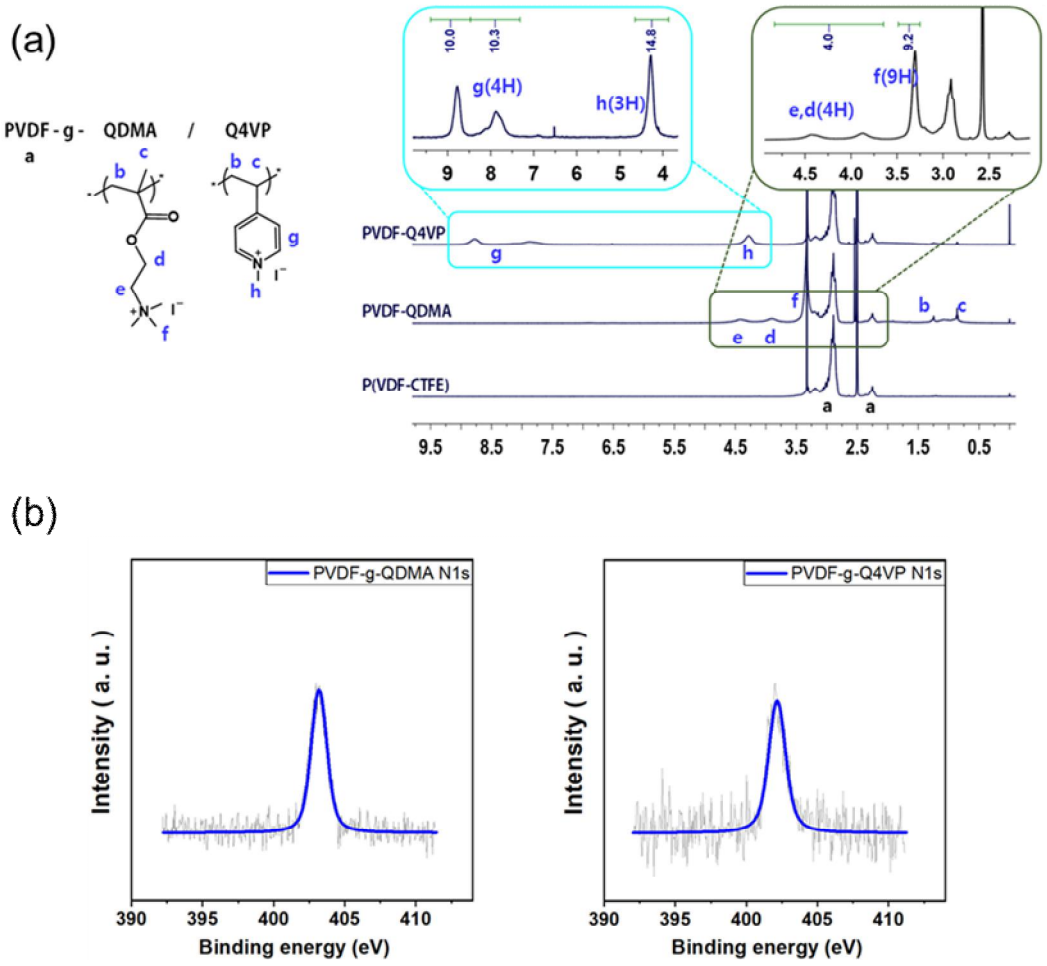

Figure 3.2 (a) ^{1}H NMR spectra of PVDF-g-QDMA, PVDF-g-Q4VP, and P(VDF-CTFE), and integrals of characteristic peaks, (b) XPS N_{1s} spectra of PVDF-g-QDMA (left) and PVDF-g-Q4VP (right)

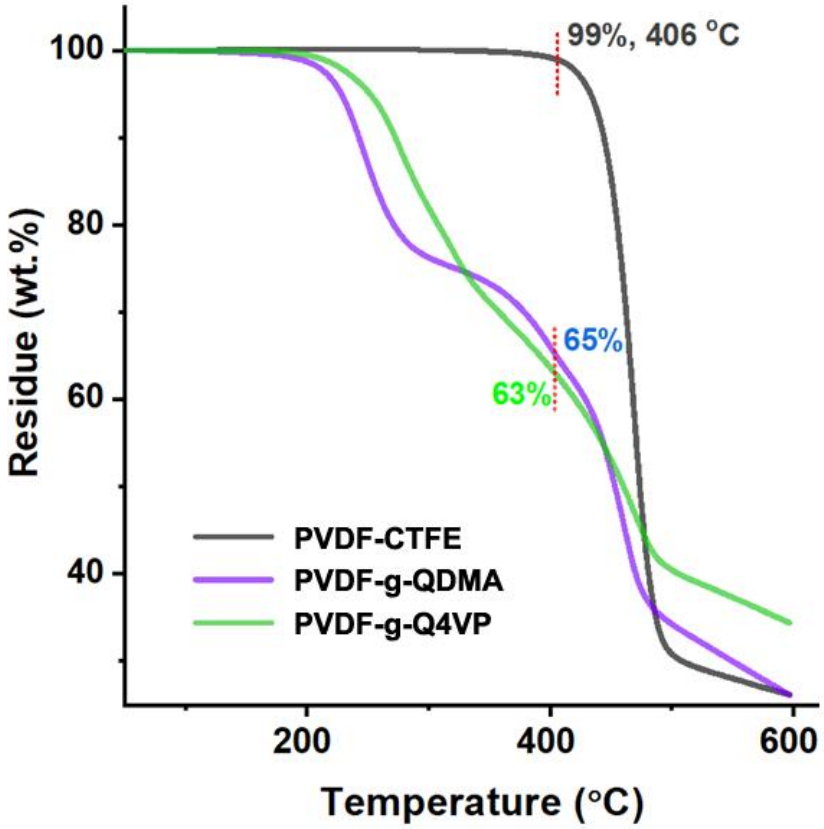

Figure 3.3. TGA curves of PVDF-g-QDMA, PVDF-g-Q4VP and P(VDF-CTFE)

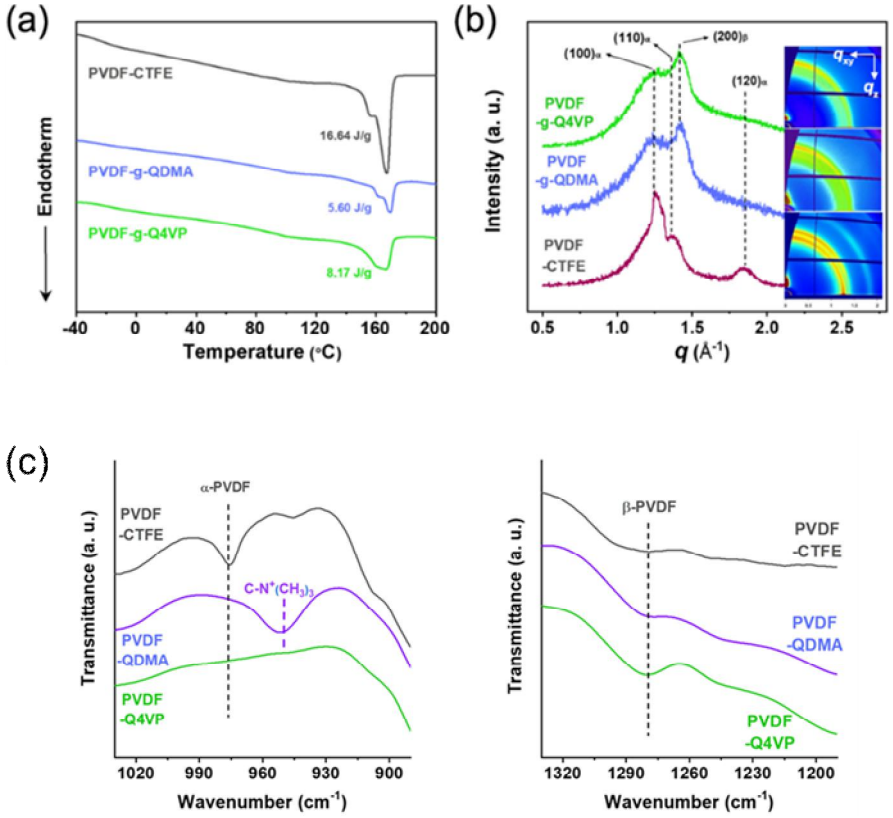

Figure 3.4. (a) DSC curves and (b) 1D GIWAXD patterns of PVDF-g-QDMA, PVDF-g-Q4VP, and P(VDF-CTFE) (inset images: 2D GIWAXD diffractograms). (c) FT-IR spectrum of PVDF-g-QDMA, PVDF-g-Q4VP and P(VDF-CTFE) around α phase (left) and β phase (right) characteristic peaks

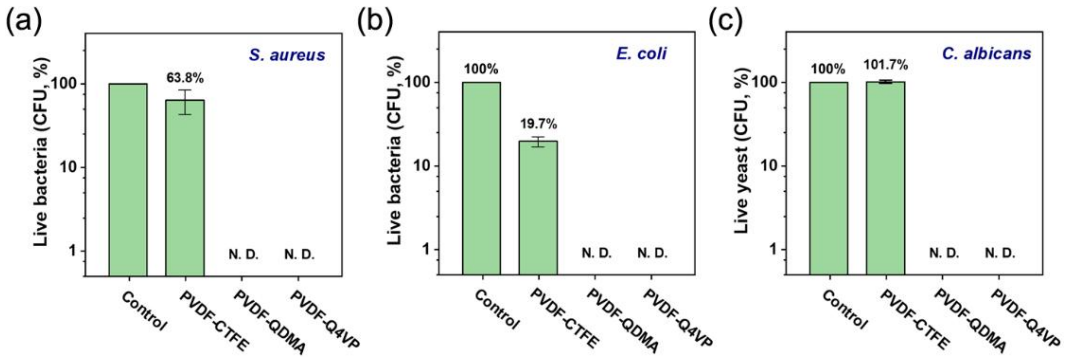

Figure 3.5. Proportion of live microbes on the cationic grafted polymers and P(VDF-CTFE) against (a) *S. aureus*, (b) *E. coli*, and (c) *C. albicans*.

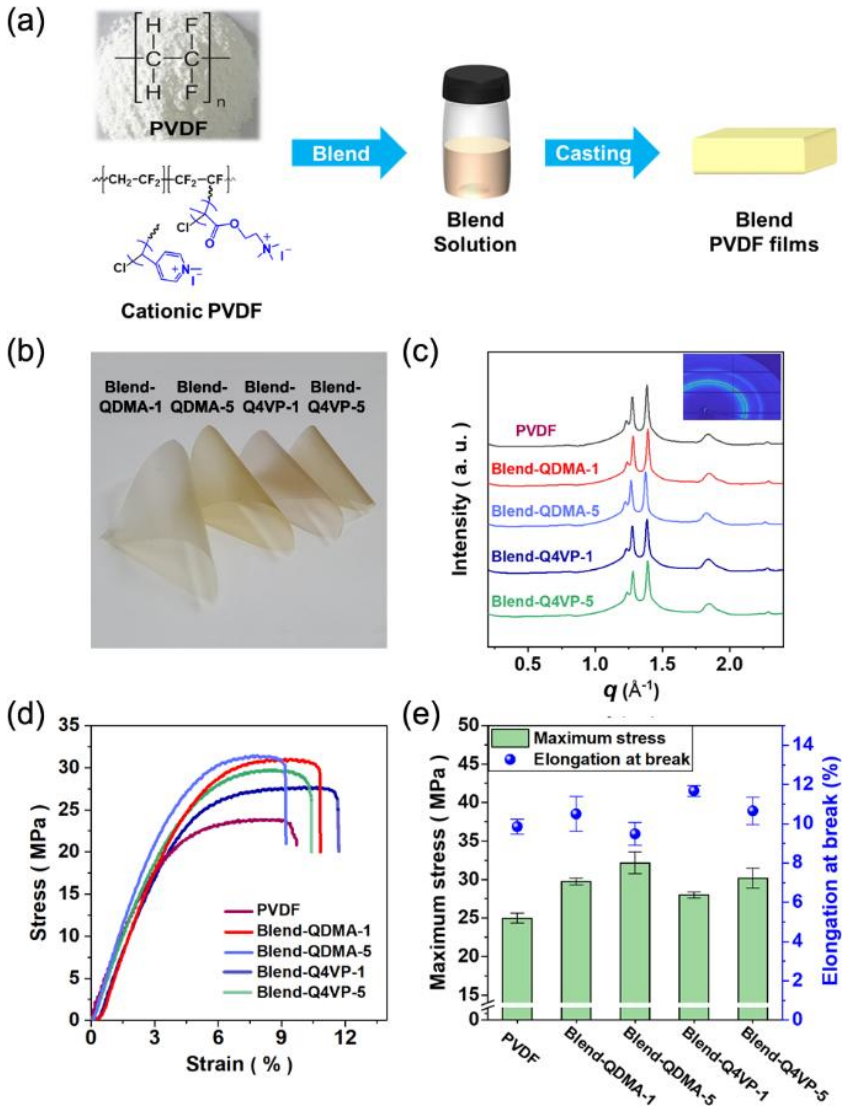

Figure 3.6. (a) Schematics of the fabrication process of PVDF-based blend films, (b) Images of flexible PVDF-based blend films, (c) 1D WAXD patterns of PVDF blend films (inset image: representative 2D WAXD diffractogram), (d) stress–strain curves, and (e) mechanical properties of PVDF and blend films

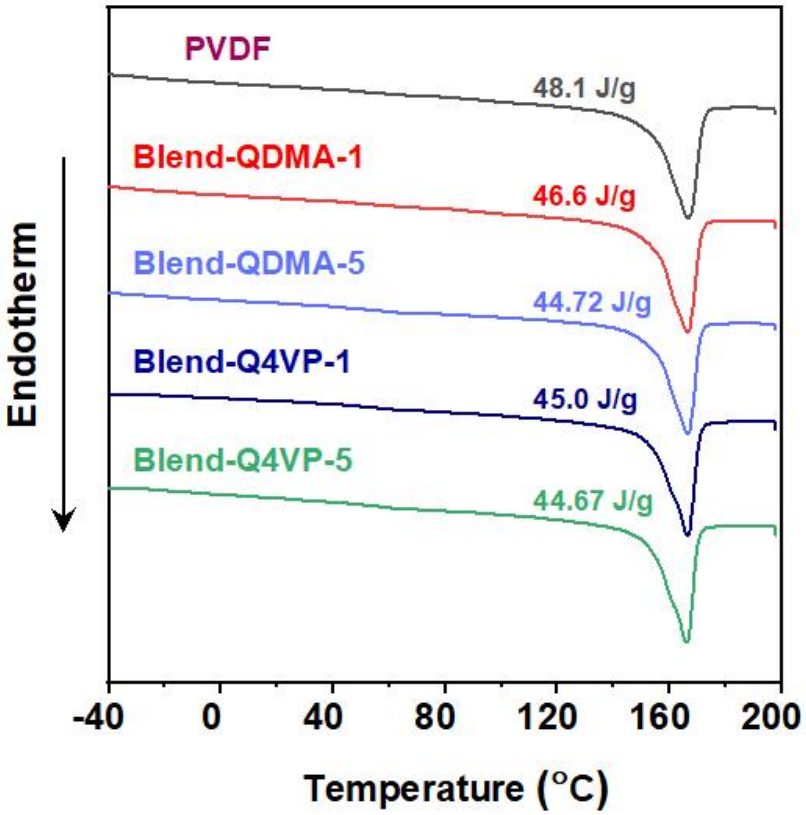

Figure 3.7. DSC profiles of PVDF and blend films

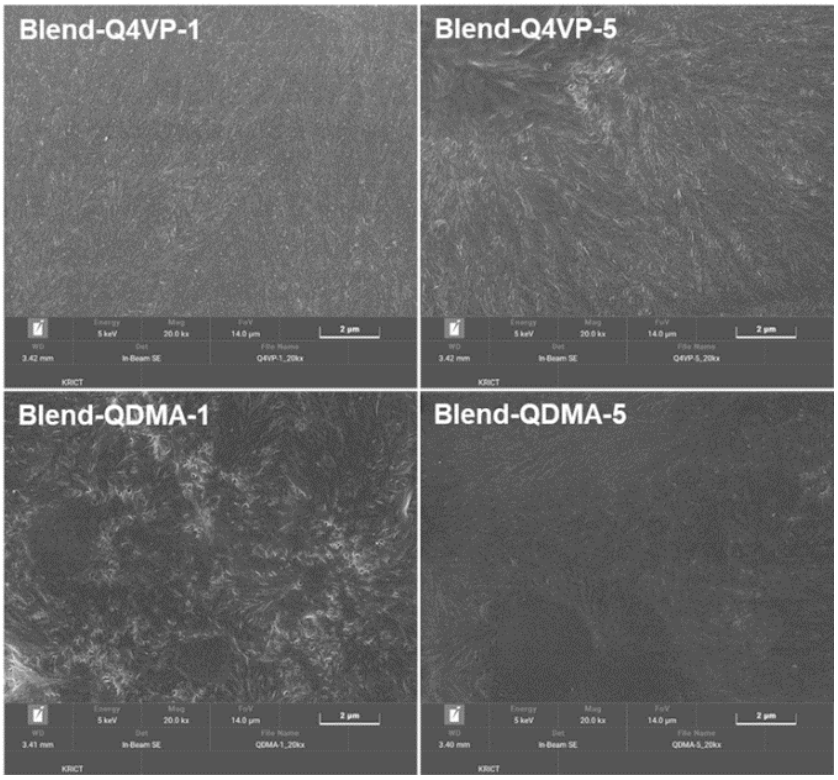

Figure 3.8. SEM images of blend films

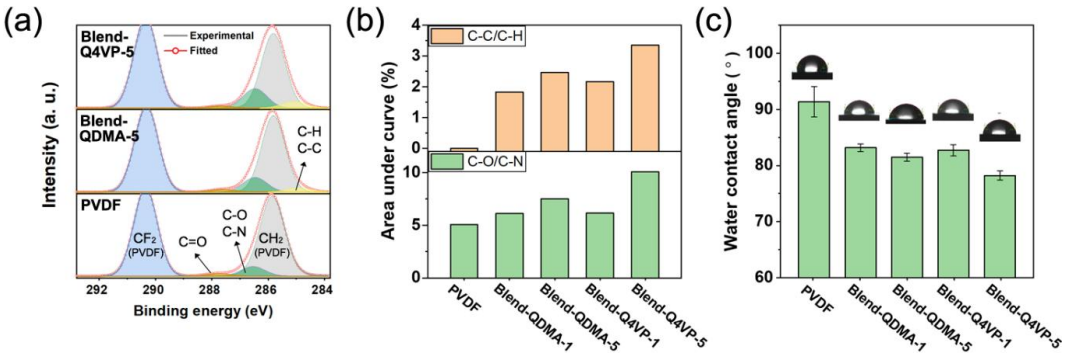

Figure 3.9. (a) XPS C_{1s} spectra for PVDF, Blend-QDMA-5, and Blend-Q4VP-5 and (b) the corresponding calculated areas for the C–C/C–H and C–O/C–N peaks, and (c) water contact angles of PVDF and the blend films

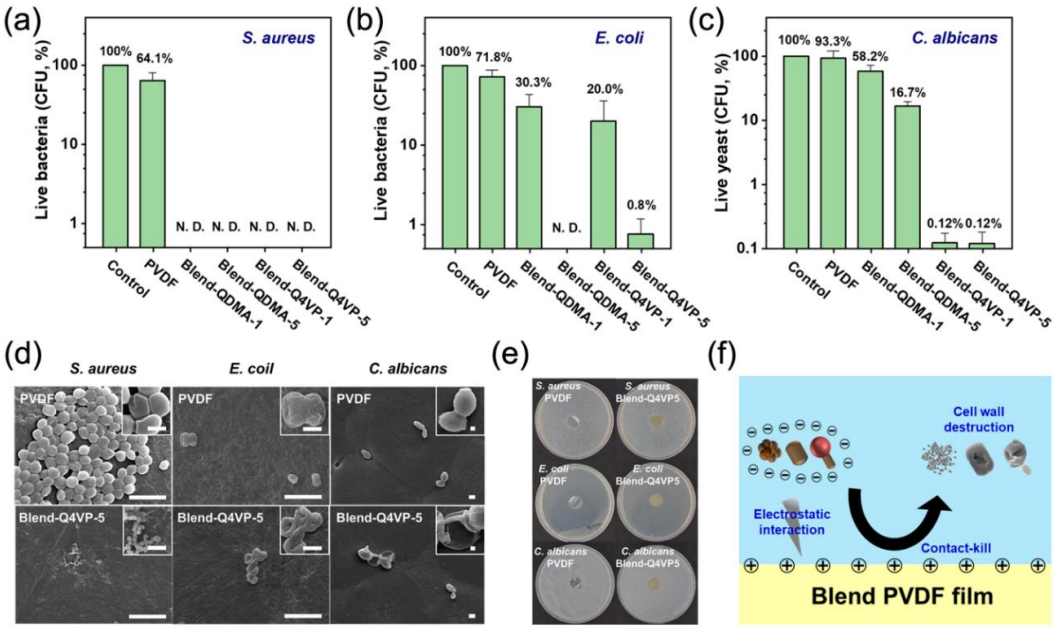

Figure 3.10. Proportion of live microbes on PVDF and blend films against (a) *S. aureus*, (b) *E. coli,* and (c) *C. albicans* (d) SEM images of microbes on pristine PVDF and Blend-Q4VP-5 films (scale bar = 2 μm, inset : 0.5 μm), (e) Inhibition zone of pristine PVDF and Blend-Q4VP-5 films, and (f) Diagrammatic sketch of the antimicrobial mechanism

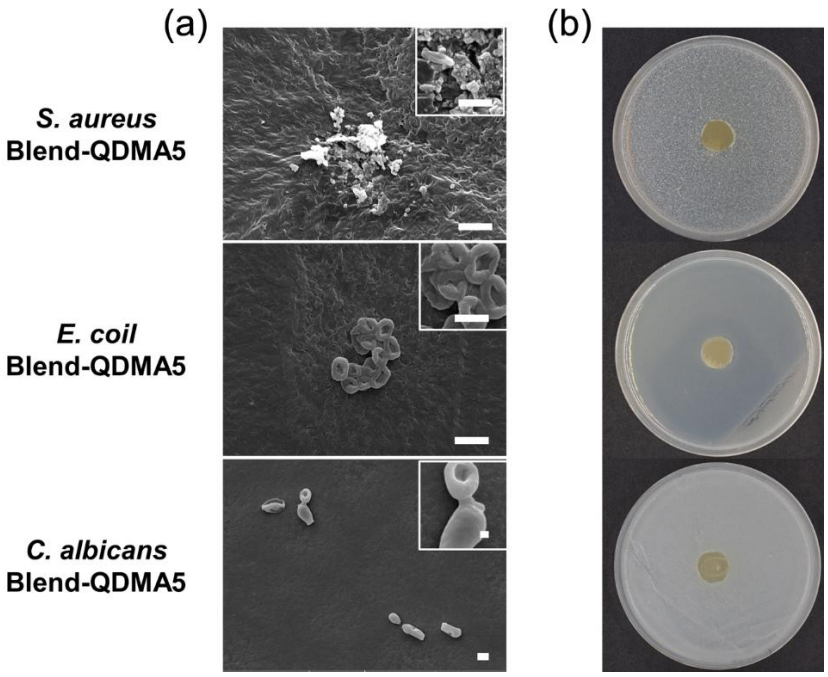

Figure 3.11. (a) SEM images of microbes on Blend-QDMA-5 films (scale bar = 2 μm, inset : 0.5 μm), (b) Inhibition zone of Blend-QDMA-5 films

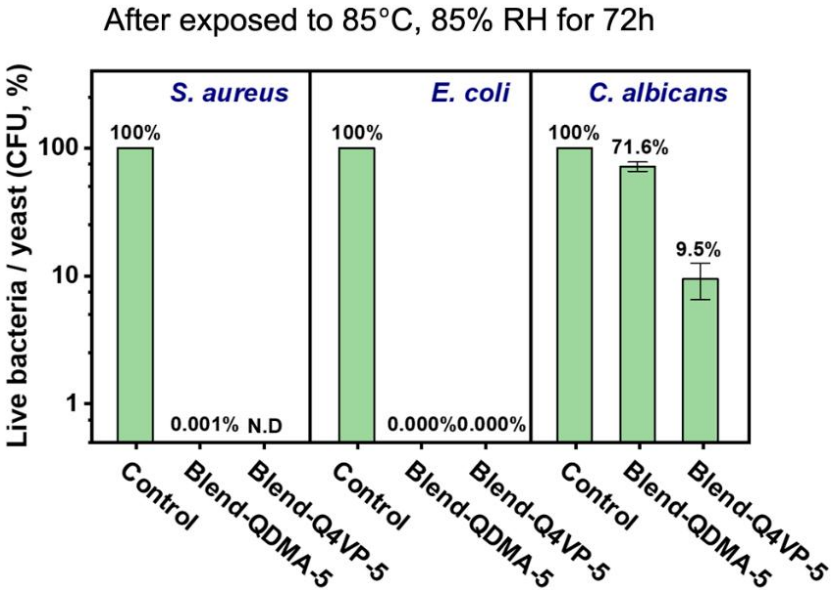

Figure 3.12. Antimicrobial rates of Blend-QDMA-5 and Blend-Q4VP-5 films after exposed to harsh environment

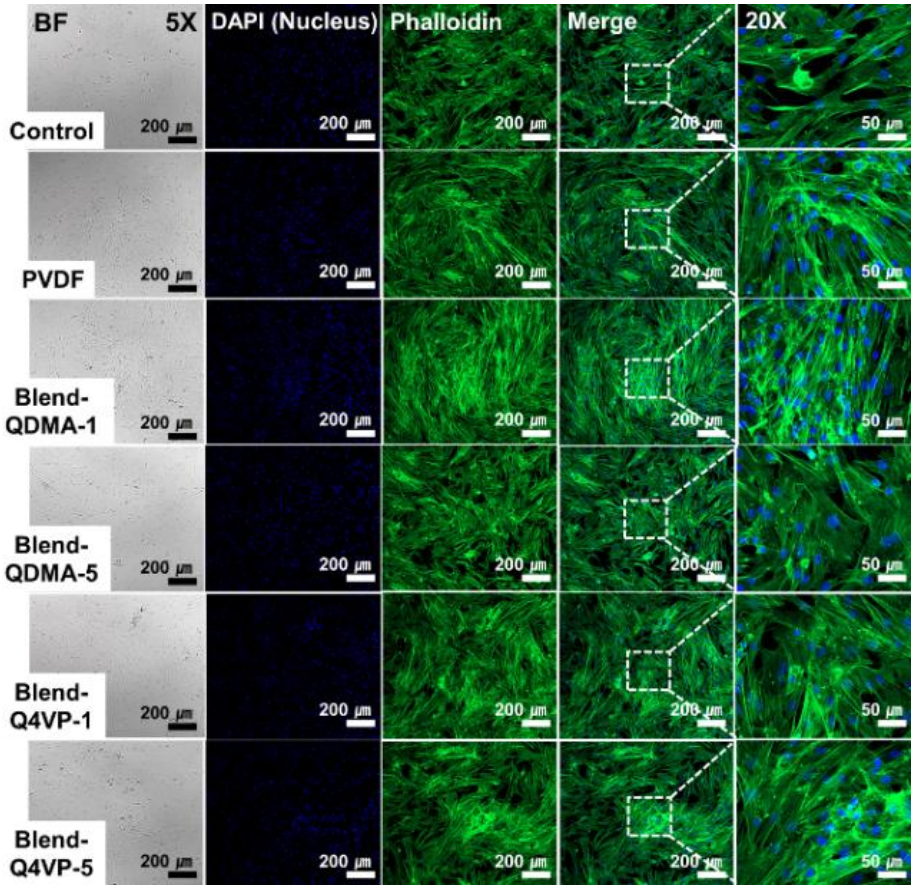

Figure 3.13. Bright-field and immunofluorescence images of HCME cells cultured with PVDF and blend films for 2 days. The nucleus and actin cytoskeleton were immunostained by DAPI (blue) and phalloidin (green)

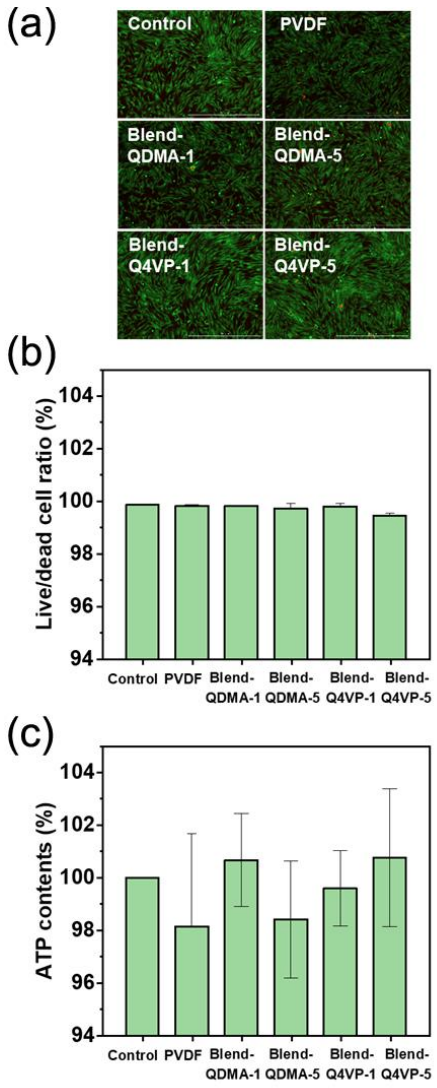

Figure 3.14. Viability characterization of HCME cells with PVDF and blend films for 2 days. (a) Live (green)-Dead (dead) fluorescence images of the cells, (b) Live/Dead cell ratio quantified from the fluorescence images (c) Relative ATP contents of the cells in comparison to the control (HCME cells only)

Chapter 4

Ionic PVDF-based additive with biofouling mitigation and bactericidal activity for fabricating high-performed antifouling membrane

4.1. Introduction

As the importance of water resources has been highlighted, the utilization of water treatment technologies is becoming imperative.[1,2] Membrane separation technology is at the forefront in the water treatment field since it has comparative advantages in terms of treatment efficiency, energy consumption, and operation convenience.[3,4] The polymeric membranes occupy a pivotal role in this process, and it is made of polymers such as PVDF, PAN, PSf, cellulose derivatives, and PTFE depending on its use.[5,6] Among the materials, PVDF is one of the preferred polymers owing to its high mechanical stability, chemical inertness, and processibility.[2,7] However, the innate hydrophobicity of this fluoropolymer is depicted as a drawback since hydrophobic surfaces are easily subject to underwater contamination.[8,9] Particularly, it is vulnerable to biofoulants because hydrophobic-hydrophobic interaction facilitate the adherence of proteins and bacteria. Under practical conditions, biofouling can deteriorate the filtration efficiency and even cause proliferation of microorganisms and pathogenic infection.[10,11] Hence, numerous methods have been employed to mitigate bio-contamination, such as proper module structure, pretreatment of filtrate, chemical cleaning, and making antifouling membranes.[6,12] Among them, designing membranes with inherent anti-biofouling properties were considered as one of the

effective answer in aspects of maintenance cost, filtration efficiency, and long-term usability.[13,14]

Numerous studies have been reported to fabricate biofoulant-resistant PVDF membrane, and these studies largely imparted two properties to the membrane: i) biofouling-resistant property, and ii) biocidal property.[10,11] In the former strategy, membranes were hydrophilic-modified to inhibit the adhesion between surfaces and foulants. Typically, PEG[15,16] and zwitterionic groups[17,18] are introduced to form a hydration layer, and it is known to be effective against fouling of oil, protein, and bacteria. However, for long-term use where a certain amount of adhesion is inevitable, this approach is not suitable because the proliferation of attached microbe is unpreventable.[19,20] In the latter strategy, membranes does not prevent biological contamination, but inhibits proliferation by killing or inactivating attached microorganisms. The membranes were decorated with biocidal materials such as cationic charged groups[20–22] and inorganic particles,[10,23,24] which kills microorganisms by contact-killing or release-killing mechanism.[11,25] However, biocide-functionalized membranes exhibit little effect against contaminants such as protein and dead bacteria, resulting in deterioration of performance.[4,18]

For the prolonged membrane life span, it is insufficient to implement single antifouling or biocidal property.[19,25,26] Therefore, PVDF membranes with

hybrid properties (both antifouling and biocidal) are regarded as promising next-generation strategy. This complementary scope have been achieved by following approaches: coating,[9,27] surface grafting,[4,13,28] and polymer blending.[29,30] Unlike other approaches that require multi-step reactions or additional processes, the polymer blending method only involves single-step of mixing.[5,31] Simplicity makes this approach versatile and suitable for large scale application or industrial use. However, compatibility or solubility issue may arise between the PVDF matrix and additives, which narrows the window of applicable polymers.[15,20] Particularly, their utilization has been curtailed because hydrophilic ionic polymers are not soluble in common solvents[17,32] or hardly miscible with hydrophobic PVDF.[33] Poor miscibility can adversely affect the homogeneity of the structure, and consequently attenuates the performance of the membranes.[34] Furthermore, some ionic polymers are leachable in aqueous solutions which make them unsuitable for practical water treatment conditions.[8,33] Considering that ionic functionalities exhibit the paramount antifouling or antibacterial characteristics,[14,17,21] overcoming these obstacle is critical for designing biofouling-inert blend membranes.

Therefore, in this study, we aimed to develop ionic polymer additives and PVDF membranes with dual antifouling and bactericidal properties. To avoid incompatibility, additives were designed to share PVDF backbone structure by

covalent grafting of ionic monomers into P(VDF-CTFE). Two different polymers were synthesized: PVDF with cations (PVDF-QDMA) and PVDF with cations and zwitterions simultaneously (PVDF-QDMA/MPC). Consistent with our previous work,[35] synthesized additives are well-soluble in DMSO, and compatible with PVDF matrix. With additive contents of 5 wt% or 10 wt%, PVDF blend membranes were fabricated via non-solvent induced separation (NIPS) method. The influence of the ionic additives on blend membranes was investigated by comparing membrane characteristics, fouling resistances, and bactericidal activities. Owing to incorporated quaternary ammonium part, all the membranes possess antibacterial activity against both gram-positive and –negative bacteria. However, when it comes to fouling resistance, zwitterionic containing PVDF-QDMA/MPC additive shows superior property than cationic PVDF-QDMA. Especially, membrane with 10 wt% of PVDF-MPC/QDMA showed remarkable performance in both antibacterial and fouling-resistant aspects.

4.2. Experimental

Materials

Industrial grade P(VDF-CTFE) with 15 wt% CTFE was provided from Solvay and PVDF (Kynar 761) was supplied from Arkema. Acetone (HPLC grade), Cu(I)Cl (99.99 %) phosphate buffer saline (PBS), bovine serum albumin (BSA), and all the NMR solvents were obtained from Sigma-Aldrich. 2-methacryloyloxyethyl phosphorylcholine (MPC, 97%) was procured from Henan Tianfu Chemical (China). Iodomethane (99%) was obtained from Samchun chemicals (South Korea) and dimethyl sulfoxide (DMSO, HPLC grade) was sourced from Duksan chemicals (South Korea). N,N,N',N'',N''-Pentamethyldiethylenetriamine (PMDTA, 99%) and (dimethylamino)ethylmethacrylate (DMAEMA, 98.5%) were received from TCI chemicals (Japan). All the reagents were used as received unless noted. Preparation procedure of 2-(methacryloyloxyethyl)trimethylammonium iodide (QDMA), the cationic monomer, is as follows. One-neck 250 mL flask with DMAEMA (11.2 g) and 60 mL of acetone were placed in ice bath. Iodomethane (10.6 g) was slowly injected with stirring and then the reaction was proceeded at 25 °C for 3 h. White powdery product were washed with acetone several times and obtained (yield >95%).

Synthesis of graft copolymers

QDMA and MPC monomers were graft onto P(VDF-CTFE) by chlorine initiated ATRP. In 250mL schlenk flask, 9g of QDMA monomer (or 2.5 g of MPC and 5g of QDMA) was dissolved in 150g of 4wt % of P(VDF-CTFE)/DMSO solution. After degassing, CuCl (0.3g) was introduced into the flask and the solution was further degassed by vacuum-nitrogen exchanges until 0.62 mL of PMDTA was injected. The reaction was proceeded at 90 °C under nitrogen atmosphere. After 24 h, the solution was cooled down to room temperature and precipitated in ethanol. The precipitate was purified by washing in DI water for several times. About 9g of polymers were obtained and named as PVDF-QDMA or PVDF-MPC/QDMA.

Fabrication of blend PVDF membranes

Membrane preparation procedures were illustrated in Figure 4.1. Mixture of PVDF and PVDF-based graft copolymers were dissolved in DMSO at 80 °C to make 18 wt% homogenous solutions. DMSO was selected as the solvent because it could dissolve both PVDF and additives, and the amount of copolymer additives were set as 5 or 10 wt% to total solid. After complete dissolution, polymer solutions were left overnight to remove bubbles. The resulting solutions were uniformly cast onto non-woven fabric (Novatexx 2471), using a bird type

applicator (TQC, 200μm gap) at the speed of 1 inch/sec. After 10 sec after casting, the plates were immersed into a water bath of 30 ± 2 °C to precipitate out the polymer. The membranes were kept in the water bath for 30 min and then moved to fresh deionized water bath. Fabricated membranes were named M-C# when PVDF-QDMA was used, and M-ZC# when PVDF-MPC/QDMA was used (# : 5 or 10, weight fraction of additives). Pristine PVDF membrane was also fabricated (M-0), and recipes of all the membranes are described in Table 4.1. Except for the filtration experiments, the fabricated membranes were air-dried for characterization.

Characterization

The chemical structures were analyzed by NMR spectroscopy (Bruker Avance, 500 MHz for ^{1}H, 471 MHz for ^{19}F NMR). DMSO-d_6 and TMS as a solvent and internal standard, and small amount trifluoroacetic acid-d was used to shift H_2O peak. The Fourier transform infrared (FTIR) spectra were recorded by FT/IR-4100 spectrophotometer (Jasco) under transmission mode or Nicolet 5700 spectrophotometer (Thermo) under ATR mode. Thermogravimetric analysis (TGA, Q5000, TA Instruments) was conducted under N_2 atmosphere. Temperature was ramped at 10 °C min^{-1} in the range of room temperature to 600 °C. Differential scanning calorimetry (DSC, Q1000, TA Instruments) was conducted in the

temperature range of -50 to 200 °C at a heating rate of 10 °C·min^{-1}. X-ray photoelectron spectroscopy (XPS) was performed using surface analysis system (AXIS SUPRA, Kratos). To investigate the surface and cross-section morphologies, membranes were coated by platinum and then observed by Scanning Electron Microscopy (SEM, Tescan MIRA 3, 10 kV). The surface topologies were obtained by SPA 400 atomic force microscope (AFM) (Seiko, Japan) with a SPI 3800 controller, using a NCH-10 probe (Nanoworld, Switzerland). For an area of 10 × 10 μm^2, analysis was conducted at a scan rate of ~1 Hz using non-contact mode. The water contact angles were measured at room temperature and ambient relative humidity using a DSA100 goniometer with ADVANCE software (Krüss). Measurements were performed by dispensing 4μl of water (sessile drop) or 6μl of air (captive bubble) onto the membrane surfaces and at least four different results were averaged. The surfaces zeta potentials were measured by zeta potential analyzer (SurPASS 3, Anton Paar, Austria). The measurement was carried out in a 1 mM NaCl solution at 25 °C, and varied pH condition by using 1 M HCl or NaOH The mean pore sizes and their distributions were examined by a capillary flow porometer (Porolux 1000, Porometer NV) with Porefil liquid (16 mN/m).

Membrane filtration experiments

All filtration performances were measure with cross-flow filtration setup (ASTM E1343-90) with effective filtration area of 13.4 cm^2 (Figure 4.2). A pre-filtration step was performed under 1 bar using a PBS buffer solution to compact and stabilize the membrane. Then, pure water filtration was performed by filtering deionized water at 1 bar, and the weight of permeate was recorded by balance (UW6200H, shimadzu). Pure water flux (J_0) was calculated by the Eq. (1)

$$J\ (L\ m^{-2}\ h^{-1}\ bar^{-1}) = \Delta V / (A \times \Delta t \times \Delta p) \quad (1)$$

Where ΔV is the permeate volume (L), Δt denotes the filtration time, and A is the effective membrane area (m^2). Secondly, dynamic fouling test were conducted to assess the antifouling properties of the membranes. PBS solution containing 500 ppm BSA is selected as feed solution. Fouling test is conducted in four steps : i) determining initial water flux, ii) filtering protein solution, iii) cleaning membranes and module with deionized water, and iv) filtering pure water again. Fouling resistances of each membrane was evaluated by flux recovery ratio (FRR, %) which is calculated by the Eq. (2)

$$FRR\ (\%) = J_1/J_0 \times 100 \quad (2)$$

Where J_0 denotes initial water flux and J_1 denotes recovered water flux measured in step iv). Reversible flux decline (R_r, %) and irreversible flux decline (R_{ir}, %) caused by organic fouling are determined by Eq. (3) and Eq. (4).

$$R_r\ (\%) = (J_1 - J_2)/J_0 \times 100 \quad (3)$$

R_{ir} (%) = (J_0 – J_1)/J_0 × 100 (4)

Where J_2 is flux for BSA feed solution

Antibacterial experiments

Antibacterial properties were measured against gram-positive *Staphylcococcus aureus* (*S. aureus*, ATCC 6538), and gram-negative *Pseudomonas aeruginosa* (*P. aeruginosa*, ATCC 9027). Bacteria were cultivated in nutrient agar (NA) at 32 °C for 24 h and the strain suspensions of 10^6 colony forming unit (CFU)/mL were prepared by appropriate dilution. To evaluate the antimicrobial characteristics, 0.4 mL of each suspension was dropped on a 5 cm × 5 cm sterilized membranes at 32 °C. After 24 h, the bacteria on the membranes were transferred into the petri dish by 10 mL of nutritional broth. Subsequently, the strain solutions were serially diluted and grown for 24 h at 32 °C. Afterwards, the emerging colonies were counted and bactericidal rate (%) was calculated as bactericidal rate = $(1 - CFU_{experimental}/CFU_{control}) \times 100$ %, where $CFU_{control}$ and $CFU_{experiment}$ are the numbers of viable microbe on positive control and sample film. In this experiment, sterilized PET films were used as positive control according to the ISO 22196 standard. Results were obtained from more than three different measurements and averaged. Bacterial adhesion tests were examined against *P. aeruginosa*. Strain suspensions of 10^7 CFU/mL were inoculated on the M-0, M-C10, and M-ZC10

membranes. After 24 h of cultivation, membranes were rinsed by PBS and adhered bacteria were fixed by 2.5 % glutaraldehyde at 4 ℃ for 18 h. Typical EtOH dehydration processes were conducted on membranes and dried. Finally, samples were sputter-coated by platinum and then observed by MAGNA FEG SEM (10 kV, Tescan). The numbers of adherent bacteria were counted form multiple SEM images and quantified.

4.3. Results and discussion

Two ionic monomer sets were introduced into PVDF backbone: i) only cationic QDMA, ii) both zwitterionic MPC and cationic QDMA. Note that PVDF with only zwitterionic MPC was also synthesized, but not included in this study since it is insoluble to any common solvents. Figure 4.3a illustrate the synthetic procedure of ionic-functionalized PVDF additives and their chemical structures. PVDF with cationic graft units are terms as PVDF-QDMA, and PVDF with both cationic and zwitterionic units were named as PVDF-MPC/QDMA, respectively. Chemical structures were identified by ^{1}H NMR spectroscopy (Figure 4.3b). Each peak except for P(VDF-CTFE) unit is assigned to protons in QDMA or MPC, and composition of polymers were investigated by comparing these peaks. Table 4.2 describes the calculated compositions in weight fraction. The grafted parts account for ~ 40 wt%, and QDMA to MPC ratio in PVDF-MPC/QDMA is determined to be 52:48. These results are corroborated by XPS elemental analysis which give comparable results (Table 4.3). A presence of ionic parts was also confirmed by FTIR spectra (Figure 4.3c). New peaks at 884 and 1402 cm^{-1} were observed from the specta of synthetic polymers since both QDMA and MPC monomers bear quaternary ammonium group. [35] Also, owing to the presence of zwitterionic MPC, phosphonate group peaks (1090 and 1240 cm^{-1})[36] are

observed in PVDF-MPC/QDMA spectrum. Additionally, appearance of N_{1s} and/or P_{2p} peak in the XPS spectra (Figure 4.3d) can be an evidence of incorporated ionic unit.

To assess the hydrophilicity, water contact angles were measured by the deposition of water droplets or air bubbles on the polymer coated glasses (Figure 4.4a). In addition to the typical sessile drop method, captive bubble contact angles were also embraced because the arrangement of ionic polymer is different in dry and wet conditions.[34] By the introduction of ionic branch, hydrophobic P(VDF-CTFE) is converted to hydrophilic. Under air environment, lower contact angle of 32.1° is observed in PVDF-MPC/QDMA than PVDF-QDMA (59.4°) which can be an evidence of more hydrophilic nature of zwitterionic group than cationic group.[18,37] Interestingly, both ionic PVDF polymers exhibited very low contact angles (<20°) in captive bubble method. These results indicate that both ionic additives are highly hydrophilic in fully wet state, demonstrating their potential in fouling-resistant modifiers.

The bactericidal activities of PVDF-QDMA and PVDF-MPC/QDMA were measured by film attachment method, by counting bacterial colonies after cultivation.[9,38] This experiment was conducted against gram-positive *S. aureus* and gram-negative *P. aeruginosa* (Figure 4.4b and c). In comparison with control sample, both polymers were proven to eradicate all the bacteria efficiently,

whether gram-positive or negative. Bactericidal property is on account of incorporated cationic QDMA since zwitterionic groups and PVDF-based polymers do not have bacteria-killing activities.[35,37] Consequently, it can be believed that synthesized polymers with excellent hydrophilicity and antibacterial properties can be applicable in various fields including membrane preparation.

Synthesized ionic polymers were used as additives and blend PVDF membranes were cast with 5 wt% or 10 wt% additives. The top and cross-sectional morphologies of the resulting membranes were examined by SEM (Figure 4.5a and b). The top of pristine PVDF membrane shows a relatively dense surface with little porosity while all the blend membranes show porous surfaces. This porous structure can be concomitant to incorporation of additives whose hydrophilic parts act as a pore-forming agent.[39,40] Cross-sectional SEM images show typical asymmetric membrane structures comprising dense skin layers and sublayers with macrovoids. In line with the surfaces, more porous structures were developed in the blend membranes, implying that the ionic additives improved the affinity between solvent and non-solvent.[32,41] Over all the images, macrophase separation of additives from the PVDF matrix is not presented. The homogeneous surfaces indicate the good compatibility of synthesized additives although they contain significant amount of ionic parts (~40 wt%). Shared PVDF backbone structure can be ascribable to this well-miscibility and this feature is imperative

for membrane performance since heterogeneous parts may cause malfunction of membranes.[34,39] Morphology of membrane surfaces were also investigated by AFM (Figure 4.5c) and their roughness data is sorted in Figure 4.5d. AFM results revealed that the roughness of the blend membranes is lower than the M-0. Even though the influence of the additive type or amount was not clear, sub-micron sized roughness was mainly observed in blend membrane samples, whereas M-0 possesses bigger sized roughness. This can be attributable to the nanosized pores on the blend membrane surfaces, which is consistent with the SEM results.

XPS analysis was conducted to assess the membrane surfaces, and N_{1s} narrow spectra are shown in Figure 4.6a. Unexpectedly, nitrogen peak at 398 eV is observed on the spectrum of pristine PVDF membrane. Given the chemical structure of PVDF, nitrogen peak can be considered as erroneous peak. However, note that the industrial grade PVDF can be co-formulated with hydrophilic modifier,[34] and therefore, it can be inferred that used PVDF has nitrogen containing modifier. Since nitrogen is not observed in powder state PVDF (Figure 4.7), this peak can be originated from the surface segregation of trace modifier. All blend membranes exhibit the N_{1s} peak at 402 eV which is a characteristic peak of the quaternized nitrogen species. Therefore, peaks at 402 eV could be evidence of cationic or zwitterionic groups on the surfaces,[35] and it can be considered that the outermost surfaces (~10nm) are mainly covered with ionic additives as

the peak at 398eV is almost invisible. Surface segregation of ionic groups is also revealed by FTIR-ATR spectra (Figure 4.8). Ester and quaternary ammonium peaks emerge on blend membrane spectra and their intensities increase as more additives are formulated (M-C10 or M-ZC10). In case of the P_{2p} XPS spectra (Figure 4.6b), peaks were only observed on the M-ZC5 and M-ZC10 samples corroborating the presence of PVDF-MPC/QDMA additive on the surface.

Since the surface charge of the membrane is an important factor determining the antibacterial or antifouling properties, electric state of surfaces was investigated by zeta potential analyzer. As plotted in Figure 4.6c, pristine M-0 show overall negative zeta potential, which is consistent with typical behavior of hydrophobic PVDF membrane.[4,32] Exploitation of ionic additives rapidly changes the surface charges owing to the strongly positive QDMA. Quaternary ammonium on the surface can make the surface more positive, and shift the isoelectric point to higher pH region. This tendency is clearly exhibited in M-C10 and M-C5 samples on account of highly cationic PVDF-QDMA additive. These surfaces have noticeably positive charges, and their isoelectric points appear at pH 9.97 and 8.06, respectively. Meanwhile, the influence of PVDF-MPC/QDMA is not as great as PVDF-QDMA because zwitterionic MPC possess neutral charge, not positive. Hence, the isoelectric points of M-C10 and M-C5 membranes drop to 7.43 and 5.73, but higher than pristine PVDF membrane. Notably, almost neutral M-ZC10

seems to be advantageous in fouling-resistant property since neutral charge is preferred for constructing antifouling surfaces against broad-spectrum of foulants.[8]

The hydrophilicity of the membrane was evaluated by contact angle measurement (Figure 4.6d). Considering the actual condition, the captive bubble method was adopted rather than the sessile drop.[42] Compared to the contact angle of the pristine PVDF membrane (60.1°), blend membranes show lower contact angle. This demonstrate that ionic additives are segregated on the surface regardless of the additives although hydrophilicity of the membranes is influenced by the amount or type. Increasing the feed of additive to 10 wt% led to a clear improvement in hydrophilicity, and the utilization of zwitterion-containing additive can make further impact. This result is reasonable considering that the zwitterionic group is generally more hydrophilic than cationic one.[18,37] Consequently, M-ZC10 membrane is expected to show best antifouling properties owing to its superb hydrophilicity and almost neutral electric charge.

The pore size distributions and mean pore size of membranes are displayed in Figure 4.6e and f. In all the membranes, most of the pores possess a size between 40nm and 80nm. The mean flow pore diameters are in the range of 54.6 to 69.5 nm though trend according to the type or amount of additive are not distinct.

The pure water fluxes of the different membranes were measured by cross-flow

apparatus and results were presented in Figure 4.9a. The pristine M-0 membrane show the lowest pure water flux of 75.4 L m^{-2} h^{-1} bar^{-1} which is attributable to low porosity and innate hydrophobicity. Ionic additives significantly improve water flux to about 300 L m^{-2} h^{-1} bar^{-1}, nearly four times that of M-0. The type or amount of additive do not have a substantial effect on permeability as all the membranes show comparable flux performances. Among all, M-ZC5 membrane marked the highest permeance of 351.3 L m^{-2} h^{-1} bar^{-1} which can be correlated with the pore size of the membrane (Figure 4.6f).[32,43]

Fouling resistance was evaluated by dynamic fouling test, and BSA was selected as the model foulant. BSA is widely used as a biological or organic foulant surrogate, and they tend to block the membrane pores by adhesion.[33] The normalized flux profiles are plotted over time in Figure 4.9b. In filtration experiments, the flux of the membranes sharply decline once the feed was switched to BSA solution. This reduction of flux is mainly ascribable to pore blockage on the membrane surfaces which can be induce by both tightly- and loosely-bound foulants. After BSA filtration, membranes were hydraulically cleaned and the feed was switched back to pure water. In this process, loosely bound proteins were removed and the fluxes were recovered to some extent. From filtration profiles, corresponding fouling factors are calculated from the Eq. (2-4) and exhibited in Figure 4.9c to estimate the antifouling property more

comprehensively. After 30 minutes of BSA filtration, the highest total flux decline (R_r + R_{ir}) was observed in M-ZC5, but most of the decay was found to be recovered through washing. Therefore, flux reduction is mainly originated from loosely bound foulants or foulants larger than the pores which can induced the temporary pore clogging by forming cake layer of pollutants.[12,23] Regarding irreversible fouling, R_{ir} is simultaneously influenced by hydrophilicity and surface charge, and the ratios follows the order of: M-C10 > M-0 > M-C5 > M-ZC5 > M-ZC10. Since hydrophobicity facilitate the adhesion of contaminants under aquatic environment, M-0 membrane marked high R_{ir} of 40.1 % due to innate hydrophilicity. Interestingly, hydrophilic M-C10 (contact angle: 44.2°) exhibited the highest R_{ir} of 49.1 %. This is due to the strong surface positive charge of M-C10 as unveiled in zeta potential curve (Figure 4.6c). Under the current filtration condition (PBS, pH 7.4), foulant BSA has a negative charge, which can make an electrostatic interaction with the positive surfaces.[8,32] As a result of electrostatic interaction, the majority of BSA on surface can tightly adhered to the membrane and be hardly removed by simple cleaning. Meanwhile, in case of M-ZC10 membrane, irreversible fouling is not observed, and flux was fully recovered after BSA filtration process. This indicates that almost all foulant deposited on the membrane is loosely bound or temporarily layered on the surface. Excellent fouling resistance of M-ZC10 is realized thanks to highly hydrophilic

surface (contact angle: 39.6°) and almost neutral surface charge (isoelectric points: 7.43) which are essential requisite of enhanced antifouling property.[14,18] For further characterization of antifouling property, three consecutive filtration cycles were proceeded against M-0 and M-ZC10 membranes (Figure 4.10). M-ZC10 membrane showed marginal FRR reduction in the first two cycles, and flux and FRR values were still above 80.0% after third cycle.

The antibacterial properties of the membranes were investigated against gram-positive *S. aureus* and gram-negative *P. aeruginosa* and the results are displayed in Figure 4.11a, b. By virtue of the incorporated ionic additives, blend membranes exhibit improved bacteria killing ability compared to pristine M-0. Apparently, bactericidal activity is ascribed to cationic moiety on the surfaces which can eradicate various microbes by contact-killing mechanism.[22,37] Positive-charged surfaces can make electrostatic interactions with negative-charged bacterial cell wall[4,21,35] that induce the rupture of bacterial cytomembranes and leakage of intracellular contents.[22,24] Therefore, the blend membranes showed better antibacterial performance to *P. aeruginosa* than *S. aureus* although the pure ionic polymers were highly effective to kill both bacteria (bactericidal activity > 99.99%). When comparing the membranes with 5 wt% additives, it was observed that M-C5 showed more than 99.9 % and M-ZC5 of 90.1 % bactericidal rates

against *S. aureus*. In case of gram-negative *P. aeruginosa*, pristine M-0 did not show any antibacterial properties at all. Although membranes with ionic additives show better antibacterial properties, M-C5 and M-ZC5 showed insufficient bactericidal rates of 69.9% and 60%, respectively. This difference in viability could be originated from the structural difference of the species.[21,44] Gram-negative bacteria are known to have a complex structure across the cell wall which can protect the intracellular structure. Therefore, they are better able to survive on contact killing surfaces compared to gram-positive ones. In case of membranes with 10 wt% additive (M-C10 and M-ZC10), however, more than 99.9% of antibacterial properties are achieved regardless of the species. Even though the surface charge of M-ZC10 is almost neutral, this result demonstrate that cationic groups on the surface can impart sufficient biocidal activity when 10 wt% of additive is incorporated. Therefore, these membranes have potential to effectively inhibit bio-contamination in water treatment processes.

Furthermore, bacterial adhesion on the membranes were examined because not only live but also dead bacteria on the surfaces can deteriorate the long-term water treatment efficiency.[19,20] Tests were conducted on M-0, M-C10, and M-ZC10 samples and anti-adhesion property was evaluated by observing membrane surfaces after bacteria incubation (Figure 4.11c). Gram-negative *P. aeruginosa* was selected as model bacteria for the reason that it showed better viability in

prior tests. SEM microscopic images show that considerable number of bacteria were adhered on the surface of M-0. Bacteria adsorption was reduced in M-C10, and adherent bacteria were hardly observable in M-ZC10. Adhesion can be related to the hydrophilic nature of the membranes, especially for M-ZC10 which possess highly hydrophilic and biofouling-repellent zwitterionic group on the surface.[9,14] By investigation of the bacterial morphologies, the contact-killing activity of the blend membranes were also verified, as displayed in insets of Figure 4.11c. *P. aeruginosa* on M-0 have intact and smooth shapes which were fully enveloped by cell wall. Meanwhile, the outer profiles of bacteria on M-C10 and M-ZC10 samples were deformed or contracted, implying that the cell wall has been destroyed and lysed.[24,44] Therefore, it can be expected that the proliferation of bacteria will hardly occur on these membranes. From the multiple SEM images, the number of adherent bacteria were quantified and averaged in Figure 4.11d. The number of adherent bacteria on M-ZC10 membrane was reduced by more than 95% compared to pristine M-0, and by more than 85% compared to cationic M-C10. Consequently, M-ZC10 membrane with both cationic and zwitterionic groups exhibited the remarkable performances in the aspect of biocidality and fouling resistance.

4.4. Conclusion

In this study, PVDF membranes containing cationic part or zwitterionic-co-cationic part was developed. Firstly, two different PVDF-based additives were strategically designed and synthesized via atom transfer radical polymerization to impart on-demand functions of antibacterial property and/or fouling resistance. Secondly, ionic group decorated membranes was fabricated by simple polymer blending followed by conventional NIPS method. Only 5 wt% or 10 wt% of additives were utilized to make dope solutions, and five different membranes with varied composition were fabricated. Regardless of type or contents, incorporation of additives make blend membranes more porous and further improves pure water fluxes. However, hydrophilicity and electric state of surface were varied according to the type or contents of additives and consequently influence the fouling resistance or bactericidal property. Among the membranes, M-ZC10 exhibit high hydrophilicity and electric neutrality owing to balanced structure of quaternary ammonium and zwitterionic MPC. Consequently, M-ZC10 exert superb fouling resistance (FRR: ~100%) and bactericidal activity against *S. aureus* and *P. aeruginosa* (>99.9%). Furthermore, bacterial fouling was reduced by more than 95% compared to pristine PVDF, indicating that it has potential for use in long-term water treatment applications.

4.5. References

[1] H.B. Park, J. Kamcev, L.M. Robeson, M. Elimelech, B.D. Freeman, *Science* 2017, 356, 138–1148.

[2] D. Zou, Y.M. Lee, *Prog. Polym. Sci.* 2022, 128, 101535.

[3] R.P. Lively, D.S. Sholl, *Nat. Mater.* 2017, 16 276–279.

[4] M.M. Zhu, Y. Fang, Y.C. Chen, Y.Q. Lei, L.F. Fang, B.K. Zhu, H. Matsuyama, *J. Colloid Interface Sci.* 2021, 584, 225–235.

[5] N.H. Ismail, W.N.W. Salleh, A.F. Ismail, H. Hasbullah, N. Yusof, F. Aziz, J. Jaafar, *Sep. Purif. Technol.* 2020, 233, 116007.

[6] S.P. Nunes, P.Z. Culfaz-Emecen, G.Z. Ramon, T. Visser, G.H. Koops, W. Jin, M. Ulbricht, *J. Membr. Sci.* 2020, 598, 117761.

[7] Z. Cui, E. Drioli, Y.M. Lee, P*rog. Polym. Sci.* 2014, 39, 164–198.

[8] S.Y. Wang, L.F. Fang, H. Matsuyama, *J. Membr. Sci.* 2020, 597, 117766.

[9] K. Cheng, N. Zhang, N. Yang, S. Hou, J. Ma, L. Zhang, Y. Sun, B. Jiang, *Sep. Purif. Technol.* 2021, 262, 118316.

[10] M. Mukherjee, S. De, *Environ. Sci. Water Res. Technol.* 2018, 4, 1078–1104.

[11] J. Wang, J. Lu, Y. Zhou, Y. Zhou, 2021, 1, 479–497.

[12] S. Huang, R.H.A. Ras, X. Tian, *Curr. Opin. Colloid Interface Sci.* 2018, 36, 90–109.

[13] J. Yang, X. Zhu, J. Lin, Q. Wang, L. Zhang, N. Yang, L. Lin, J. Zhao, Y. Zhao, L. Chen, *ACS Appl. Polym. Mater*. 2022, 4, 229–239.

[14] S.K. Lau, W.F. Yong, *ACS Appl. Polym. Mater.* 2021, 3, 4390–4412.

[15] X. Zhou, Y. Sun, S. Shen, Y. Li, R. Bai, *Membranes.* 2021, 11, 951.

[16] S. Wang, T. Li, C. Chen, S. Chen, B. Liu, J. Crittenden, *Appl. Surf. Sci.* 2018, 435, 1072–1079.

[17] S.H. Tang, A. Venault, C. Hsieh, G.V. Dizon, C.T. Lo, Y. Chang, *J. Membr. Sci.* 2020, 598, 117655.

[18] C. Zhang, J. Zhou, X. Ye, Z. Li, Y. Wang, *Macromolecules.* 2021, 54, 4236–4245.

[19] C.-Y. Chiu, T.-J. Yen, Y. Chang, *Chem. Eng. J.* 2022, 440, 135798.

[20] M. Ping, X. Zhang, M. Liu, Z. Wu, Z. Wang, *J. Membr. Sci.* 2019, 570–571, 286–293.

[21] C. Andersen, J. Madsen, A.E. Daugaard, *Macromol. Rapid Commun.* 2021, 42, 1–27.

[22] R. Kaur, S. Liu, *Prog. Surf. Sci.* 2016, 91, 136–153.

[23] Y. Pan, Z. Yu, H. Shi, Q. Chen, G. Zeng, H. Di, X. Ren, Y. He, *J. Chem. Technol. Biotechnol.* 2017, 92, 562–572.

[24] C. Geng, L. an Fan, H. Niu, L. Liu, F. Zhao, J. Zhang, H. Dong, S. Yu, *Mater. Sci. Eng. C*. 2021, 131, 112517.

[25] E.N. Durmaz, S. Sahin, E. Virga, S. De Beer, L.C.P.M. De Smet, W.M. De Vos, *ACS Appl. Polym. Mater.* 2021, 3, 4347–4374.

[26] Y. Zhan, S. Yu, A. Amirfazli, A. Rahim Siddiqui, W. Li, *Adv. Eng. Mater.* 2021, 2101053, 1–22.

[27] Q. Lin, L. Wu, W. Hu, X. Wan, Z. Wu, C. Zhang, *Surfaces and Interfaces.* 2022, 29, 101708.

[28] J. Zhao, J. Yang, Y. Li, D. Li, Q. Wang, L. Zhang, Y. Zhang, S. Zhang, L. Chen, *Eur. Polym. J.* 2020, 135, 109883.

[29] K. Gao, Y. Su, L. Zhou, M. He, R. Zhang, Y. Liu, Z. Jiang, *J. Membr. Sci.* 2018, 548, 621–631.

[30] X. Li, B. Wu, H. Chen, K. Nan, Y. Jin, L. Sun, B. Wang, *J. Mater. Chem. B.* 2018, 6, 4274–4292.

[31] H. Wu, T. Li, B. Liu, C. Chen, S. Wang, J.C. Crittenden, *Appl. Surf. Sci.* 2018, 455, 987–996.

[32] S. Shen, L. Zhang, Y. Zhang, G. Zhang, J. Yang, R. Bai, *J. Appl. Polym. Sci.* 2020, 137, 1–8.

[33] P. Kaner, E. Rubakh, D.H. Kim, A. Asatekin, *J. Membr. Sci.* 2017, 533, 141–159.

[34] P. Kaner, A. V. Dudchenko, M.S. Mauter, A. Asatekin, *J. Mater. Chem. A*. 2019, 7, 4829–4846.

[35] D. J. Han, S. Kim, H. J. Heo, C. Jin, J. Kim, H. Choi, I. J. Park, H. S. Kang, S. G. Lee, J.-C. Lee, E.-H. Sohn, *Appl. Surf. Sci.* 2021, 562, 150181.

[36] G. Han, J.T. Liu, K.J. Lu, T.S. Chung, *Environ. Sci. Technol.* 2018, 52, 6686–6694.

[37] X. Zhang, L. Liu, W. Peng, X. Dong, Y. Gu, Z. Ma, D. Gan, P. Liu, *J. Mater. Chem. B.* 2021, 9, 4169–4177.

[38] X. Zhang, Y. Liang, C. Ni, Y. Li, *Mater. Sci. Eng. C.* 2021, 118, 111411.

[39] F. Chen, X. Shi, X. Chen, W. Chen, *Appl. Surf. Sci.* 2018, 427, 787–797.

[40] S.H. Park, Y. Ahn, M. Jang, H.J. Kim, K.Y. Cho, S.S. Hwang, J.H. Lee, K.Y. Baek, *Sep. Purif. Technol.* 2018, 202, 34–44.

[41] Z. Chen, X.A. Du, Y. Liu, Y. Ju, S. Song, L. Dong, *J. Mater. Chem. A*. 2018, 6, 15191–15199.

[42] Y. Baek, J. Kang, P. Theato, J. Yoon, *Desalination.* 2012, 303, 23–28.

[43] D.H. Choi, S. Kwon, Y. Yoo, I.C. Kim, H. Park, Y.I. Park, S.Y. Yang, S.E. Nam, Y.H. Cho, *Membranes,* 2022, 12.

[44] J. Du, Y. Li, J. Wang, C. Wang, D. Liu, G. Wang, S. Liu, *ACS Appl. Mater. Interfaces.* 2020, 12, 26966–26972.

Table 4.1. Profiles of membrane dope solutions in this study

Sample	PVDF (wt%)	PVDF-QDMA (wt%)	PVDF-MPC/QDMA (wt%)	DMSO (wt%)
M-0	18	-	-	82
M-C5	17.1	0.9	-	82
M-C10	16.2	1.8	-	82
M-ZC5	17.1	-	0.9	82
M-ZC10	16.2	-	1.8	82

Table 4.2. Composition profiles of synthesized graft copolymers

	P(VDF-CTFE) backbone (wt%) [a]	QDMA (wt%) [a]	MPC (wt%) [a]
PVDF-QDMA	62	38.0	-
PVDF-MPC/QDMA	60	20.8	19.2

[a)] calculated from ^{1}H NMR

Table 4.3. Characterizations of PVDF-QDMA and PVDF-MPC/QDMA by different analyses.

	Graft part weight ratio (wt%)		*QDMA in graft part (mol%)*		*MPC in graft part (mol%)*	
	NMR	TGA[a]	NMR	XPS	NMR	XPS
PVDF-QDMA	38	36	100	100	0	0
PVDF-MPC/QDMA	40	42	52	48	48	52

[a)] calculated from residual mass at 382 ºC.

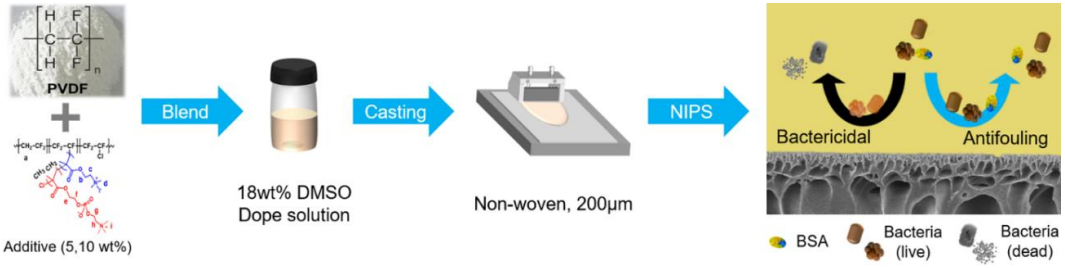

Figure 4.1. Diagrammatic sketch of blend membrane fabrication

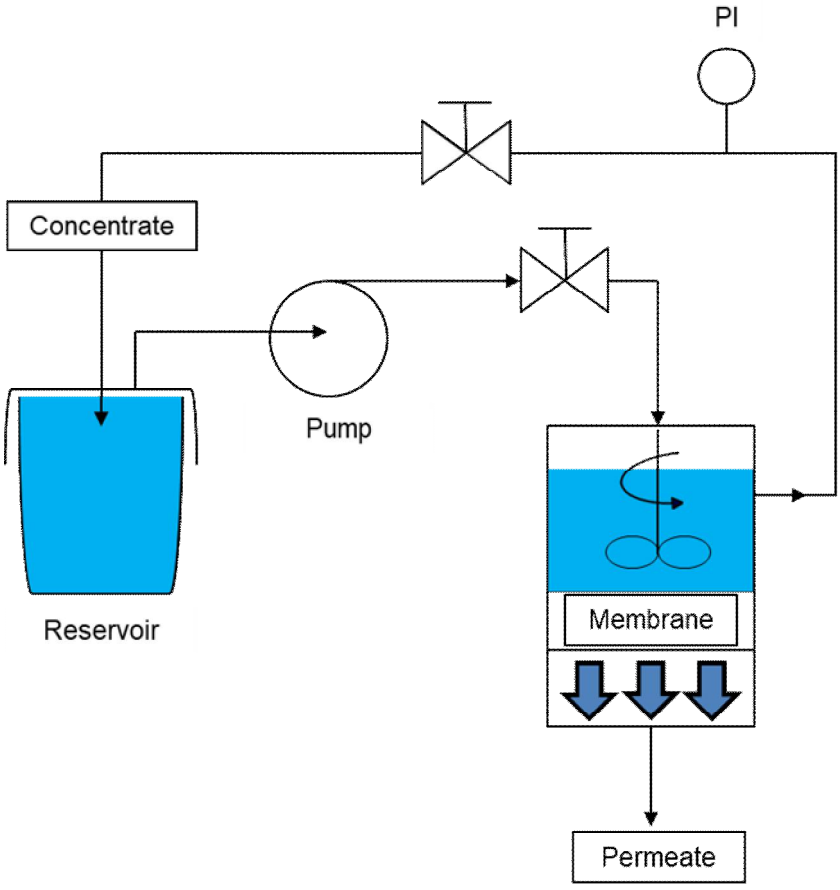

Figure 4.2. Schematic diagram of cross-flow filtration setup

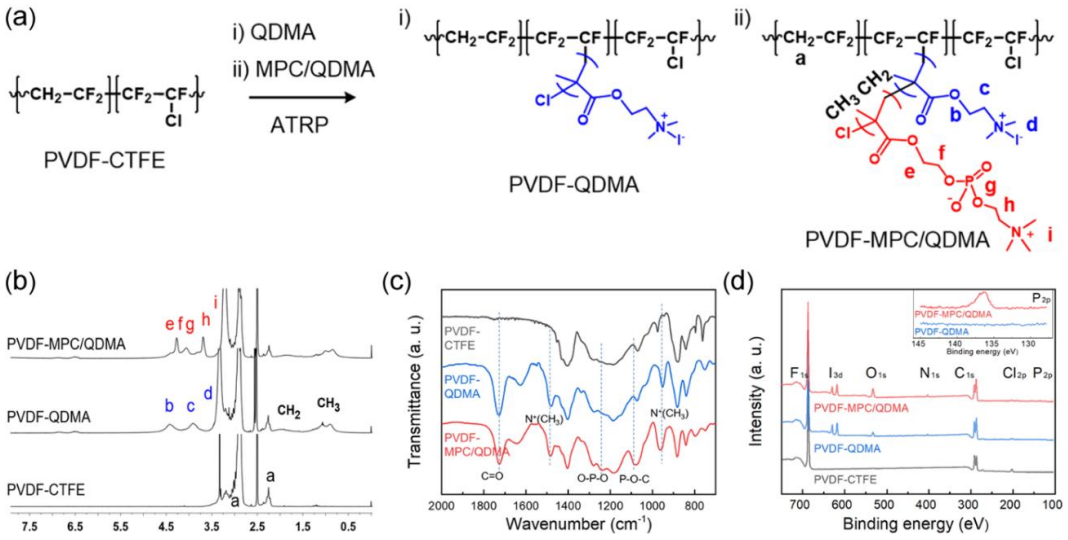

Figure 4.3. (a) Synthetic procedure of PVDF-QDMA and PVDF-MPC/QDMA (b) ^{1}H NMR, (c) FTIR, and (d) XPS spectra of P(VDF-CTFE), PVDF-QDMA, and PVDF-MPC/QDMA (inset : P_{2p} high resolution spectra)

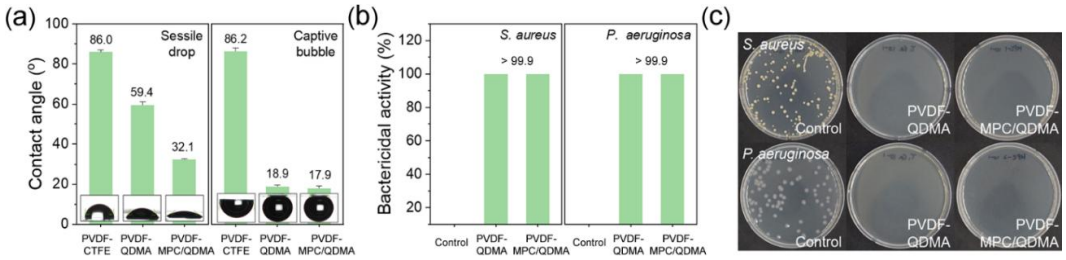

Figure 4.4. (a) Water contact angles of polymer films. (b) Bactericidal ability of polymers against *S. aureus* and *P. aeruginosa*, and (c) agar plate images

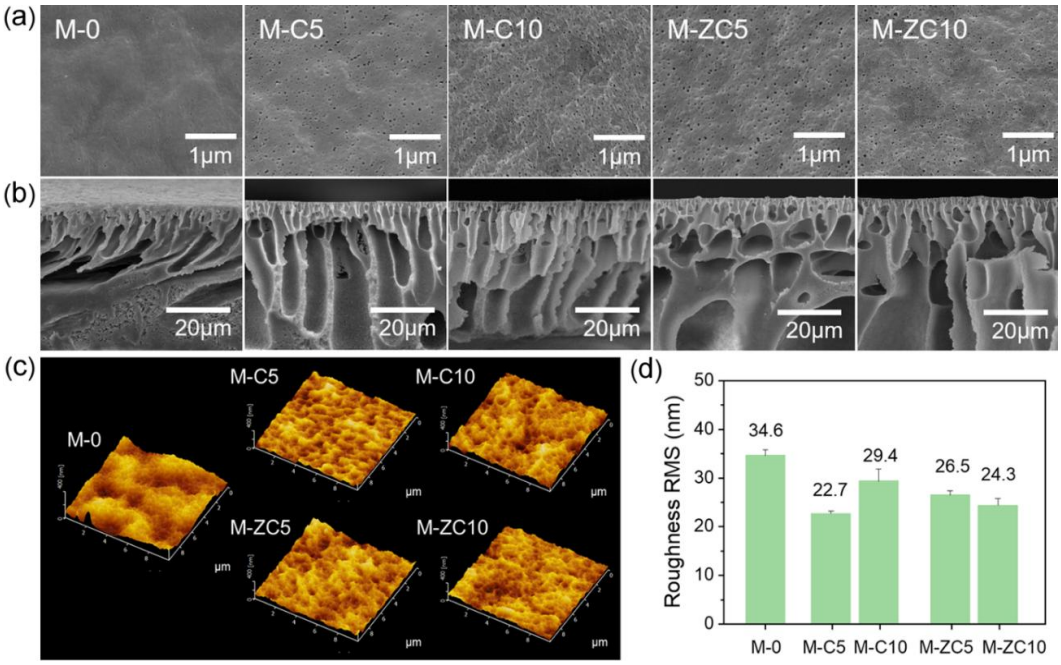

Figure 4.5. (a) Top, and (b) cross-section SEM images of membranes. (c) AFM topographic profiles (d) and RMS roughness of membranes

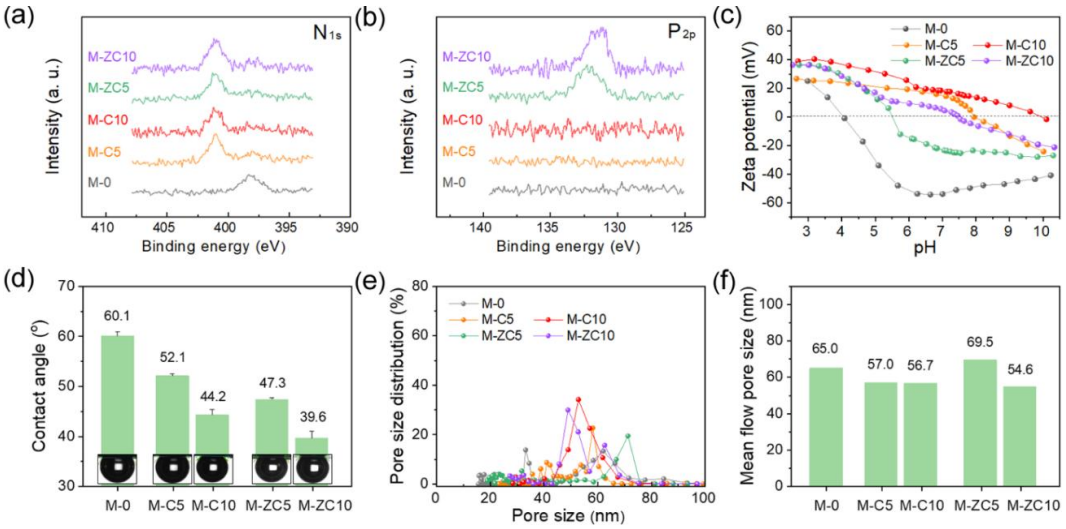

Figure 4.6. XPS (a) N_{1s}, (b) P_{2p} spectrum, (c) zeta potential and (d) water contact angles of membranes. (c) Pore size distribution and (d) mean pore size of membranes

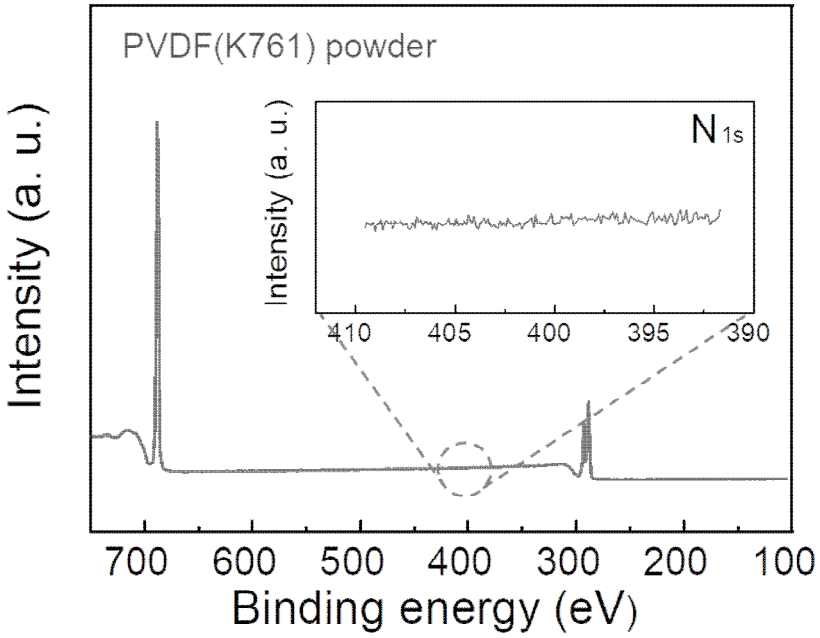

Figure 4.7. Survey and N_{1s} high resolution XPS spectrum of PVDF powder

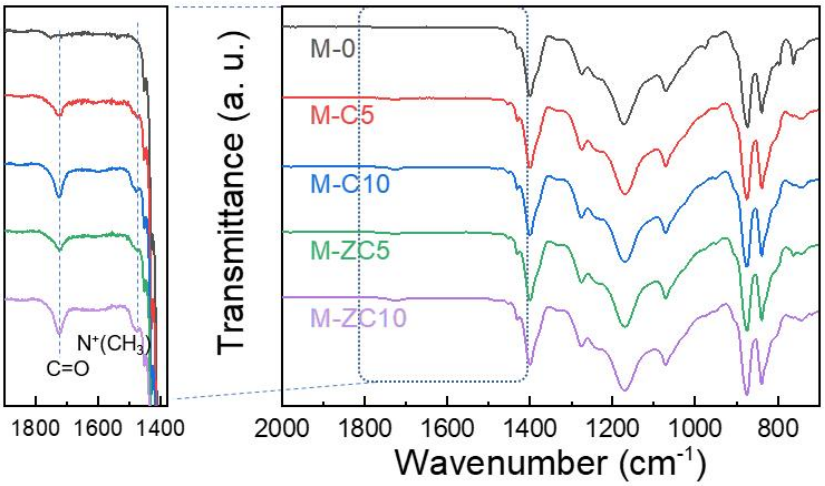

Figure 4.8. FTIR-ATR spectrum of membranes (right) and their magnified spectrum in the range of 1400 - 1900 cm^{-1} (left)

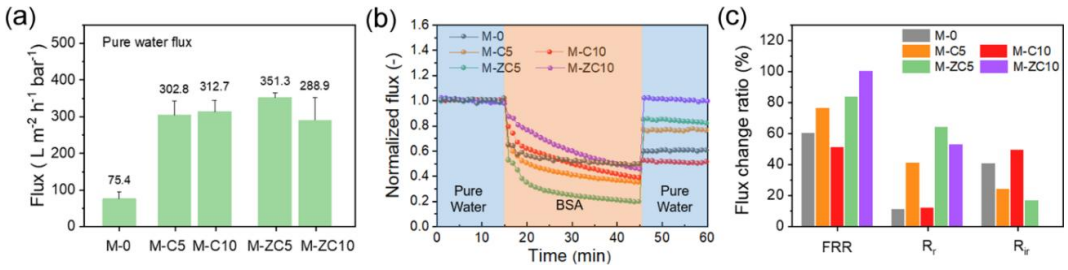

Figure 4.9. (a) Pure water flux, (b) dynamic BSA fouling profiles, and (c) fouling resistance parameters (FRR, R_r, and R_{ir}) of membranes

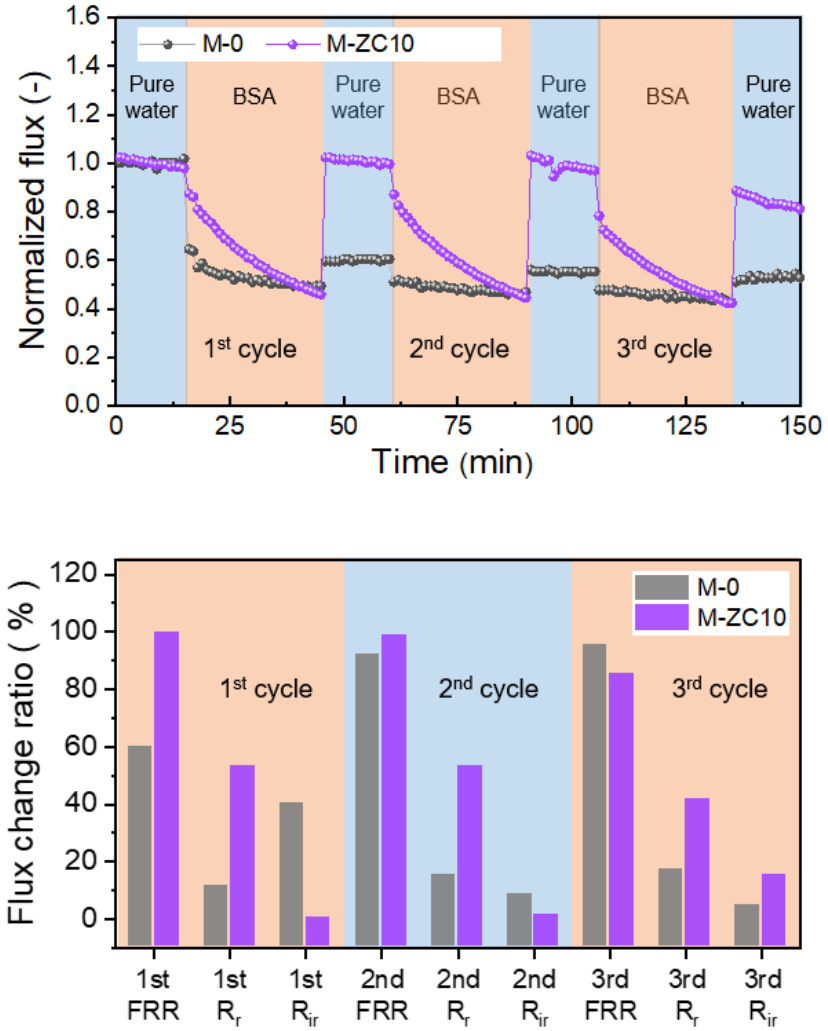

Figure 4.10. Three cycle dynamic BSA fouling profiles (top) and their flux change factors (FRR, R_r, and R_{ir}) of M-0 and M-ZC10 membranes (bottom)

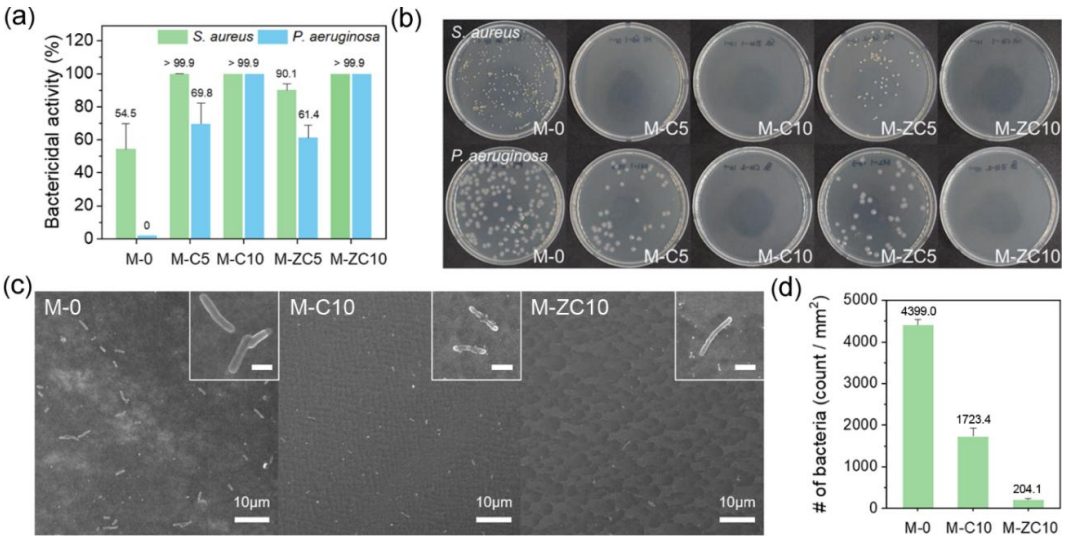

Figure 4.11. (a) Bactericidal activity of membranes against *S. aureus* and *P. aeruginosa*, and (b) agar plate images. (c) SEM images of M-0, M-C10, and M-ZC10 after bacteria adhesion test (inset : magnified *P. aeruginosa*, scale bar = 1μm) and (d) number of adherent *P. aeruginosa*

Chapter 5

Versatile Functionalization of Fluoropolymer via One-pot Thiol Incorporation

5.1. Introduction

VDF-based fluoropolymers have attracted tremendous attention owing to their thermal stability, chemical inertness, weatherability, and excellent mechanical properties finding their finding applications in the fields of water treatment,[1,2] outdoor coatings,[3,4] fuel cell membranes,[5,6] and rechargeable batteries.[7,8] Furthermore, on account of distinctive electrical properties based on their unique structure, VDF-based polymers are also utilized as dielectric,[9] piezoelectric,[10] electroactive,[11] and even electrocaloric devices.[12] These fascinating characteristics are mainly originated from peculiar properties of fluorine atom : low polarizability, high electronegativity, small van der Waals radius, and high strength of C-F bond.[13–15] From the other side of view, however, these characteristics cause ineluctable disadvantages like poor processibility, low miscibility with solvent or other materials, and difficulty in tuning the properties for on-demand applications.[4,14] To compensate the ascribed drawbacks, achieving desired properties through introducing functionality into fluoropolymer have been extensively studied because commercial VDF-based polymers mostly lacks of functionality, and other shortcomings can also be covered by the same strategy.[16]

One approach of introducing functionality is the utilization of functional vinyl

co-monomers and free radical copolymerization with VDF. Copolymerization is a commonly used in the field of polymer chemistry owing to its simplicity of functionalization,[17] and several VDF-based copolymers with desired functionalities have been reported. [4,16,18] However, the reactivity ratio of the VDF which is different from typical vinyl monomers, restrict the scope of co-monomers except for special monomers such as perfluoromethyl vinyl ether[14,19] and 2-(trifluoromethyl)acrylic acid.[4,16,20] In addition, since VDF monomer is in a gaseous state, copolymerization process is also burdened with the synthetic difficulty. The other strategy is modification of commercial fluoropolymers by chemical pathway. Compared to direct copolymerization, this approach broaden the scope of introducible functionality and also offers the advantages of relatively facile synthetic process and economic competitiveness.[21] Therefore, the latter method has been widely utilized to prepare the on-demand functionalized fluoropolymers while retaining their original attractive properties.[22]

Numerous chemical methods have been used, among which graft modification using ATRP has received much attention since the report by Hester *et al.* in 2002.[23] Because various fluoropolymers such as PVDF,[7,23] P(VDF-CTFE),[24,25] PVDF-TrFE[22] and even nafion[26] can be involved, this approach have been widely employed to prepare functional fluoropolymers with

enhanced performance. Nevertheless, immanent disadvantages such as sensitive reaction conditions and residual catalyst make ATRP process uncompetitive in large-scale production and industrial application.[21] Functionalization using nucleophiles is also one of the well-known methods of modifying VDF-based fluoropolymers. Nucleophiles such as amines and thiols are introduced into the fluoropolymer backbone through nucleophilic addition[27] or substitution,[28] and these have been frequently utilized to crosslink fluoropolymers or to prepare fluoropolymer based elastomers in both academia and industry.[29–31] However, since the nucleophile can causes uncontrollable dehydrofluorination in the VDF segment[10,32] and multi-step is sometimes required for functionalization,[1,33] a facile reaction route under mild conditions needs to be further studied.

Herein, in effort to introduce functionality onto VDF-based fluoropolymer, fluoropolymer P(VDF-CTFE) is functionalized with thiols. P(VDF-CTFE) was selected because chlorine atoms in the CTFE sequence have selective reactivity. Using tertiary amines as the sole catalyst, varied functional groups were successfully introduced into the fluoropolymer by one-step mild reactions, and the properties of resulting polymers were investigated. In addition, through model reactions with hydroxyl thiol, the amount of introduced functional groups were studied as a function of reagent input, time, solvent, and other conditions. This one-pot reaction involves the three different reactions of double bond formation,

thiol-Michael addition into double bond, and nucleophile substitution. Notably, the sites for nucleophile substitution are proposed with the aid of quantum chemistry and comparison reaction with other fluoropolymers. Thanks to the simplicity of the reaction, this functionalization system is expected to be a promising strategy that facilitates the molecular engineering of VDF-based polymers and further broadens their applicability.

5.2. Experimental

Materials

P(VDF-CTFE) with 15wt% CTFE (1.3mM of CTFE unit in 1.0 g) was purchased from Polyk Technologies (PA, United states). Triethylamine (TEA, 99.5%), sodium 3-mercapto-1-propanesulfonate (90%), 3-Mercaptopropionic acid (99%), 2-(Dimethylamino)ethanethiol hydrochloride (95%), n-butylamine (99.5%), 1H,1H,2H,2H-perfluorodecanethiol (97%), 1-methyl imidazole (MI, 99%), 1,4-Diazabicyclo[2.2.2]octane (DABCO, 99%), and triethyl phosphate (TEP, 99.8%) were obtained from Sigma-Aldrich. 3-Mercapto-1-propanol (97%), 1-hexanethiol (96%), and 4-(Trifluoromethyl)benzenethiol (98%) were provided from TCI chemicals (Japan). N-methyl-2-pyrrolidone (NMP, 99.5%), dimethyl sulfoxide (DMSO, HPLC grade), and dimethylformamide (DMF, HPLC grade) were sourced from Samchun chemicals (South Korea) and NMR solvents were received from Euriso-top (France). All the reagents were used as received, and DI water with a resistivity of 18.2 MΩcm was prepared with Milli-Q system (Millipore).

One pot Thiol-ene Functionalization of PVDF backbone

P(VDF-CTFE) solution with 2.0g of polymer and 60ml of solvent (NMP, TEP,

and DMSO) were added to a round-bottom flask equipped with a magnetic stirring bar. Solution was degassed for more than 30 min and transferred to pre-heated reactor. Designated amount of thiols and bases were consecutively added into flask, and the reaction was proceeded at 60 °C for 24 h under a nitrogen atmosphere unless noted (2.6mM is set as 1equiv. which is equal to the number of CTFE unit in 2.0 g of polymer). The resulting products were precipitated into excess amount of DI water (or brine in case of 3-mercapto-1-propanesulfonate) and washed with DI water and ethanol several times. Finally, the product was dried under vacuum at 50 °C. Side-by-side reactions with PVDF (Solef 1015) and PVDF-TrFE (Solvene 200/200) were subjected to thiol functionalization reaction. 2.0g of polymer, 60ml of NMP and 3.9mM of TEA / mercapto-1-propanol were reacted at 60 °C for 72 h

Bond dissociation enthalpy calculation

Density functional theory (DFT) analysis was utilized to investigate electronic state of molecules and bond dissociation energy of interest. Long-range corrected hybrid functional (CAM-B3LYP) and augmented basis sets precisely descripting electrons and polarity (aug-cc-PVTZ) basis sets were adopted solve Kohn-Sham equation of the molecular system via Gaussian 09 software. Ten different molecular structures existing in fluoropolymers were prepared and experienced

geometry optimization process, carefully finding ground-state of the molecule. After that, the molecule was separated into the two fragments by dissociating C-X (X=F or Cl) bond, and the enthalpies of each fragment were computed. The temperature was set to 298.15 K. The sum of the enthalpies of the two fragment and the original molecule were then compared. The enthalpy difference is equivalent to the bond dissociation enthalpy.

Polymer film fabrication

Polymer solutions were prepared by dissolving polymers into solvent (7-10wt%). Prepared solutions were casted at onto the 80 °C glass plates until the solvent was evaporated. Casted films were peeled off from the glass plates beneath the water bath and dried.

Characterization

The chemical structures of the monomers and polymers were confirmed by NMR spectroscopy (Bruker AVANCE, 500 MHz for ^{1}H, 471 MHz for ^{19}F NMR) using DMSO-d_6 and TMS as a solvent and internal standard. The Fourier transform infrared (FTIR) spectrum were obtained by FT/IR-4100 spectrophotometer (JASCO, Japan) using KBr pellet method. X-ray photoelectron spectroscopy (XPS) was performed using surface analysis system (AXIS NOVA,

KRATOS, UK). Thermogravimetric analysis (TGA, Q5000, TA Instruments) was used to determine the thermal degradation in the temperature range of room temperature to 600 °C at a heating rate of 10 °C min^{-1} under N_2 atmosphere. Differential scanning calorimetry (DSC, Q1000, TA Instruments) was conducted in the temperature range of -50 to 200 °C at a heating rate of 10 °C·min^{-1}. The molar mass and polydispersity index were measured using gel permeation chromatography (GPC with Shodex column) equipped with a refractive index detector. DMF and monodisperse polystyrene were used as the eluent and standard. The water contact angles of films were measured at room temperature and ambient relative humidity using a DSA100 with ADVANCE software (Krüss). Measurements were performed by dispensing 4μl of water onto the film and the results were obtained. The mechanical properties of films were analyzed by universal testing machine (UTM, MultiTest 2.5-I, Mecmesin) at a tensile speed of 50 mm min^{-1}. The samples were cut into dumbbell shapes with testing width of 5 mm. At least four different samples were tested and averaged.

5.3. Results and discussion

To introduce functionality into PVDF backbone, P(VDF-CTFE) was one-pot reacted with thiol and TEA in polar aprotic solvent through multiple reaction pathways. In this system, base induced backbone dehydrochlorination and successive thiol addition were firstly considered. (Figure 5.1a) As reported in the literature, internal double bonds are formed in the P(VDF-CTFE) backbone via a TEA catalyzed dehydrochlorination reaction.[11,21] Due to the influence of electronegative flourine, resulting –CH=CF– double bond has electron-deficient nature and could be subjected to the subsequent thiol-Michael addition reaction. TEA also catalyzes this further process through deprotonation of thiols and the resulting thiolates are introduced into the PVDF backbone. In this reaction, unlike typical thiol-ene reaction solely affording anti-Markovnikov adduct,[34,35] both anti-Markovnikov and Markovnikov addition species were simultaneously observed. These can be attributable to the small van der Waals radius of F atom which offers minimal steric hindrance, and detailed reaction routes are displayed in Figure 5.2.

The molar ratio of CTFE in the pristine P(VDF-CTFE) is 9 mol%, and the sum of formed double bonds and incorporated thiols therefrom is less than 9 mol% considering the -CF_2-CFCl-CF_2- sequence.[36] Hence, the thiol addition

mechanism alone cannot account for more than 9 mol% conversion. However, as will be shown later, conversions exceeding 9 mol% were experimentally observed, and the nucleophile substitution mechanism was additionally considered. (Figure 5.1b) Because thiolate ions have strong basicity, nucleophilic addition to halogens can occur that enables total conversion of more than 9 mol%. Nucleophilic attack on pendant chlorine atoms of CTFE species has been prior reported[28] and this pathway may allow thiolation of the $-CF_2-CFCl-CF_2-$ sequence, which is not possible with the first pathway. Simultaneously, a nucleophilic attack to C-F bond was considered to account for conversions in excess of 9 mol%. In general, breaking C-F bonds with nucleophiles is difficult, but nucleophilic attack has been reported onto unsaturation adjacent fluorine atom under similar conditions.[29,33] Furthermore, it is known that the activity of the remaining C-F bonds increases when one fluorine in the $-CF_2-$ bond is substituted with less electronegative group compared to the robust $-CF_2-$ bond.[22,37] Enhanced reactivity may allow the reaction of primary C-F bond, and the -CFH- and -CF(S-)- species resulting from the pre-described reactions can be possible site. To verify, instead of P(VDF-CTFE), comparative reactions with PVDF and PVDF-TrFE were performed side-by-side. (Figure 5.3) In the same condition, addition of thiol was not observed in PVDF, but the evidence of thiol incorporation was observed in PVDF-TrFE through NMR analysis. The result implies that the -CFH- group can participate in

the nucleophilic substitution unlike -CF_2- group, which corroborate our proposed reaction mechanism. To verify further, ^{19}F-NMR method were utilized to detect the generation of fluoride ion (F^-) which can be originated from the C-F bond cleavage.(Figure 5.3) The reactions involving P(VDF-CTFE) and PVDF were carried out in DMSO-d solvent, and the crude products and the precipitated polymers were respectively investigated. In the P(VDF-CTFE) reaction, a fluoride peak near -165ppm is observed in the crude product, but not observed in the polymer product. From this result, it can be confirmed that the C-F bond participates in the reaction, and the fluoride ion is removed through the polymer purification process. Conversely, emerging peaks were not observed in the experiment using PVDF, which demonstrate the inactivity of the -CF_2- group. To elucidate the reaction pathway, the bond dissociation enthalpies of C-X (X=F or Cl) bond analogues in fluoropolymers were calculated with the aid of quantum chemistry. (Figure 5.4) As expected, -CF_2- showed very strong bond strengths of 471.949 and 481.462 kJ/mol. The C-F bonds in -CF(S-)- species showed dissociation energy of 395.18 and 407.583 kJ/mol, which was lower than -CFH- species in PVDF-TrFE (427.492 and 447.955 kJ/mol). Hence, the calculated bond energies suggest that the C–F bond in the thiol-modified polymer is readily activated via nucleophilic substitution and correlates well with the proposed reaction pathway. (Figure 5.5) Through the pre-described thiol modification

pathway, this reaction would allow the successful incorporation of various functional groups (alkyl, hydroxyl, carboxyl, etc.). To adjust the contents of adduct, input amount of reagent, reaction time, and the type of solvent and other conditions were controlled, and the resulting 61 entries are listed in Table 5.1.

To investigate the reaction, the model reaction was conducted with mercapto-1-propanol which bear thiol and hydroxyl group at both end. NMP was selected as solvent since dehydrochlorination is most likely to occur in NMP among the solvent used (Table 5.1, entry 1-3).[21] Figure 5.6a displays the ^{1}H NMR spectrum of pristine P(VDF-CTFE), double bond incorporated, and the thiol functionalized polymers. In the spectra of P(VDF-CTFE), only VDF unit related peaks were observed at 2.7−3.5 (H-T sequence) and 2.3−2.5 ppm (T-T sequence). In addition to VDF peaks, multiple peaks are observed on the spectrum of hydroxyl functionalized polymers.[25] Newly appeared peaks can be designated to hydroxyl and methylene group of thiol and internal double bond. The molar ratios of the incorporated thiol and internal double bond were compared from the peaks of VDF, internal double bond, and peak c (thiol, β position CH_2). Further, molar contents of hydroxyl thiol ([*OH*]) and double bond ([*DB*]) were quantified from Equation 1 and 2, considering the molar content of the P(VDF-CTFE).

(1) $$[DB] = \frac{I[-CH=CF-]}{I[-CH=CF-] + I[c] + I[VDF]} \times 91\ mol\%$$

(2) $$[OH] = \frac{I[c]}{I[-CH=CF-] + I[c] + I[VDF]} \times 91\ mol\%$$

^{19}F NMR spectrum of the same polymers were exhibited on the Figure 5.6b. Compared to original P(VDF-CTFE), in the spectrum of dehydrochlorinated polymer, double bond-related peaks are generated, and the intensity of the chlorine-adjacent peaks is reduced. Double bond-related peaks are totally or partially vanished in thiol modified P(VDF-CTFE) due to the consumption of the double bond in thiol addition process. Moreover, the almost complete disappearance of the chlorine-related peaks indicates the occurrence of nucleophilic substitution between thiolates and halogens. Further characterizations except for NMR spectroscopy are discussed below.

In order to determine the influence of thiol / base dosage, reaction conditions were systemically investigated. Reactions were proceeded in NMP for 24h at 60 °C and the amounts of thiol and base (TEA) were simultaneously adjusted from 0 to 4.0 equiv. Molar ratios of introduced thiol and double bond were calculated from ^{1}H NMR and results are shown in Figure 5.7a. As the reagent input increases, the content of double bonds increases and then slightly decreases because increasing the reagent concentration initially favors dehydrochlorination, but it rather promote thiolate addition afterward. The amount of thiol increases in proportion to the addition of the reagent, and eventually has a composition of

[OH]=8.3, [DB]=2.9 mol% under the condition of thiol (equiv.) / base (equiv.) = 4.0 / 4.0. The exceptionally high conversion is the combinational result of thiol-Michael addition into double bond and nucleophilic substitution reaction as previously described. Resulting polymers synthesized from the conditions of thiol (equiv.) / base (equiv.) = 0.5 / 0.5, 1.5 / 1.5, and 3.0 / 3.0 were further characterized by FTIR, XPS, TGA, and GPC analyses. FTIR spectrum in Figure 5.7b reveal that new noticeable signals appear around 3500cm^{-1} and 1700 cm^{-1} which correspond to characteristic peak of hydroxyl group and double bond in PVDF backbone.[1,15,32] These results indicated the introduction of hydroxyl thiol into PVDF backbone and further corroborated by XPS survey spectrum (Figure 5.7c). As more amounts of thiol and TEA were added to the reaction, the Cl_{2p} peaks from P(VDF-CTFE) backbone disappeared, and the thiol-originated O_{1s}, S_{2s}, and S_{2p} peak intensities gradually increased. These results indicated the successful thiol addition reaction into PVDF backbone in line with the pre-discussed NMR data. Thermal properties of polymers were also measured by thermogravimetric analysis and differential scanning calorimetry. TGA curves in Figure 5.7d represent that pristine P(VDF-CTFE) was stable up to 400 °C, whereas thiol modified polymers have thermal decomposition around 250°C owing to fragile thiol linkage.[38] Therefore, as the contents of incorporation thiol increased, more decomposition was observed between 250 and 400 °C. However,

the residual weight of synthesized polymers above 500 °C was even larger than that of P(VDF-CTFE), attributable to double bond related thermal crosslinking.[21] Also, crystallization enthalpy ($D\Delta H_c$) and crystallization temperature decreases, as the increase of thiol introduction, ascribed to the plastisizing effect of hydroxyl branch (Figure 5.8). The number average molar masses (M_n) and polydispersity index (PDI) were investigated by GPC (Figure 5.7e). Except for one sample synthesized under the condition of thiol (equiv.) / base (equiv.) = 3.0 / 3.0, all polymers show almost similar elution behavior on the GPC curves. The three polymers exhibit almost identical curvature, and their peaks appears at a retention time of about 10 min, indicating similar M_n and PDI values ranged in 180,000 - 187,000 and 1.6 - 1.7, respectively. However, in the curve of the sample having 5.9 mol% of hydroxyl group and 3.1 mol% of double bond, shifted peak position and the extended curvature are observed. This result demonstrates that M_n and PDI increased at the same time (209,000 and 2.2 respectively), which can be explicable to a crosslinking reaction from an excess of reagent.[29,31] Therefore, in this system, using a large amount of reagent may deteriorate the solvent solubility caused by crosslinking albeit can obviously increase the degree of functionalization.

Experiments were conducted to determine the influence of the ratio of thiol / base input and their results are shown on Figure 5.9. The dose of TEA was fixed

of 1.0 equiv., and the amount of thiol was controlled from 0 to 4 equiv. Firstly, 1 equiv. of TEA was solely participated in the reaction, and resulting molar content of the generated double bond was 3.2 mol%. The content of the double bond hardly changed even with the addition of thiol, but it slightly decreased to 2.3 mol% when 4 equiv. of thiol was introduced. In contrast, the molar contents of the inserted thiol increase with the increasing amount of dosing thiol. However, rather decreased thiol conversion is also observed in case of 4 equiv. of thiol input. In this case, the highest conversion rate was observed under the condition of thiol (equiv.) / base (equiv.) = 3.0 / 1.0, implying the presence of optimal thiol / base ratio. The utilization of excess thiol rather can reduce the thiol addition since TEA can be involved in multiple reactions that could be competitive, including dehydrochlorination and thiol deprotonation.[39]

Figure 5.10 displays the time-dependency profile of incorporated hydroxyl thiol and generated double bond contents. To avoid crosslinking that might occur in prolonged reactions, the amounts of thiol and base (TEA) dosage were set as thiol (equiv.) / base (equiv.) = 1.5 / 1.5 and the reaction was proceeded in NMP at 60 °C. The reaction was carried out for 48h, and samples were obtained at predetermined points to conduct ^{1}H NMR analysis. The reaction rate is fast in the beginning, but it gradually decreases as the reaction progresses. Nearly 50% of the thiol addition and double bond formation reaction occurs in the first 4 hours, which

continuously increases to a composition of [OH]=3.2, [DB]=3.9 mol% after 48 hours. Interestingly, except for the case of 1h, the content of double bond were slightly dominant than inserted thiol, and their ratio had been maintained over time.

To investigate the effect of solvent, two other polar aprotic solvents (TEP and DMSO) were used instead of NMP, which is known to well dissolve PVDF and also known to be environmentally friendly (Figure 5.11a).[40,41] After 24 hours of reaction, polymers with dramatically different compositions were obtained, although they are all polar aprotic solvents. Compared to NMP, the polymer obtained from TEP showed much smaller thiol addition, and the polymer obtained from DMSO rather showed the opposite (Figure 5.11b). These results can be ascribed to polarity of the solvents (DMSO > NMP >TEP), and it has been observed that the polarity has a positive influence on the conversion efficiency. Solvents with higher polarity can promote the reaction in two reason : 1) they can better accommodate the byproduct of double bond formation (HCl),[21] 2) they can better stabilize the thiolate ion, thus facilitating its generation.[42] Therefore, the polymer from TEP show the composition of [OH] = 2.2 and [DB] = 2.7 mol% even after 72 hours, but in the case of DMSO, insoluble polymer was observed due to crosslinking (Table 5.1, entry 33, 35). Figure 5.11c exhibits the time-dependency profile of the reaction executed in DMSO solvent. Compared to NMP

(Figure 5.9), totally different propensity was observed including much faster early reaction rate, and unvarying double bond content after 9h (~2.9 mol%), despite the continuously increasing thiol content. The composition of the final product is [OH]=7.9, [DB]=3.0 mol%, confirming superior addition efficiency in DMSO solvent system.

Two additional nitrogen containing bases of MI (pK_a =7.0) and DABCO (pK_a =8.8) were also utilized in the reactions (Figure 5.12a).[35,43] Primary amines known to be suitable for Michael addition[34,44] have also been used (n-butylamine, pK_a =10.2), but they produced insoluble products on account of side reactions like crosslinking (Table 5.1, entry 46).[29,45] Bases with higher pK_a were not intentionally selected since they could be involved in the backbone dehydrofluorination and undermine the selectivity of the reaction.[1,2] As revealed in Figure 5.12b, the usage of other two bases debilitates the efficiency of thiol introduction or double bond formation compared to the use of TEA (pK_a =10.8). The same tendency is also shown in the DMSO solvent (Table 5.1, entry 44, 45), because the weaker the basicity, the less favorable the double bond formation which make acidic byproduct. A drastic low conversion was observed for MI, which is known to good agent for nucleophile-catalyzed thiol-Michael addition.[43] For the current one-pot reaction, therefore, reaction catalysts that proceed primarily through the base-catalyzed pathway are more suitable than

those using the nucleophile catalytic pathway. Furthermore, experiments on reaction temperature and sensitivity to oxygen and water were also conducted (Table 5.1, entry 28-31). High temperature leads to only small increase of incorporated thiol that can be attributable to facilitation of the internal double bond formation.[21] According to experiments conducted in the air or in the presence of water, the reaction demonstrates the water- and oxygen-tolerant characteristic widening their feasibility to practical applications.[45]

To verify the versatility of modification reaction, varied functionalities were introduced into P(VDF-CTFE) backbone. Six different thiols possessing hexyl (C_6), (trifluoromethyl)aryl ($ArCF_3$), sulfonate (SO_3), carboxyl (COOH), dimethylamino ($N(CH_3)_2$), and perfluorinated ($C_{10}F_{17}$) groups were selected and reacted with P(VDF-CTFE) (Figure 5.13). The reactions were successfully conducted following the similar conditions as hydroxyl thiol. To calculate the molar contents of the introduced functional groups and double bonds, ^{1}H NMR spectrum, ^{19}F NMR and XPS elemental analysis were solely or complementary utilized and their spectrum were exhibited in Figures 5.14. Regardless of the type of thiol, usage of DMSO solvent shows advantageous effect on thiol conversion than NMP solvent and this result is consistent with the solvent effect experiments. Although there is a difference in conversion rate, it is confirmed that various functional groups were well inserted into the PVDF main chain and it may be

further controlled through the adjustment of reaction conditions. Consequently, current reaction route can be adopted in numerous thiols and fine-tuned polymers can be facilely produced from the thiol modification.

To study the potentials in practical application, thiol-modified PVDF copolymers were fabricated into films by solvent casting method and their properties were analyzed. Firstly, to assess the wettability of the polymers, the water contact angles were measured and displayed in Figure 5.15. Owing to its fluorine-rich structure, pristine P(VDF-CTFE) film shows the high water contact angle of 83.3° which can be considered hydrophobic. Water contact angle decreased slightly by the introduction of unsaturation into PVDF backbone, but not significant. As the various functional group were incorporated into the fluorinated backbone, arbitrarily tuned wettability was observed. Due to the hydrophilic nature, hydroxyl, amino and sulfonate groups make the polymer more hydrophilic and accordingly lower the contact angles to ~70°. Modification with hydrophobic functional thiols rather make the water contact angle higher than the original polymer, and particularly, highly hydrophobic film was observed when perfluorinated group was included. Therefore, modifying P(VDF-CTFE) with current thiol addition pathway, possibly regulate the surface wettability by employing appropriate thiols. The mechanical properties of films were also investigated and typical tensile stress-strain curves are displayed in Figure 5.16a. The similar tensile behaviors

which include yielding, strain hardening, and necking were observed from all the samples. From each curve, tensile strength (σ) and elongation at break (ε break) data were obtained and reported in Figure 5.16b. The pristine P(VDF-CTFE) film shows a tensile strength (σ) of ~11 MPa and elongation at break (ε break) of ~450%. However, markedly improved tensile properties were observed from thiol-modified films except for alkyl (C_6) and perfluoroalkyl ($C_{10}F_{17}$) modified samples. Both strength and elastic properties were simultaneously improved to a different level that can be attributable to the interaction between the PVDF backbone and introduced functionality.[7,46,47] Among the films, hydroxyl-modified PVDF exhibits the best mechanical properties of σ and ε break of ~23 MPa and ~830%, respectively, showing about twice the performance of the original polymer. In addition, elastic modulus of the samples were calculated from the beginning of the curve and displayed on Figure 5.17. Although there are some exceptions, highly enhanced modulus were observed in most samples and the tendency is very similar with the tensile strength or elongation property of the films. Since high modulus is desirable property which related to the breakdown strength of the polymer dielectric,[48,49] thiol-modified polymers also possess great potential to be utilized as dielectric polymer with enhanced property.

5.4. Conclusion

Commercially available fluoropolymer P(VDF-CTFE) is successfully modified with thiols having varied functional groups (hydroxyl, alkyl, aryl, sulfonate, carboxyl, amino and perfluorinated group) via tertiary amine catalyzed one-step mild reaction. The reaction has been resolute to be in the three different reactions of double bond formation, thiol-Michael addition into double bond, and nucleophilic substitution to halogen. To adjust the thiol introduction into resultant fluoropolymers, reaction conditions were accordingly controlled. The pKa value of the base and solvent polarity, as well as the reagent dose and time, had a significant influence on the thiol incorporation, and in several cases, conversion rates exceeding 100% were observed that are attributable to nucleophilic substitution to C-F bond. The C-F bond sites for substitution are proposed with the aid of quantum chemistry and comparison reaction with PVDF or PVDF-TrFE. Nine different fluoropolymers with or without functionalities were fabricated into polymer films by solvent casting method. They exhibited controlled surface hydrophilicity and noticeably altered mechanical properties. Owing to simplicity and universality, we believe that this reaction system can contribute to fluoropolymer field by lowering the barrier to on-demand fluoropolymer synthesis.

5.5. References

[1] J. Sierke, A. V. Ellis, *J. Membr. Sci.,* 2019, 581, 362–372.

[2] C. Van Goethem, M.M. Magboo, M. Mertens, M. Thijs, G. Koeckelberghs, I.F.J. Vankelecom, *J. Membr. Sci.,* 611, 118274.

[3] K.A. Wood, *Prog. Org. Coatings,* 2014, 77, 2140–2146.

[4] M. Wehbi, S. Banerjee, A. Mehdi, A. Alaaeddine, A. Hachem, B. Ameduri, *Macromolecules,* 2017, 50, 9329–9339.

[5] A.R. Motz, M.C. Kuo, J.L. Horan, R. Yadav, S. Seifert, T.P. Pandey, S. Galioto, Y. Yang, N. V. Dale, S.J. Hamrock, A.M. Herring, *Energy Environ. Sci.,* 2018, 11, 1499–1509.

[6] K. Feng, B. Tang, P. Wu, *J. Mater. Chem. A,* 2015, 3, 12609–12615.

[7] J.I. Lee, H. Kang, K.H. Park, M. Shin, D. Hong, H.J. Cho, N.R. Kang, J. Lee, S.M. Lee, J.Y. Kim, C.K. Kim, H. Park, N.S. Choi, S. Park, C. Yang, *Small,* 2016, 12, 3119–3127.

[8] X. Wang, S. Liu, Y. Zhang, H. Wang, A.A. Aboalhassan, G. Li, G. Xu, C. Xue, J. Yu, J. Yan, B. Ding, *ACS Appl. Mater. Interfaces,* 2020, 12, 38132–38139.

[9] Y. Huang, J.Z. Xu, T. Soulestin, F.D. Dos Santos, R. Li, M. Fukuto, J. Lei, G.J. Zhong, Z.M. Li, Y. Li, L. Zhu, *Macromolecules,* 2018, 51, 5460–5472.

[10] J. Lin, M.H. Malakooti, H.A. Sodano, *ACS Appl. Mater. Interfaces,* 2020, 12,

21871–21882.

[11] Z. Zhang, X. Wang, S. Tan, Q. Wang, *J. Mater. Chem. A,* 2019, 7, 5201–5208.

[12] V.I. Sultanov, V. V. Atrazhev, D. V. Dmitriev, N.S. Erikhman, D.U. Furrer, S.F. Burlatsky, *Macromolecules,* 2021, 54, 3744–3754.

[13] T. Soulestin, V. Ladmiral, F.D. Dos Santos, B. Améduri, *Prog. Polym. Sci.,* 2017, 72, 16–60.

[14] B. Ameduri, *Chem. Rev.,* 2009, 109, 6632–6686.

[15] D.J. Han, S. Kim, H.J. Heo, I.J. Park, H.S. Kang, S.G. Lee, J.-C. Lee, E.-H. Sohn, *ACS Appl. Polym. Mater.,* 2020, 2, 3957–3965.

[16] S. Banerjee, T. Soulestin, Y. Patil, V. Ladmiral, B. Ameduri, *Polym. Chem.,* 2016, 7, 4004–4015.

[17] H.J. Heo, I.J. Park, S.G. Lee, J.W. Ha, S.B. Lee, E.H. Sohn, *Green Chem.,* 2018, 20, 502–505.

[18] M.N. Wadekar, Y.R. Patil, B. Ameduri, *Macromolecules,* 2014, 47, 13–25.

[19] F. Reis Da Cunha, I. Davidovich, Y. Talmon, B. Ameduri, *Polym. Chem.,* 2020, 11, 2430–2440.

[20] Y. Patil, B. Ameduri, *Prog. Polym. Sci.,* 2013, 38, 703–739.

[21] S. Tan, J. Li, G. Gao, H. Li, Z. Zhang, *J. Mater. Chem.,* 2012, 22, 18496–18504.

[22] B. Peng, J. Wang, M. Li, M. Wang, S. Tan, Z. Zhang, *Polym. Chem.,* 2021, 12,

3132–3141.

[23] J.F. Hester, P. Banerjee, Y.Y. Won, A. Akthakul, M.H. Acar, A.M. Mayes, *Macromolecules,* 2002, 35, 7652–7661.

[24] D.J. Han, S. Kim, H.J. Heo, C. Jin, J. Kim, H. Choi, I. J. Park, H. S. Kang, S. G. Lee, J.-C. Lee, E.-H. Sohn, *Appl. Surf. Sci.,* 2021, 562, 150181.

[25] D.J. Han, H.J. Heo, I.J. Park, H.S. Kang, S.G. Lee, S.-B. Lee, J.-C. Lee, E.-H. Sohn, *ACS Appl. Polym. Mater.,* 2020, 2, 178–188.

[26] J. Dai, Y. Dong, C. Yu, Y. Liu, X. Teng, *J. Membr. Sci.,* 2018, 554, 324–330.

[27] A. Taguet, L. Sauguet, B. Ameduri, B. Boutevin, *J. Fluor. Chem.,* 2007, 128, 619–630.

[28] M.W. Pelter, R.T. Taylor, *J. Polym. Sci. Part A Polym. Chem.,* 1988, 26, 2651–2667.

[29] A. Taguet, B. Ameduri, B. Boutevin, *Adv. Polym. Sci.,* 2005, 184, 127–211.

[30] D. Zou, Y. M. Lee, *Prog. Polym. Sci.,* 2022, *128*, 101535

[31] K.L. Paciorek, L.C. Mitchell, C.T. Lenk, *J. Polym. Sci.,* 1960, 45, 405–413.

[32] L. Xiao, D.M. Davenport, L. Ormsbee, D. Bhattacharyya, *Ind. Eng. Chem. Res.,* 2015, 54, 4174–4182.

[33] S. Tan, D. Li, Y. Zhang, Z. Niu, Z. Zhang, *Macromol. Chem. Phys.,* 2018, 219, 1–8.

[34] J.W. Chan, C.E. Hoyle, A.B. Lowe, M. Bowman, *Macromolecules,* 2010, 43,

6381–6388.

[35] A.B. Lowe, *Polym. Chem.,* 2014, 5, 4820–4870.

[36] Y. Lu, J. Claude, Q. Zhang, Q. Wang, *Macromolecules,* 2006, 39, 6962–6968.

[37] Y. Wang, A. Liu, *Chem. Soc. Rev.,* 2020, 49, 4906–4925.

[38] C.E. Hoyle, T.Y. Lee, T. Roper, *J. Polym. Sci. Part A Polym. Chem.,* 2004, 42, 5301–5338.

[39] X. Hu, S. Tan, G. Gao, Y. Xie, Q. Wang, N. Li, Z. Zhang, *J. Polym. Sci. Part A Polym. Chem.,* 2014, 52, 3429–3440.

[40] J. Chang, J. Zuo, L. Zhang, G.S. O'Brien, T.S. Chung, *J. Membr. Sci.,* 2017, 539, 295–304.

[41] A. Figoli, T. Marino, S. Simone, E. Di Nicolò, X.M. Li, T. He, S. Tornaghi, E. Drioli, *Green Chem*., 2014, 16, 4034–4059.

[42] G.Z. Li, R.K. Randev, A.H. Soeriyadi, G. Rees, C. Boyer, Z. Tong, T.P. Davis, C.R. Becer, D.M. Haddleton, *Polym. Chem.,* 2010, 1, 1196–1204.

[43] W. Xi, C. Wang, C.J. Kloxin, C.N. Bowman, *ACS Macro Lett.,* 2012, 1, 811–814.

[44] K.F. Long, H. Wang, T.T. Dimos, C.N. Bowman, *Macromolecules*, 2021, 54, 3093–3100.

[45] G.B. Desmet, M.K. Sabbe, D.R. D'Hooge, P. Espeel, S. Celasun, G.B. Marin, F.E. Du Prez, M.F. Reyniers, *Polym. Chem.,* 2017, 8, 1341–1352.

[46] C. Xing, M. Zhao, L. Zhao, J. You, X. Cao, Y. Li, *Polym. Chem.,* 2013, 4, 5726–5734.

[47] S. Samanta, D.P. Chatterjee, S. Manna, A. Mandal, A. Garai, A.K. Nandi, *Macromolecules*, 2009, 42, 3112–3120.

[48] Z.X. Huang, M.M. Wang, Y.H. Feng, J.P. Qu, Macromolecules, 2020, 53, 8494–8501.

[49] J. Claude, Y. Lu, K. Li, Q. Wang, *Chem. Mater.,* 2008, 20, 2078–2080.

Table 5.1. Reaction conditions and compositions of resulting polymers

En-try	P(VDF-CTFE)(g)	Thiol/ input (equiv.)	base/input (equiv.)	solvent/ input(mL)	Tempera-ture(°C)	Time	[SH] (mol%)	[DB] (mol%)
1	2	-	TEA/1.5	NMP/60	60	24h	0	4.1
2	2	-	TEA/1.5	TEP/60	60	24h	0	1.4
3	2	-	TEA/1.5	DMSO/60	60	24h	0	3.4
4	2	-	TEA/1.5	NMP/60	60	72h	0	4.9
5	2	-	TEA/2.5	NMP/60	60	72h	0	7.1
6	2	-	MI/1.5	NMP/60	60	24h	0	0.8
7	2	-	DABCO/0.75	NMP/60	60	24h	0	3.1
8	2	-OH/1.5	-	NMP/60	60	24h	0.0	0.0
9	2	-OH/0.5	TEA/0.5	NMP/60	60	24h	1.1	2.5
10	2	-OH/1.0	TEA/1.0	NMP/60	60	24h	2.4	3.6
11	2	-OH/1.5	TEA/1.5	NMP/60	60	24h	3.2	3.9
12	2	-OH/2.0	TEA/2.0	NMP/60	60	24h	4.2	3.6
13	2	-OH/3.0	TEA/3.0	NMP/60	60	24h	5.9	3.1
14	2	-OH/4.0	TEA/4.0	NMP/60	60	24h	8.3	2.9
15	2	-	TEA/1.0	NMP/60	60	24h	0.0	3.2
16	2	-OH/0.5	TEA/1.0	NMP/60	60	24h	1.3	3.4
17	2	-OH/1.0	TEA/1.0	NMP/60	60	24h	2.4	3.6
18	2	-OH/1.5	TEA/1.0	NMP/60	60	24h	2.9	3.2
19	2	-OH/2.0	TEA/1.0	NMP/60	60	24h	3.8	3.3
20	2	-OH/3.0	TEA/1.0	NMP/60	60	24h	4.4	3.1
21	2	-OH/4.0	TEA/1.0	NMP/60	60	24h	3.6	2.3
22	2	-OH/1.5	TEA/1.5	NMP/60	60	1h	0.7	0.6
23	2	-OH/1.5	TEA/1.5	NMP/60	60	2h	1.0	1.1
24	2	-OH/1.5	TEA/1.5	NMP/60	60	4h	1.6	1.9
25	2	-OH/1.5	TEA/1.5	NMP/60	60	6h	2.1	2.2
26	2	-OH/1.5	TEA/1.5	NMP/60	60	9h	2.5	2.7
27	2	-OH/1.5	TEA/1.5	NMP/60	60	48h	3.9	4.5
28	2	-OH/1.5	TEA/1.5	NMP/60	40	24h	2.4	2.2
29	2	-OH/1.5	TEA/1.5	NMP/60	80	24h	3.7	4.8
30 [a]	2	-OH/1.5	TEA/1.5	NMP/60	60	24h	3.4	3.7
31 [b]	2	-OH/1.5	TEA/1.5	NMP/60	60	24h	3.4	3.6
32	2	-OH/1.5	TEA/1.5	TEP/60	60	24h	1.2	1.6

33	2	-OH/1.5	TEA/1.5	TEP/60	60	72h	2.2	2.7
34	2	-OH/1.5	TEA/1.5	DMSO/60	60	24h	6.0	3.2
35	2	-OH/1.5	TEA/1.5	DMSO/60	60	72h	insoluble	
36	2	-OH/1.5	TEA/1.5	DMSO/60	60	1h	2.4	0.7
37	2	-OH/1.5	TEA/1.5	DMSO/60	60	2h	3.2	1.6
38	2	-OH/1.5	TEA/1.5	DMSO/60	60	4h	3.6	2.0
39	2	-OH/1.5	TEA/1.5	DMSO/60	60	6h	4.4	2.6
40	2	-OH/1.5	TEA/1.5	DMSO/60	60	9h	4.8	2.9
41	2	-OH/1.5	TEA/1.5	DMSO/60	60	48h	7.9	3.0
42	2	-OH/1.5	MI/1.5	NMP/60	60	24h	0.9	0.6
43	2	-OH/1.5	DABCO/0.75	NMP/60	60	24h	2.6	3.4
44	2	-OH/1.5	MI/1.5	DMSO/60	60	24h	1.5	1.6
45	2	-OH/1.5	DABCO/0.75	DMSO/60	60	24h	4.0	3.6
46	2	-OH/1.5	butylamine/1.5	NMP/60	60	24h	insoluble	
47	2	C6/1.5	TEA/1.5	NMP/60	60	24h	3.6	3.9
48	2	C6/3.0	TEA/1.5	NMP/60	60	24h	5.1	3.3
49	2	C6/1.5	TEA/1.5	DMSO/60	60	24h	6.0	3.3
50[c]	2	ArCF3/1.5	TEA/1.5	NMP/60	60	24h	4.3	1.5
51[c]	2	ArCF3/3.0	TEA/1.5	NMP/60	60	24h	6.1	2.8
52[c]	2	ArCF3/1.5	TEA/1.5	DMSO/60	60	24h	5.6	3.1
53	2	SO3/1.5	TEA/1.5	NMP/60	60	24h	1.2	0.3
54	2	SO3/3.0	TEA/1.5	NMP/60	60	24h	1.7	0.2
55	2	SO3/1.5	TEA/1.5	DMSO/60	60	24h	2.9	0.3
56	2	COOH/1.5	TEA/1.5	NMP/60	60	24h	2.8	3.9
57	2	COOH/1.5	TEA/1.5	DMSO/60	60	24h	5.4	2.9
58	2	DMAE/1.5	TEA/1.5	NMP/60	60	24h	0[c]	2.3
59[d]	2	DMAE/1.5	TEA/1.5	DMSO/60	60	24h	4.7[c]	1.3
60[c]	1	C10F17/1.5	TEA/1.5	NMP/60	60	24h	0.3	5.3
61[c]	1	C10F17/1.5	TEA/1.5	DMSO/60	60	24h	3.8	4.9

[a)] Experiment conducted under air

[b)] Experiment conducted with 1mL of water

[c)] Calculated from ^{19}F NMR analysis

[d)] Calculated from XPS analysis

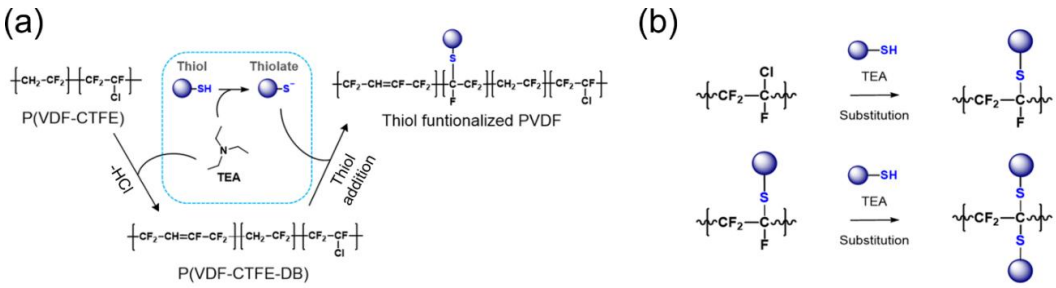

Figure 5.1. Reaction pathway of (a) dehydrochlorination and thiol addition (b) nucleophilic substitution between polymer backbone and TEA catalyzed thiol

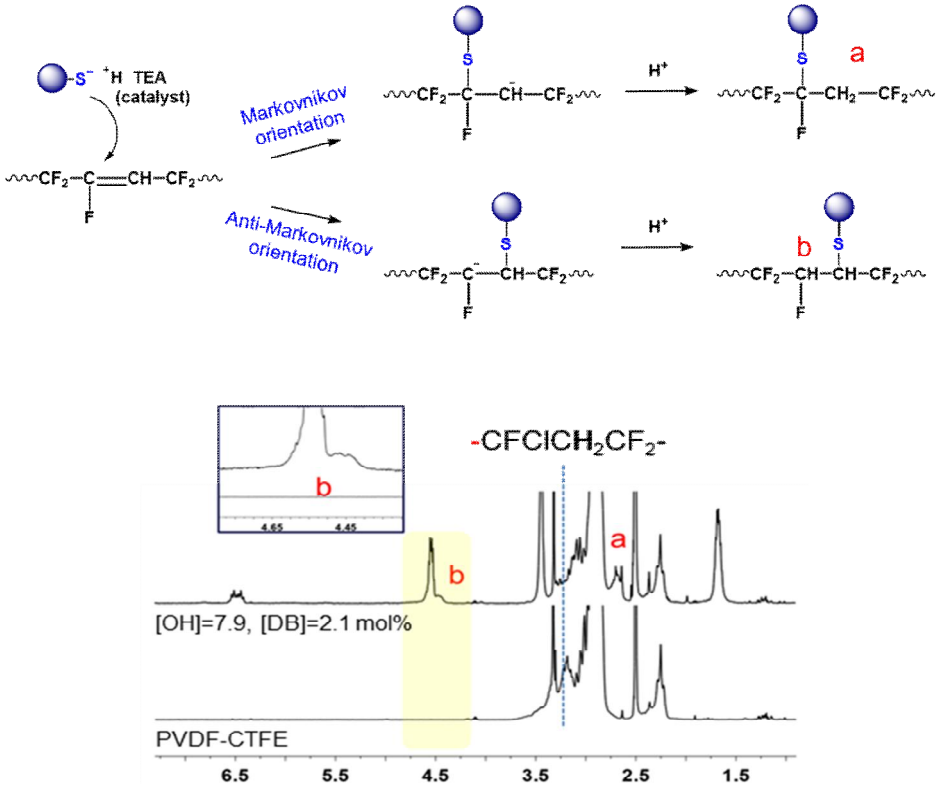

Figure 5.2. Reaction pathway of the thiol insertion in Markovnikov and anti-Markovnikov direction and ^{1}H NMR spectrum of pristine P(VDF-CTFE) and thiol modified P(VDF-CTFE). The insets are amplified signals in the range 4.3-4.7 ppm. (solvent : DMSO –d_6)

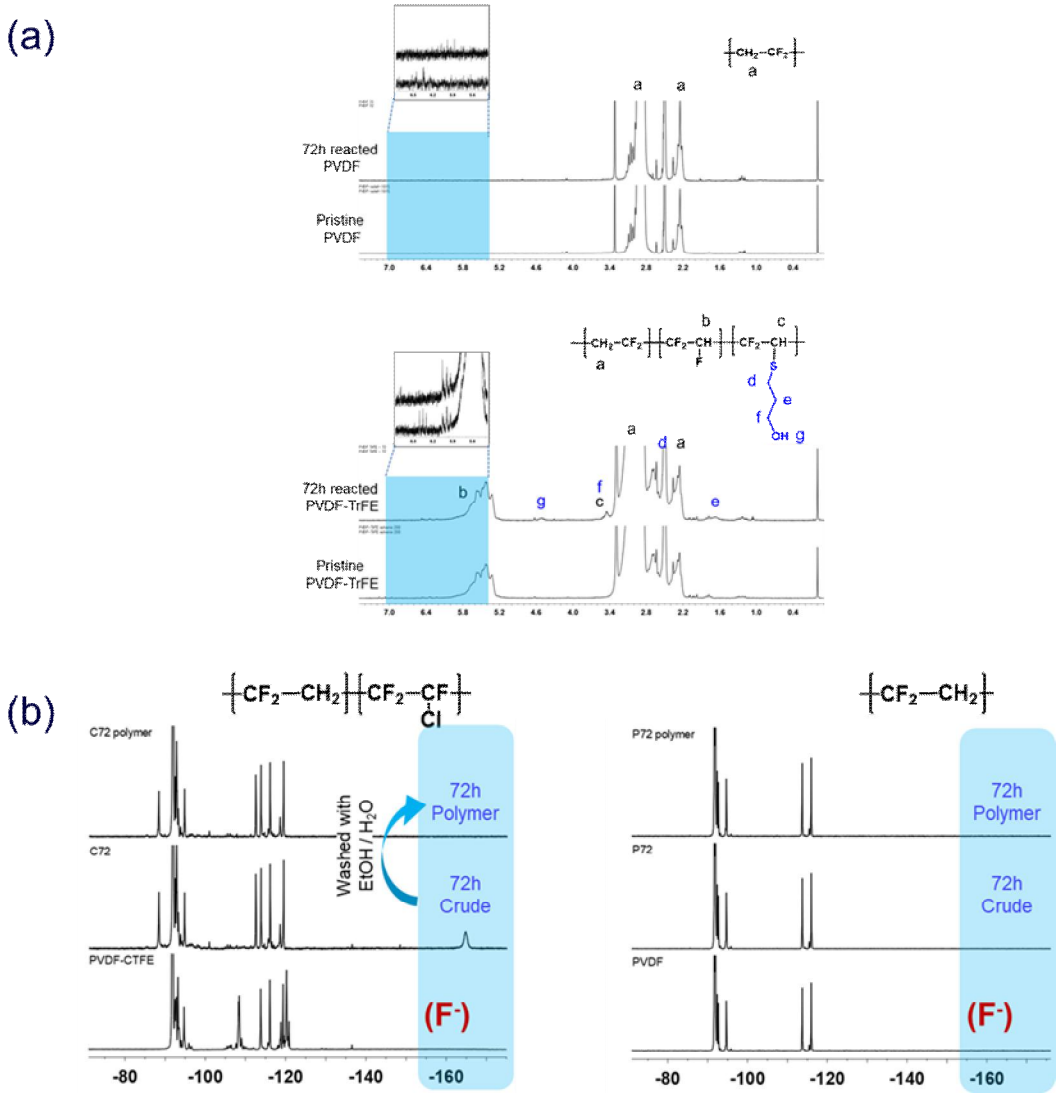

Figure 5.3. (a) ^{1}H NMR spectrum of PVDF and PVDF-TrFE (pristine or 72h reacted). (b) ^{19}F NMR spectrum of P(VDF-CTFE) and PVDF (pristine, 72h reacted crude product, and precipitated polymer).

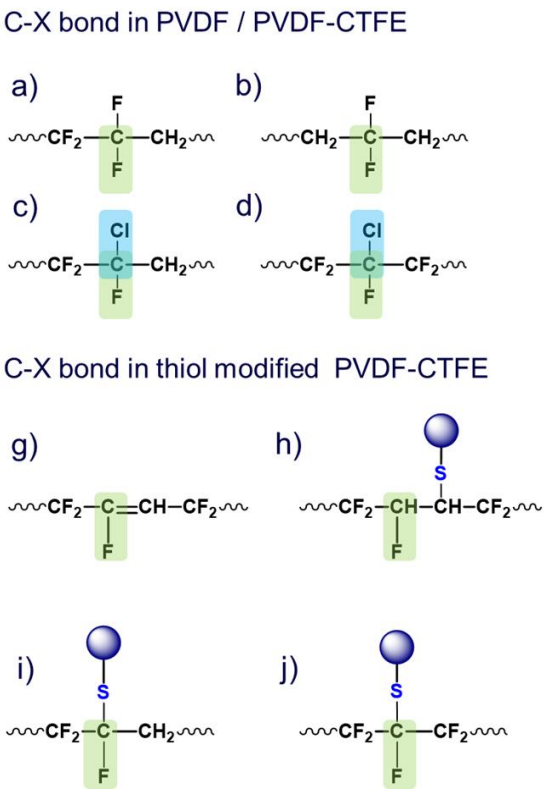

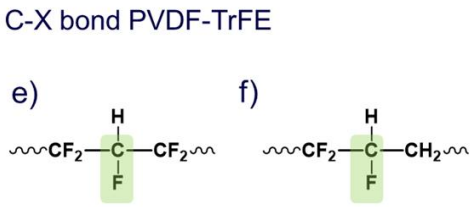

	C-X bond (sequence)	Bond dissociation enthalpy (kJ/mol)
	PVDF / PVDF-CTFE	
a	-CF_2**CF**$_2CH_2$-	-471.949
b	-CH_2**CF**$_2CH_2$-	-481.462
c-1	-CF_2**CF**ClCH_2-	-421.007
c-2	-CF_2**CF**ClCH_2-	-289.005
d-1	-CF_2**CF**ClCF_2-	-420.852
d-2	-CF_2**CF**ClCF_2-	-292.851
	PVDF-TrFE	
e	-CF_2**CF**HCF_2-	-427.492
f	-CF_2**CF**HCH_2-	-447.955
	Thiol modified PVDF-CTFE	
g	-CF_2**CF**=CH-	-484.838
h	-CF_2**CF**HCH(S-C)-	-415.795
i	-CF_2**CF**(S-C)CH_2-	-395.18
j	-CF_2**CF**(S-C)CF_2-	-407.583

Figure 5.4. Structure of C-X (X=F or Cl) bond analogues in fluoropolymers (a-j), and their calculated bond dissociation enthalpy

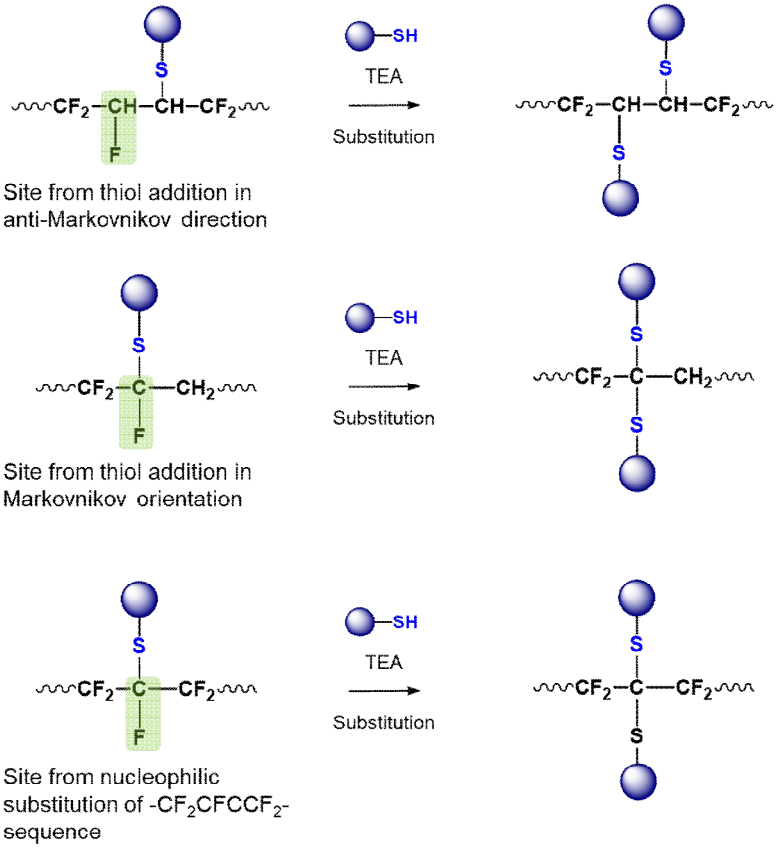

Figure 5.5. Proposed reaction pathway of the nucleophilic substitution between C-F bond and TEA catalyzed thiol

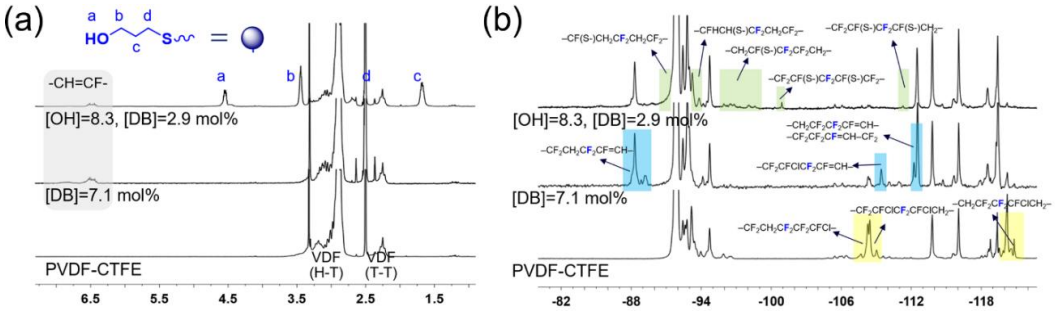

Figure 5.6. (a) ^{1}H NMR and (b) ^{19}F NMR spectrum of P(VDF-CTFE), fully dehydrochlorinated P(VDF-CTFE) ([DB]=7.1mol%), and thiol modified P(VDF-CTFE) ([OH]=8.3, [DB]=7.1mol%)

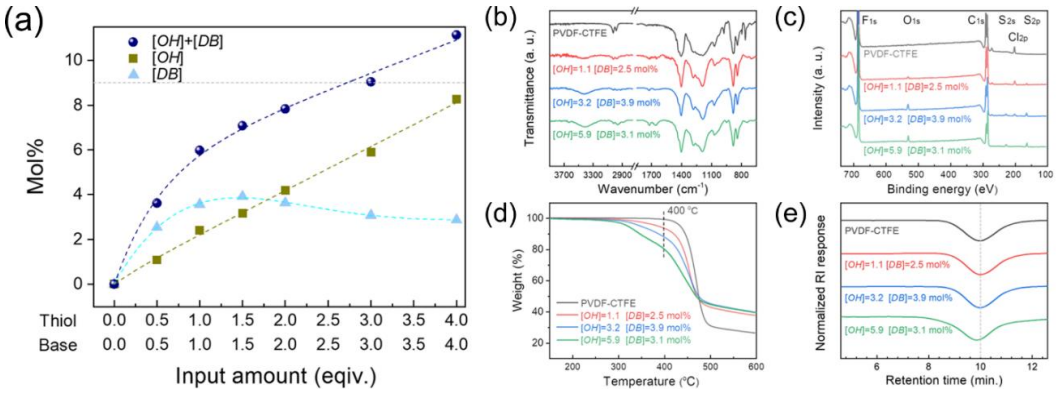

Figure 5.7. (a) Thiol / base input dependency of incorporated thiol and double bond, (b) FTIR (c) XPS (d) TGA (e) GPC results of P(VDF-CTFE) and thiol modified P(VDF-CTFE) with different composition

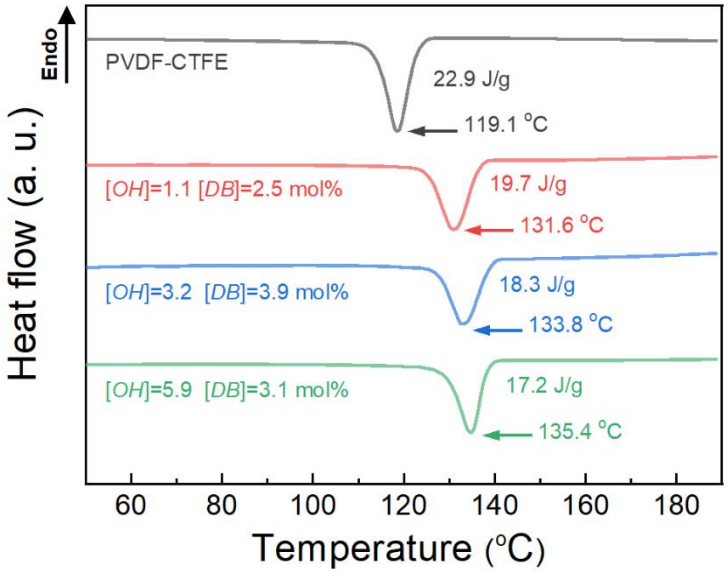

Figure 5.8. DSC curves, enthalpy of crystallization (ΔH_c), and crystallization temperatures of prinstine P(VDF-CTFE) and polymers in Table 5.1 entry 9, 11 and 13 (top to down, respectively)

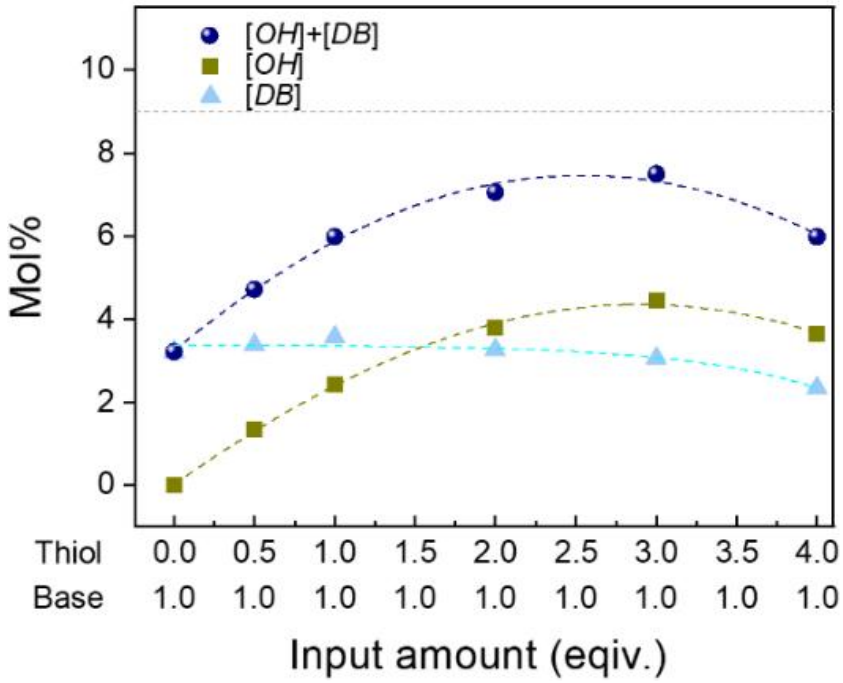

Figure 5.9. Thiol input dependency of incorporated thiol and double bond

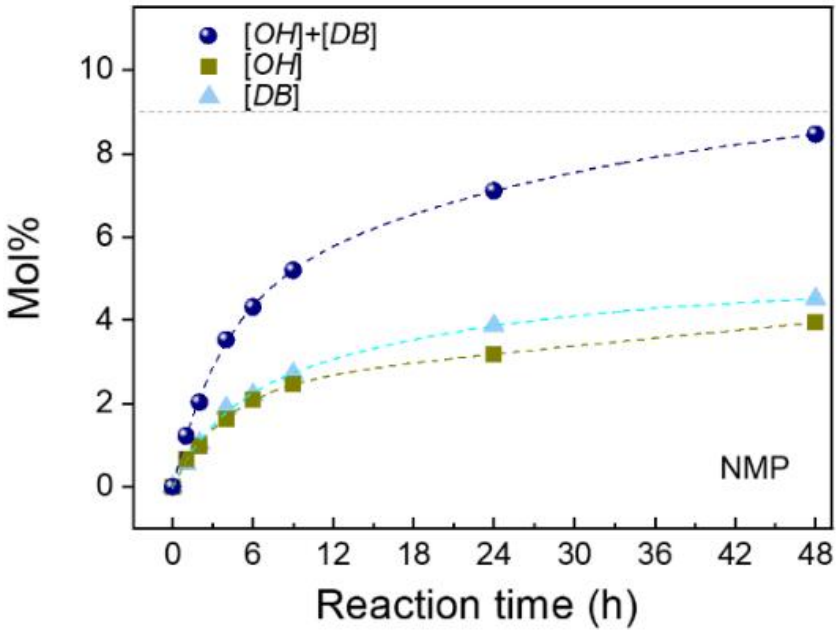

Figure 5.10. Time dependency of incorporated thiol and double bond

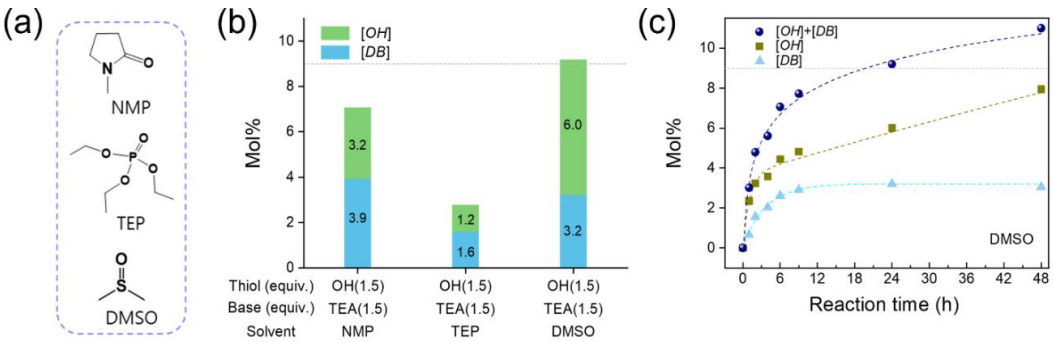

Figure 5.11. (a) Structure of solvents, (b) solvent dependency, and (c) time dependency (solvent : DMSO) of incorporated thiol and double bond

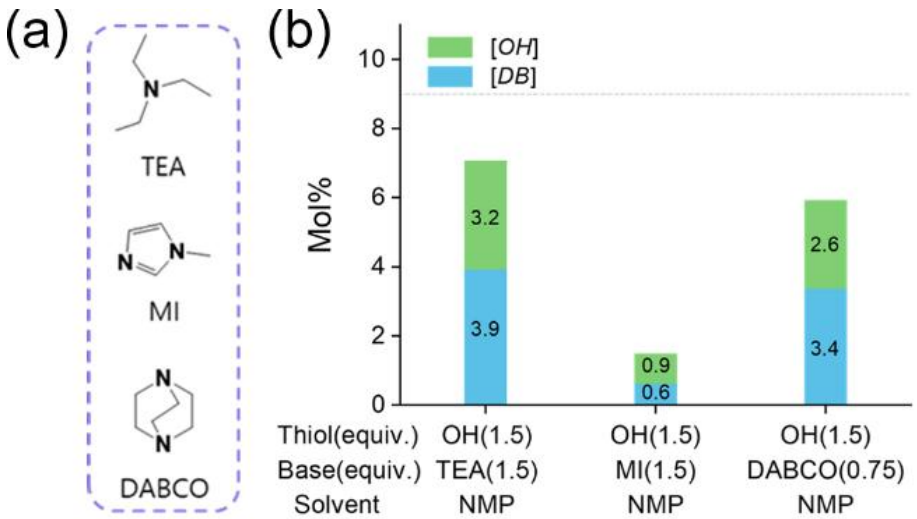

Figure 5.12. (a) Structure of bases and (b) base dependency of incorporated thiol and double bond

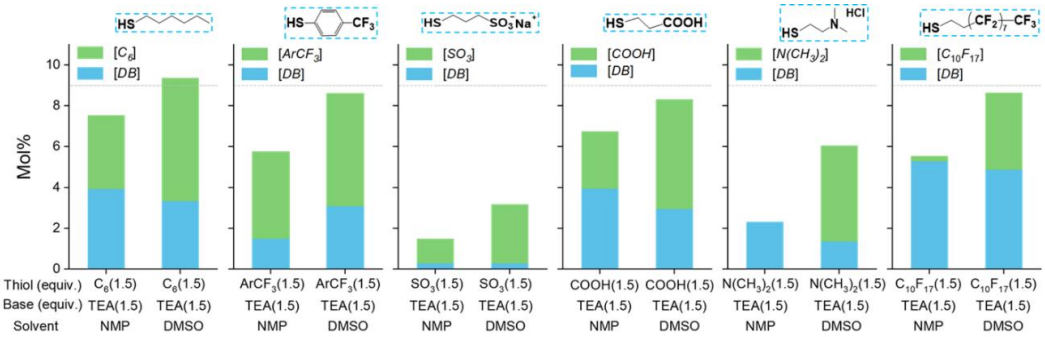

Figure 5.13. Thiol type and solvent dependency of incorporated thiol and double bond

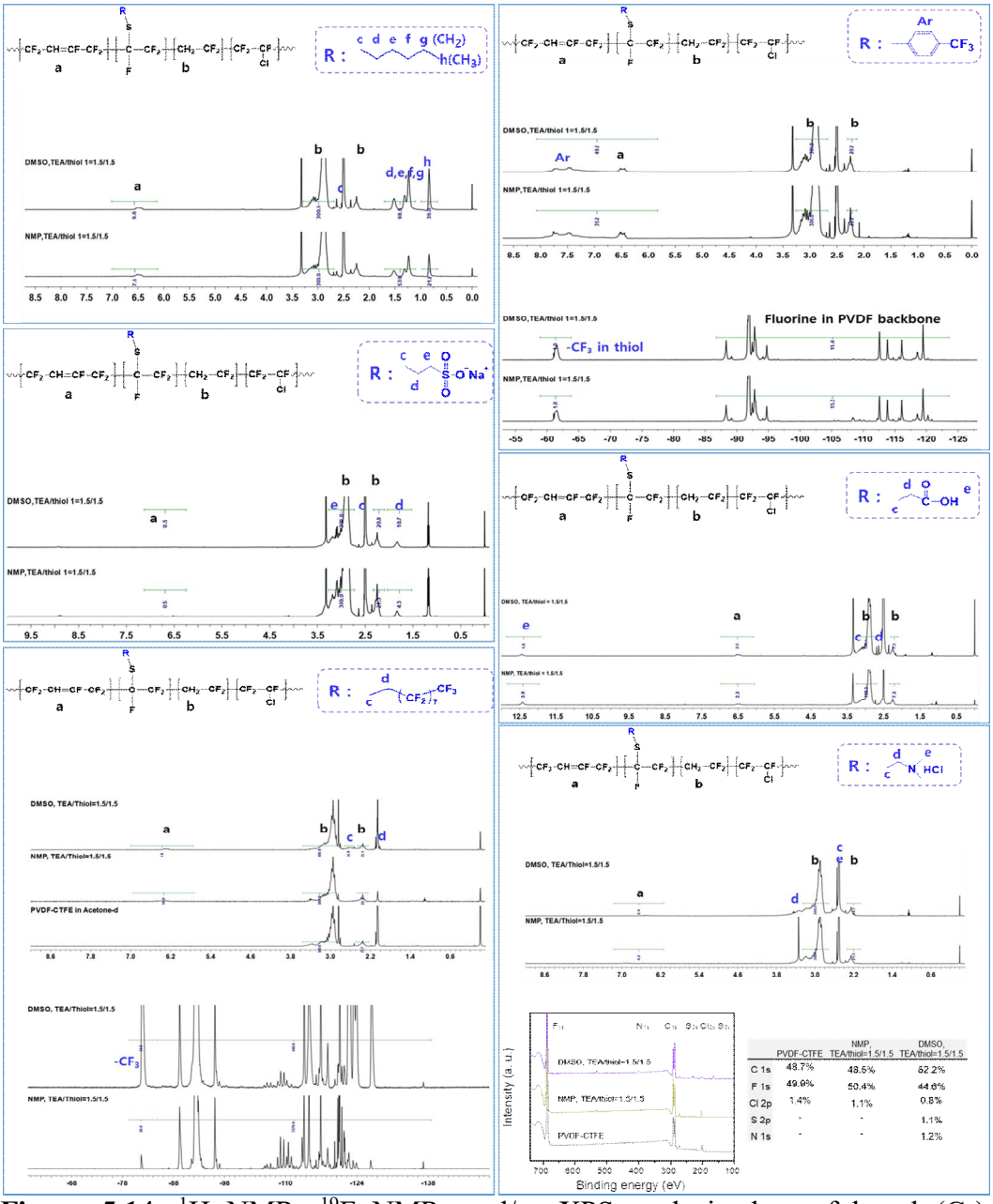

Figure 5.14. ^{1}H NMR, ^{19}F NMR, and/or XPS analysis data of hexyl (C_6), (trifluoromethyl)aryl ($ArCF_3$), sulfonate (SO_3), carboxyl (COOH), dimethylamino ($N(CH_3)_2$), and perfluorinated ($C_{10}F_{17}$) group incorporated P(VDF-CTFE)s

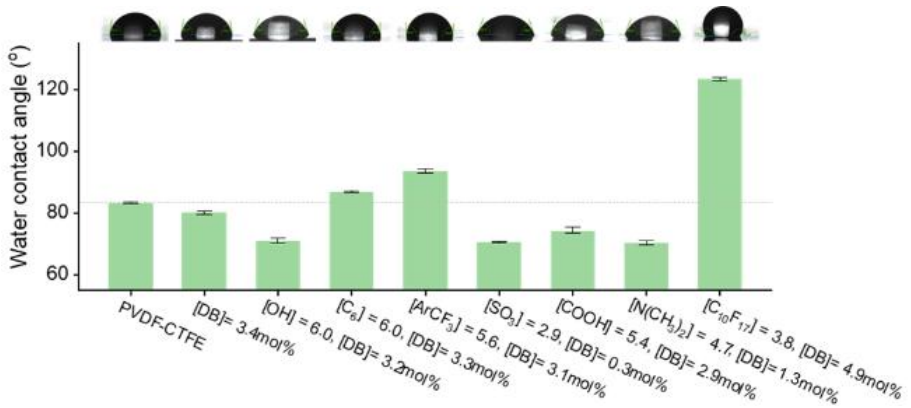

Figure 5.15. Water contact angles of pristine and thiol-modified P(VDF-CTFE) films

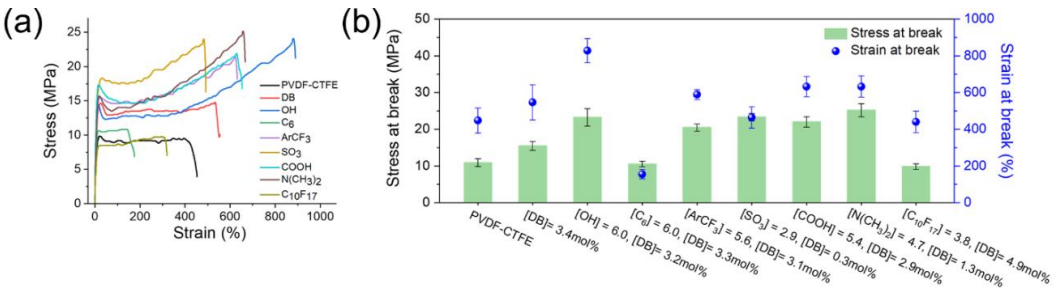

Figure 5.16. (a) Stress–strain curves and (b) mechanical properties of pristine and thiol-modified P(VDF-CTFE) films

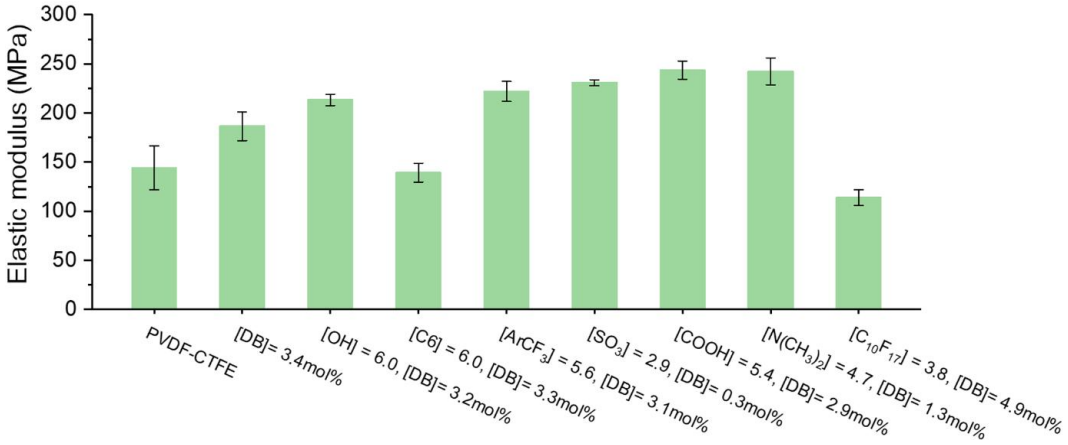

Figure 5.17. Elastic modulus of polymer films containing varied functional groups

Chapter 6

Access to Fluorinated Polymer Surfaces with Outstanding Mechanical Property, High Optical Transparency, and Low Surface Energy via Nonafluoro-tert-Butyl Group

Introduction

6.1. Introduction

Fluorinated compounds have received much attention because of their thermal and chemical inertness,[1] low refractive index,[2] and water and oil repellency,[3] finding applications in the fields of water treatment,[4] self-cleaning coatings,[1,5] fuel cell membranes,[6] and biomedical devices.[7] These advantageous properties originate from the low polarizability of fluorine atoms and the high strength of C–F bonds, which can substitute C–H bonds with only small conformational changes.[8,9] Consequently, the use of fluoro-functionalization (or fluorination) to enhance material properties has attracted much interest.

According to the synthetic approach, the fluorination of common polymers can be divided into (i) copolymerization with fluorinated monomers,[10,11] (ii) direct functionalization using fluorination agents such as F_2 and HF,[12–16] and (iii) the introduction of fluorinated functional moieties.[17,18] Copolymerization is a general method of introducing fluoro-functionalities into polymers owing to its ease of implementation and cost-effectiveness;[19,20] however, the scope of fluorinated monomers is restricted.[21,22] On the other hand, direct fluorination is applicable to most organic compounds but involves the use of reagents posing acute toxicity and environmental problems,[23–25] e.g., F_2,[12,13] HF,[14,15]

and BF_3.[16] In contrast, the introduction of fluorinated moieties offers the advantages of mild reaction conditions, applicability to a wide range of polymers, and control over functionality (or selective functionalization) in the case when the polymer has certain reaction sites.[9,17,18,22] However, this technique still suffers from drawbacks of complex fluorination conditions and the limited scope of fluorinated moieties.[9]

Owing to its fluorine-rich bulky structure and low surface energy, the nonafluoro-*tert*-butyl (NFtB) group has received much attention as a fluorinated moiety, particularly in the fields of lithium batteries,[26] functional magnetic resonance imaging,[27–29] and surfactants.[30,31] Nonafluoro-*tert*-butanol (NFtB–OH) exhibits an acidity comparable to that of carboxylic acids (pK_a = 5.2)[32] and therefore easily reacts with other functional groups to afford functionalized products with high conversion efficiencies under mild reaction conditions. In addition, the corresponding derivatives show no acute *in vivo* toxicity and no evidence of retention in organs,[27,30] whereas linear long-chain perfluoroalkyl acids and their precursors pose a potential environmental risk due to their bioaccumulation in wildlife and long-term biopersistence.[20,33] Despite these attractive features of the NFtB group, studies of using NFtB group as polymer fluorination agent remain scarce.

Herein, copolymers of methyl methacrylate (MMA) and 2-hydroxyethyl

methacrylate (HEMA) were prepared to model the fluorination of common polymers via NFtB group incorporation. The hydroxyl group of HEMA acted as an active site for NFtB moiety attachment, which allowed the fluorine content of the polymer to be controlled by MMA:HEMA ratio adjustment. The developed fluorination could be efficiently performed under mild conditions and enhanced the mechanical, optical, and surface properties of thin films produced from fluorinated polymers. Thus, the results of this study pave the way to the efficient fluorination of various polymers and the production of polymer films with the desired properties.

6.2. Experimental

Materials

MMA (99%), HEMA (97%), tetrahydrofuran (THF, 99.9%), *N*,*N*-dimethylformamide (DMF, 99.8%), *N*-methyl-2-pyrrolidone (NMP, 99.5%), methyl ethyl ketone (MEK, 99%), poly(methyl methacrylate) (PMMA, M_w = 350 000), basic alumina, and NMR solvents were purchased from Sigma-Aldrich. NFtB–OH (99%), triphenylphosphine (Ph_3P, 99%), diisopropyl azodicarboxylate (DIAD, 94%), and 2,2,3,3,4,4,4-heptafluorobutyl methacrylate (HFBMA, 97%) were purchased from Alfa Aesar. α,α'-Azobis(isobutyronitrile) (AIBN, 98%) was obtained from Junsei Chemical Co., Ltd. and recrystallized from methanol prior to use. Reaction monomers were purified using an alumina column, and other chemicals were used without further purification. All aqueous solutions were prepared using Milli-Q purified water (Millipore) with a resistivity of 18.2 MΩ cm.

Synthesis of MMA-HEMA copolymers and Fluorination

MMA-HEMA copolymers were prepared by free-radical polymerization. A round-bottom flask with a magnetic stirring bar was charged with NMP (50 mL)

and an MMA:HEMA mixture of the designated composition (8.0 g), and polymerization was performed at 60 °C for 18 h under N_2 using AIBN (2 wt%) as an initiator. The obtained products were precipitated by pouring the reaction mixture into excess water, washed with ethanol twice, and vacuum-dried at 50 °C. The NFtB group was introduced into P(MMA-co-HEMA) copolymers via the Mitsunobu reaction between HEMA hydroxyl groups and NFtB–OH, and the resulting copolymers containing 2-(nonafluoro-*tert*-butoxy)ethyl methacrylate (NFtBEMA) and MMA were denoted as NFtB-#s, where # is the molar content (feed, mol%) of HEMA in the monomer mixture. Typically, P(MMA-co-HEMA) (0.76 g, 2.83 mM_{OH}) and Ph_3P (4.53 mM, 1.6 equiv) were added to DMF:THF (20 mL; 1:1, v/v) under N_2. The solution was cooled to 0 °C and dropwise supplemented with DIAD (4.53 mM, 1.6 equiv) over 10 min. The resulting mixture was allowed to stir in an ice bath for 5 min, and NFtB–OH (5.66 mM, 2.0 equiv) was dropwise added over 5 min. The solution was heated at 50 °C for 24 h and poured into excess brine. The precipitate was sequentially washed with deionized (DI) water, diethyl ether, and ethanol, and vacuum-dried at 50 °C to afford the NFtB-# samples as a white powdery solid. The 6-different samples such as NFtB-5.8, NFtB-9.4, NFtB-19.7, NFtB-38.1, NFtB-57.4, and NFtB-77.3 were prepared according to the identical synthetic procedure.

Polymer Characterization

The structures of monomers and polymers were confirmed by NMR spectroscopy (Bruker AVANCE 500, 500 MHz for ^{1}H, 471 MHz for ^{19}F) using deuterated solvents (acetone-d_6 and dimethyl sulfoxide-d_6) and tetramethylsilane (TMS) as an internal standard. Chemical shifts were recorded in ppm relative to the signal of TMS at room temperature. Polymer molecular weights and molecular weight distributions (PDI) were measured at 40 °C by gel permeation chromatography (GPC; Waters 2690, Waters Corporation, USA) using a differential refractometer as a detector, THF as a solvent, and monodisperse polystyrene as a standard. The number average molecular weights (M_n) of NFtB-5.8, NFtB-9.4, NFtB-19.7, NFtB-38.1, NFtB-57.4, and NFtB-77 were 80,000, 77,900, 122,000, 100,000, 85,800, and 72,200, respectively and their PDI values were ranged in 1.5-3.1. Fourier transform infrared (FT-IR; FT/IR-4100, JASCO, Japan) spectra recorded by the KBr pellet method were obtained by the co-addition of 32 scans with a resolution of 2 cm^{-1}. Glass transition temperatures (T_gs) were determined by differential scanning calorimetry (DSC; Q1000 , TA Instruments) measurements, which were conducted in the temperature range of −50 to 200 °C at a heating rate of 10 °C min^{-1} after 5-min initial heating at 100 °C. Thermogravimetric analysis (TGA; Q5000, TA Instruments) was performed to determine the thermal properties from room temperature (RT) to 600 °C at a

heating rate of 10 °C·min^{-1} under N_2 purging.

Surface Property Measurement

Silicon wafers and glass slides preliminarily cleaned with detergent (Deconex) were sequentially ultrasonicated in water, acetone, and ethanol. Polymers were spin-coated with 2 wt% solutions in MEK at a rate of 2000 rpm for 60 s, and dried in air for 2 h at 120 °C. Surface roughness was determined by contact-mode atomic force microscopy (Bruker Nanoscope) using a silicon probe (RTESP-300, Bruker). Analysis was conducted at a scan rate of ~1 Hz for an area of 5 μm × 5 μm. X-ray photoelectron spectroscopy (XPS) analysis was performed using an UHV multipurpose surface analysis system (AXIS NOVA, KRATOS, UK). Photoelectron spectra were acquired in the constant-analyzer-energy mode using a pass energy of 40 eV and a step of 0.1 eV at a takeoff angle of 90°. Two-dimensional grazing incidence wide-angle X-ray diffraction (2D GIWAXD) analysis was performed using a high-power X-ray beam (10.0833 keV, beam size ≤ 0.5 mm^2) from a synchrotron radiation source (3C beamline, Pohang Accelerator Laboratory, Korea) at a sample-to-detector distance of 210.9253 mm. The detection system was equipped with a two-dimensional MarCCD X-ray detector. Scattering angles were corrected according to the positions of X-ray beams reflected from the silicon substrate interface with changing incidence angle

and referenced to pre-calibrated silver behenate ($AgC_{22}H_{43}O_2$). Mechanical properties (such as elastic modulus and indentation hardness) were measured using the nanoindentation method (UNHT indentation/scratch tester, Anton Paar). Polymer films prepared by spin-coating (1000 rpm, 60 s) of 10 wt% MEK solutions onto pre-cleaned silicon wafers [34] were annealed at 120 °C for 2 h. Analysis was carried out at a constant loading/unloading rate of 100 mN min^{-1} (maximum load = 50 mN), and each property was estimated from unloading curves using the Oliver-Pharr model.[35] Measurements were conducted 10 times on two different films, and the results were reported as averages ± standard errors. The advancing and receding (dynamic) contact angles of water and diiodomethane (DIM) were measured at room temperature and ambient relative humidity using a goniometer and drop shape analysis software (Krüss DSA 100). Measurements were performed by dispensing or aspiring liquid onto or from the polymer surface, and contact angles in the equilibrium region were gathered. For each sample, contact angles were measured more than six times on three different films, and the values were averaged. Ultraviolet–visible (UV–vis) transmittance spectra of PMMA and NFtB-#s coated glasses were recorded using a UV–vis spectrophotometer (V-650, JASCO, Japan) at wavelengths in the range of 300–750 nm.

Molecular Modeling

Electronic states were explored by quantum chemical calculations. Density functional theory was chosen as the calculation method in view of its reliability and adequate calculation cost.[36] Computations were performed using the algorithm embedded in Gaussian16 software.[37] In-polymer analogues of MMA and NFtBEMA were created by substituting a vinyl group for two methyl groups to analyze the local electronic states of the copolymer chain. The Kohn-Sham equation of the system was solved by a self-consistent procedure using the B3LYP hybrid functional and the 6-31G(d,p) basis set.[38–41] The rough initial molecular structure was built using Gaussview 6 modeling software [42] and subsequently converted to the ground-state structure using geometry optimization. In each step, the molecular structure was slightly transformed, and the total system energy was calculated and compared to that obtained in the previous step. This iteration was continued until the energy gradient reached 1.5×10^{-5} Hartree/Bohr. The final geometry was considered as a ground-state structure and used for the following analysis. With the obtained wavefunctions and orbital eigenvalues in hand, atomic charges were calculated using the Merz-Singh-Kollman scheme [43,44] and used to determine the dipole moment and electrostatic potential.

6.3. Results and discussion

The NFtB moiety was incorporated into P(MMA-HEMA) under mild conditions via the Mitsunobu reaction between HEMA hydroxyl groups and NFtB–OH in DMF-THF mixture solvent at 50 °C (Figure 6.1a).[29,45,46] The content of incorporated NFtB groups was controlled by adjusting the MMA:HEMA feed ratio in the first polymerization step (Table 6.1), and almost quantitative conversion (>98.0%) was obtained in all cases. Figure 6.1b displays the ^{1}H NMR spectrum of P(MMA-HEMA) and that of the corresponding fluorinated sample (NFtB-38.1). In the former spectrum, peaks around 4.8 and 3.9 ppm were assigned to the –OH group (c) and the methylene group adjacent to it (a), respectively (Figure 6.1b). After fluorination, peaks (a) and (c) were replaced by the signals of the two methylene groups (e, f) attached to the NFtB group (4.4 and 4.2 ppm) (Figure 6.1b and 2). The MMA:NFtBEMA molar ratio determined from the integrals of the characteristic peaks of NFtBEMA (–OCH_2–, e and f) and MMA (–OCH_3, d) were identical to the MMA:HEMA molar ratios calculated from the ^{1}H NMR spectrum. This result indicated the quantitative yield of NFtB group incorporation and showed that the Mitsunobu reaction with NFtB–OH was ideal for the fluorination of the chosen polymer. The generation of a fluorinated ether group was also confirmed by the observation of one sharp peak at −70.7

ppm in the corresponding ^{19}F NMR spectrum (Figure 6.3).[28]

The structures of NFtB-38.1 and the corresponding P(MMA-HEMA) copolymer were further probed by FT-IR spectroscopy (Figure 6.1c). The spectra of both samples showed a strong C=O peak around 1730 cm^{-1}, attributable to the carbonyl groups of the methacrylate backbone. However, the characteristic broad peak of the hydroxyl group around 3500 cm^{-1} was only observed for P(MMA-HEMA), while the spectrum of P(MMA-NFtBEMA) featured several peaks of C–F bonds at 540, 730, 970, and 1307 cm^{-1}.[47,48] These results indicated the successful incorporation of NFtB moieties into P(MMA-HEMA), in line with NMR data.

The surface compositions of NFtB-# thin films were investigated by comparing the F/C ratios obtained from C 1s and F 1s X-ray photoelectron spectra. In C 1s spectra, the signals of C=O, C–O, and C–H/C–C moieties appeared at 289.1, 288.2, and 284.8 eV, respectively, while F 1s spectra featured a single C–F peak at 686.4 eV (Figure 6.4a). The F/C ratios of NFtB-# films, obtained from the areas of the above peaks by dividing the experimental values by an appropriate sensitivity factor (Figure 6.4b), increased with increasing NFtB content, reflecting the direct dependence of surface fluorine content on the copolymer ratio. The experimental F/C ratios of NFtB-19.7, -38.1, -57.4, and -77.3 were similar to or lower than the corresponding theoretical values, which indicated the similar

surface occupancies of carbon and fluorine atoms or rather the formation of carbon-enriched surfaces. It has been reported that functional groups with lower surface energies prefer to be located at the surface-air interface rather than inside the polymer film.[7,20,49,50] Particularly, linear fluorocarbon chains have strong tendency to migrate toward the surface due to their extremely lower surface energies.[51] For side-by-side comparison, P(MMA-HFBMA) copolymers with linear fluorocarbon tails ($–CF_2CF_2CF_3$) were synthesized (Figure 6.5a). The F/C ratios of the P(MMA-HFBMA) films were indicative of fluorine-enriched compositions over the whole range of copolymer ratios (Figure 6.5b). Even though the experimental values for low-NFtB-content films (e.g., NFtB-5.8 and NFtB-9.4) were somewhat higher than the theoretical ones, these differences were quite small (Figure 6.4b). As a result, compositional variances revealed that NFtB groups preferred to be present inside the films, contrary to the typical behavior of fluorinated moieties. This phenomenon was very interesting, as NFtB-#s contained numerous $–CF_3$ groups with the lowest surface free energy.[31,52]

To determine the cause of the unusual surface compositional variance of NFtB-#s, their intrinsic molecular properties such as electronic state and dipole moment were investigated by quantum chemical calculations. Figure 6.6 illustrates the ground-state molecular structures of MMA and NFtBEMA analogues and provides the corresponding electrostatic potential maps and dipole moments. On

account of the similar electronegativities of hydrogen and carbon, no noticeable charge localization was observed in the MMA analogue (Figure 6.6a) except for the carbonyl oxygen. However, charge localization was observed for the NFtBEMA analogue (Figure 6.6b) owing to the presence of a fluorinated pendant group. The highly electronegative fluorine atoms drew electron density from the neighboring atoms, rendering the remaining part electron-deficient. Figure 6.7 presents the calculated atomic charges, showing that upon NFtB group incorporation, the ethylene part became positively charged, while the pendant group exhibited a complex charge distribution reflecting the contributions of the electron-rich outer fluorine region and the electron-poor inner carbon region. The dipole moment of MMA was mostly affected by the ester group. Therefore, MMA had a small dipole moment of 1.77 D (Debye) slightly tilted in the carbonyl group direction. However, the combined contributions of ester and NFtB groups in the NFtBEMA analogue resulted in a relatively large (3.21 D) dipole moment that was oriented obliquely to the methacrylate backbone, unlike in the case of conventional fluorinated methacrylates bearing linear fluorocarbon pendant groups.[20,53–55] A fluorinated methacrylate with three linear-chain fluorocarbon units (HFBMA) was also examined for comparison (Figure 6.8), showing a dipole moment (2.67 D) larger than that of MMA but smaller than that of NFtBEMA. Moreover, owing to the strong electronegativity of the linear fluorocarbon chain,

this dipole moment was almost perpendicular to the backbone. In this case, fluorinated pendant groups tended to align on the surface and made it fluorine-enriched compared to the bulk, as has been reported elsewhere.[17,53–55] In NFtB-#s, however, the molecular interaction between the tilted moment vector and the big dipole moment magnitude due to the biased charge distribution could impede the alignment of the NFtB group perpendicularly to the surface. Therefore, we believe that the provided insights into the intrinsic electronic properties can well explain the unusual molecular arrangement of NFtBEMA units on the surface.

The unexpected polar nature of the NFtBEMA unit was also confirmed by GIWAXD analysis of NFtB-# films. Figure 6.9a shows a representative 2D GIWAXD diffractogram with a ring-shaped signal indicating the absence of a crystalline structure on the molecular scale. The effect of NFtBEMA content was quantified by analysis of the line profiles of q-values in the in-plane direction (Figure 6.9b). The q-values of all polymers were calculated from the maxima of broad peaks and converted to d-spacings (i.e., average intermolecular distances) using the relationship $d = 2\pi/q$. As displayed in Figure 6.9c, the q-value and d-spacing of the PMMA film equaled 0.96 and 6.56 Å, respectively, exceeding the values of NFtB-# films, in which case d-spacings ranged between 6.01 and 6.48 Å and decreased with increasing NFtB group content. Previous researches also reported that d-spacing values for PMMA were calculated to be 2.92 Å and 6.60 Å

from X-ray diffraction peaks and they arose from intramolecular interference and inter-chain distance, respectively. [56, 57]

Given that the NFtBEMA unit (11.58 Å) is much larger than the MMA unit (5.19 Å) (Figure 6.10), this behavior was unusual. Nevertheless, this phenomenon was fully supported by the results of surface composition analysis and molecular modeling, i.e., the polar nature of the NFtBEMA unit intensified the interactions between polymer chains and thus decreased the intermolecular distance. A drastic decrease in *d*-spacing was observed upon going from NFtB-5.8 to NFtB-38.1, but became less marked in other cases (i.e., upon going from NFtB-57.4 to NFtB-77.3). Therefore, the minimum NFtB content required for the formation of a well-packed molecular structure was concluded to equal 38 mol%.

The molecular packed structure of NFtB-#s revealed by GIWAXD analysis can strongly influence various film characteristics such as mechanical properties (hardness and modulus). As load- and depth-sensing nanoindentation are the most suitable methods of analyzing the mechanical properties of thin films,[58–60] nanoindentation measurements were conducted to evaluate the near-to-surface mechanical properties of thin films with variable fluorinated group content. Figure 6.11a shows the typical load-displacement curves of PMMA, NFtB-77.3, and HFBMA-80 films, while the indentation modulus (EIT) and hardness (HIT) values calculated based on these curves are given in Figure 6.11b and 11c. The

EITs of NFtB-# films showed a definite compositional dependency, being similar to or slightly larger than that of PMMA (~5.3 GPa) below an NFtB group content of 40 mol% and significantly exceeding this value in the cases of NFtB-57.4 (6.6 GPa) and NFtB-77.3 (7.3 GPa) (Figure 6.11b).

This behavior might originate from the denser packing of polymer chains at elevated contents of high-dipole-moment NFtBEMA units, in line with the results presented above. On the other hand, the EITs of P(MMA-HFBMA) copolymers ranged from 5.3 to 6.1 GPa at HFBMA contents of 20–80 mol%, being only marginally dependent on this content. In contrast, HITs drastically decreased with increasing proportion of NFtBEMA units up to 38.1 mol%, whereas the values of NFtB-57.4 and NFtB-77.3 films were similar to and much higher than that of NFtB-38.1, respectively. As the HITs of P(MMA-HFBMA) decreased with increasing HFBMA content in the whole HFBMA content range (20–80 mol%) (Figure 6.11c), the fluorinated part probably facilitated HIT reduction, especially in the case of surface-segregated HFBMA units, as follows from the dependence of the F/C ratio on HFBMA content. Therefore, the different behaviors of NFtB-57.4 and NFtB-77.3 films were ascribed to the reduction of the influence of NFtB moieties on the surface, as these groups preferred to be located inside polymer films. Furthermore, the dense polymer structure could also contribute to this behavior difference, as discussed above. Notably, NFtB-77.3 film had larger HITs

than P(MMA-HFBMA) films at all copolymer ratios.

The wetting properties of NFtB-# films were investigated by water and DIM contact angle measurements, as shown in Figure 6.12a. The influence of surface roughness was negligible, as the surfaces of all samples were very flat (R_a < 3 nm). Compared to PMMA films, NFtB-# films (even those with NFtB unit contents as small as 5.8 and 9.4 mol%) featured higher water and DIM contact angles. The increase in contact angle with increasing NFtB unit content became less sharp starting from NFtB-38.1, and the difference between the contact angles of NFtB-57.4 and NFtB-77.3 was small. Still, NFtB-77.3 exhibited the highest water and DIM contact angles of 107.4° and 90.8°, respectively. Film surface energies were calculated from water and DIM contact angles by the Owens−Wendt−Rabel−Kaelble (OWRK) method (Figure 6.12b). The surface energy of PMMA was as high as 44 mN m^{-1}, however, the introduction of an even small amount of NFtBEMA units triggered a large decrease in surface energy (18.8 mN m^{-1} for NFtB-19.7). The values of NFtB-38.1, NFtB-57.4, and NFtB-77.3 were not very different, ranging from 14.0 to 15.8 mN m^{-1}. Although this trend was directly connected to that of contact angle change, it seemed not to reflect the effect of the polar NFtBEMA unit disclosed in previous sections (particularly that on XPS analysis). Surface energy featured the contributions of dispersive and polar parts (Table 6.2), with the polar part contribution (%)

reported to be very useful for interpreting intermolecular polar interactions.[61] The polar contributions of NFtB-#s decreased upon going from NFtB-5.8 to NFtB-19.7, increasing with increasing NFtB content in other cases. This behavior was well correlated with the dominant effect of polar NFtBEMA units on surface composition at high content, as reflected by the F/C ratios discussed above. Despite these results, the NFtB-77.3 film surface had an extremely low surface energy of 13.97 mN m^{-1}.

Figure 6.13 shows the transmittance spectra of NFtB-#- and PMMA-coated glass slides in the UV-vis region (300–750 nm). When slides were coated by polymers on one side, all NFtB-#-coated samples showed higher transmittances than bare and PMMA-coated ones in the whole UV-vis region (Figure 6.13a), which was attributed to the low refractive index of the fluorinated group.[2,5,11] The transmittance of NFtB-#-coated glass slides increased with increasing NFtB content, and the transmittances of NFtB-38.1-, NFtB-57.4-, and NFtB-77.3-coated slides were around 93%, exceeding that of PMMA (91%). Double-sided coating was more effective for enhancing transmittance, particularly in the case of samples with high NFtB contents, i.e., NFtB-38.1, NFtB-57.4, and NFtB-77.3 (Figure 6.13b). Interestingly, compared to that of PMMA-coated glass (92.4% at λ = 566 nm), the transmittance of NFtB-77.3-coated glass was significantly higher (96.0% at λ = 472 nm).

6.4. Conclusion

NFtB groups were successfully incorporated into P(MMA-HEMA) copolymers using the Mitsunobu reaction, and high conversions (>98%) were achieved despite the mild conditions. Copolymers with different NFtB group contents (NFtB-#, # = 5.8, 9.4, 19.7, 38.1, 57.4, and 77.3 mol%) were prepared by controlling the monomer feed ratio. XPS analysis showed that NFtB groups preferred to be located inside polymer films, contrary to the typical behavior of fluorinated moieties. This tendency was attributed to the effect of the NFtB group on the dipole moment (3.21 D for NFtBEMA, cf. 1.77 D for MMA analog). The average distances between NFtB-# molecules on the film decreased with increasing NFtB group content, indicating the formation of a packed molecular structure, which could be correlated with the outstanding mechanical properties of NFtB-77.3 thin films (EIT = 7.3 GPa, HIT = 234.5 MPa). Even though all NFtB-# films had low surface energies of 26–14 mN m^{-1}, the polar contribution to the surface energy of NFtB-# varied according to NFtB content. High optical transparency could be obtained by inclusion of the NFtB group, particularly for the glass slide coated with NFtB-77.3 on both sides (96% at λ = 472 nm). We believe that the described fluorination strategy can be used to create high-performance materials with desirable properties in both academia and industry.

6.5. References

[1] S. Pan, R. Guo, M. Björnmalm, J.J. Richardson, L. Li, C. Peng, N. Bertleff-Zieschang, W. Xu, J. Jiang, F. Caruso, *Nat. Mater.,* 2018, *17*, 1040–1047.

[2] W. Groh, A. Zimmermann, A. *Macromolecules,* 1991, *24*, 6660–6663.

[3] Y. Lu, S. Sathasivam, J. Song, C.R. Crick, C.J. Carmalt, I.P. Parkin, *Science,* 2015, *347*, 1132–1135.

[4] P. Kaner, A. V. Dudchenko, M.S. Mauter, A. Asatekin, *J. Mater. Chem. A,* 2019, *7*, 4829–4846.

[5] E.H. Sohn, H.S. Kang, J.C. Bom, J.W. Ha, S.B. Lee, I.J. Park, *J. Mater. Chem. A,* 2018, *6*, 12950–12955.

[6] K.A. Mauritz, R.B. Moore, *Chem. Rev.,* 2004, *104*, 4535–4585.

[7] D.J. Han, H.J. Heo, I.J. Park, H.S. Kang, S.G. Lee, S.-B. Lee, J.-C. Lee, E.-H. Sohn, *ACS Appl. Polym. Mater.,* 2020, *2*, 178–188.

[8] W. Yao, Y. Li, X. Huang, *Polymer,* 2014, *55*, 6197–6211.

[9] E.H. Discekici, A. Anastasaki, R. Kaminker, J. Willenbacher, N.P. Truong, C. Fleischmann, B. Oschmann, D.J. Lunn, J. Read De Alaniz, T.P. Davis, C.M. Bates, C.J. Hawker, *J. Am. Chem. Soc.,* 2017, *139*, 5939–5945.

[10] S. Banerjee, B. V. Tawade, V. Ladmiral, L.X. Dupuy, M.P. Macdonald, B. Améduri, *Polym. Chem.,* 2017, *8,* 1978–1988.

[11] Y.G. Ma, E.H. Sohn, J. Choi, D.W. Kim, J.S. Kim, D.S. Lee, *Langmuir,* 2018, *34*, 11850–11856.

[12] K. Sung, R.J. Lagow, *J. Am. Chem. Soc.,* 1995, *117*, 4276–4278.

[13] J.H. Lee, K.H. Kim, M. Choi, J. Jeon, H.J. Yoon, J. Choi, Y.S. Lee, M. Lee, J.J. Wie, *Nano Energy,* 2019, *66*, 104158.

[14] T. Fuchigami, S. Inagi, *Chem. Commun.,* 2011, *47,* 10211–10223.

[15] T. Fuchigami, S. Inagi, Recent Advances in Electrochemical Systems for Selective Fluorination of Organic Compounds. *Acc. Chem. Res.,* 2020, *53,* 322–334.

[16] M. Lienhard, I. Rushkin, G. Verdecia, C. Wiegand, T. Apple, L. V. Interrante,. *Am. Chem. Soc.,* 1997, *119*, 12020–12021.

[17] J.S. Chung, B.G. Kim, E.H. Sohn, J.C. Lee, *Macromolecules,* 2010, *43*, 10481–10489.

[18] Y. Ogura, M. Takenaka, M. Sawamoto, T. Terashima, *Macromolecules,* 2018, *51*, 864–871.

[19] H.J. Heo, I.J. Park, S.G. Lee, J.W. Ha, S.B. Lee, E.H. Sohn, *Green Chem.,* 2018, *20*, 502–505.

[20] E.H. Sohn, J.W. Ha, S.B. Lee, I.J. Park, *Langmuir,* 2016, *32*, 9748–9756.

[21] A. Hirao, K. Sugiyama, H. Yokoyama, *Prog. Polym. Sci.,* 2007, *32,* 1393–1438.

[22] S. Tan, J. Li, G. Gao, H. Li, Z. Zhang, *J. Mater. Chem.,* 2012, *22*, 18496–18504.

[23] J.J. Reisinger, M.A. Hillmyer, *Prog. Polym. Sci.,* 2002, *27*, 971–1005.

[24] A.P. Kharitonov, *Prog. Org. Coat.,* 2008, *61*, 192–204.

[25] Y. Dong, Z. Wang, C. Li,. *Commun.,* 2017, *8*, 1–5.

[26] L. Qiao, Z. Cui, B. Chen, G. Xu, Z. Zhang, J. Ma, H. Du, X. Liu, S. Huang, K. Tang, S. Dong, X. Zhou, G. Cui, *Chem. Sci.,* 2018, *9*, 3451–3458.

[27] Z.-X. Jiang, X. Liu, E.-K. Jeong, Y.B. Yu, *Angew. Chem. Int. Ed.,* 2009, *48* , 4755–4758.

[28] I. Tirotta, A. Mastropietro, C. Cordiglieri, L. Gazzera, F. Baggi, G. Baselli, M. Grazia Bruzzone, I. Zucca, G. Cavallo, G. Terraneo, F. Baldelli Bombelli, P. Metrangolo, G. Resnati, *J. Am. Chem. Soc.,* 2014, *136*, 8524–8527.

[29] C.M. Tressler, N.J. Zondlo, *Biochemistry,* 2017, *56,* 1062–1074.

[30] S. Decato, T. Bemis, E. Madsen, S. Mecozzi, *Polym. Chem.,* 2014, *5*, 6461–6471.

[31] W.A. Zisman, Advances in Chemistry; American Chemical Society, 1964; Vol. 43, p. 1.

[32] R. Filler, R.M. Schure, *J. Org. Chem.,* 1967, *32*, 1217–1219.

[33] X.Z. Lim, *Nature,* 2019, *566*, 26–29.

[34] H. Chakraborty, A. Sinha, N. Mukherjee, D. Ray, P. Protim Chattopadhyay,

Mater. Lett., 2013, *93*, 137–140.

[35] W.C. Oliver, G.M. Pharr, *J. Mater. Res.,* 1992, *7*, 1564–1583.

[36] K.B. Lipkowitz, D.B. Boyd, *Reviews in Computational Chemistry 6*; Wiley Online Library, 1995.

[37] M.J. Frisch, G.W. Trucks, H.B. Schlegel, G.E. Scuseria, M.A. Robb, J.R. Cheeseman, G. Scalmani, V. Barone, G.A. Petersson, H. Nakatsuji, X. Li, M. Caricato, A. V Marenich, J. Bloino, B.G. Janesko, R. Gomperts, B. Mennucci, H.P. Hratchian, J. V Ortiz, A.F. Izmaylov, J.L. Sonnenberg, D. Williams-Young, F. Ding, F. Lipparini, F. Egidi, J. Goings, B. Peng, A. Petrone, T. Henderson, D. Ranasinghe, V.G. Zakrzewski, J. Gao, N. Rega, G. Zheng, W. Liang, M. Hada, M. Ehara, K. Toyota, R. Fukuda, J. Hasegawa, M. Ishida, T. Nakajima, Y. Honda, O. Kitao, H. Nakai, T. Vreven, K. Throssell, J.A. Montgomery Jr., J.E. Peralta, F. Ogliaro, M.J. Bearpark, J.J. Heyd, E.N. Brothers, K.N. Kudin, V.N. Staroverov, T.A. Keith, R. Kobayashi, J. Normand, K. Raghavachari, A.P. Rendell, J.C. Burant, S.S. Iyengar, J. Tomasi, M. Cossi, J.M. Millam, M. Klene, C. Adamo, R. Cammi, J.W. Ochterski, R.L. Martin, K. Morokuma, O. Farkas, J.B. Foresman, D.J. Fox, Gaussian, Inc., Wallingford CT, 2016.

[38] W. Kohn, L.J. Sham, *Phys. Rev.,* 1965, *140*, A1133.

[39] A.D. Becke, *J. Chem. Phys.,* 1993, *98,* 5648–5652.

[40] C. Lee, W. Yang, R.G. Parr, *Phys. Rev. B,* 1988, *37*, 785–789.

[41] S.H. Vosko, L. Wilk, M. Nusair, *Can. J. Phys.,* 1980, *58*, 1200–1211.

[42] R. Dennington, T.A. Keith, J.M. Millam, GaussView Version 6. 2019.

[43] U.C. Singh, P.A. Kollman, *J. Comput. Chem.,* 1984, *5*, 129–145.

[44] B.H. Besler, K.M. Merz, P.A. Kollman, *J. Comput. Chem.,* 1990, *11*, 431–439.

[45] J.J. Kasper, J.E. Hitro, S.R. Fitzgerald, J.M. Schnitter, J.J. Rutowski, J.A. Heck, J.L. Steinbacher, *J. Org. Chem.,* 2016, *81*, 8095–8103.

[46] A.S.W. Lo, I.T. Horváth, *Green Chem.,* 2015, *17*, 4701–4714.

[47] D. Lin-Vien, N.B. Colthup, W.G. Fateley, J.G. Grasselli, T*he Handbook of Infrared and Raman Characteristic Frequencies of Organic Molecules*; Elsevier Science, 1991.

[48] H.J. Heo, D.J. Han, E.H. Sohn, *J. Fluor. Chem.,* 2019, *219*, 92–97.

[49] O. Daglar, E. Cakmakci, U.S. Gunay, G. Hizal, U. Tunca, H. Durmaz, *Macromolecules,* 2020, *53*, 2965–2975.

[50] F. Leroux, R.A. Bennett, D.F. Lewis, H.M. Colquhoun, *Macromolecules,* 2018, *51*, 3415–3422.

[51] B. Zuo, C. Li, Y. Li, W. Qian, X. Ye, L. Zhang, X. Wang, *Langmuir,* 2018, *34*, 3993-4003.

[52] A. Czajka, G. Hazell, J. Eastoe, *Langmuir,* 2015, *31*, 8205–8217.

[53] B.G. Kim, J.S. Chung, E.H. Sohn, S.Y. Kwak, J.C. Lee, *Macromolecules,*

2009, *42*, 3333–3339.

[54] K. Honda, M. Morita, H. Otsuka, A. Takahara, *Macromolecules,* 2005, *38*, 5699–5705.

[55] K. Honda, M. Morita, O. Sakata, S. Sasaki, A. Takahara, *Macromolecules,* 2010, *43*, 454–460.

[56] N. S. Murthy, S. T. Correale, H. Minor, *Macromolecules,* 1991, *24*, 1185–1189.

[57] S. Krimm, A. V. Tobolsky, *Text. Res. J.,* 1951, *21*, 805–822.

[58] J. Malzbender, J.M.J. Den Toonder, A.R. Balkenende, G. De With, *Mater. Sci. Eng. R,* 2002, *36*, 47–103.

[59] F. Mammeri, E. Le Bourhis, L. Rozes, C. Sanchez, *J. Mater. Chem.,* 2005, *15,* 3787–3811.

[60] A. Ferchichi, S. Calas-Etienne, M. Smaïhi, G. Prévot, P. Solignac, P. Etienne, *J. Mater. Sci.,* 2009, *44*, 2752–2758.

[61] E.H. Sohn, B.G. Kim, J.S. Chung, J.C. Lee, *J. Colloid Interface Sci.,* 2010, *343*, 115–12

Table 6.1. Monomer feed ratio and chemical compositions of polymers

Samples	Chemical composition (mol%) [a]		
	Feed (MMA/HEMA)	In P(MMA-HEMA) (MMA/HEMA)	In P(MMA-NFtBEMA) (MMA/NFtBEMA/HEMA)
NFtB-5.8	5/95	94.0 / 6.0	94.2 / 5.8 / 0.0
NFBt-9.4	10/90	89.5 / 10.5	90.6 / 9.4 / 0.0
NFtB-19.7	20/80	79.8 / 20.2	80.3 / 19.7 / 0.0
NFtB-38.1	40/60	61.6 / 38.4	61.8 / 38.1 / 0.1
NFtB-57.4	60/40	40.5 / 59.5	42.4 / 57.4 / 0.2
NFtB-77.3	80/20	22.3 / 77.7	21.2 / 77.3 / 1.5

[a)] Determined by ^{1}H NMR.

Table 6.2. Surface energy profiles of NFtB-#s

Samples	Surface energy (mN m^{-1}) [a)]			
	Dispersive part	Polar part	Polar contribution (%)	Total surface energy
NFtB-5.8	22.76	2.84	11.09	25.60
NFtB-9.4	20.34	2.02	9.03	22.36
NFtB-19.7	17.24	1.59	8.44	18.83
NFtB-38.1	14.25	1.54	9.75	15.79
NFtB-57.4	13.42	1.66	11.00	15.08
NFtB-77.3	12.35	1.63	11.67	13.97

[a)] Owens–Wendt–Rabel–Kaelble method

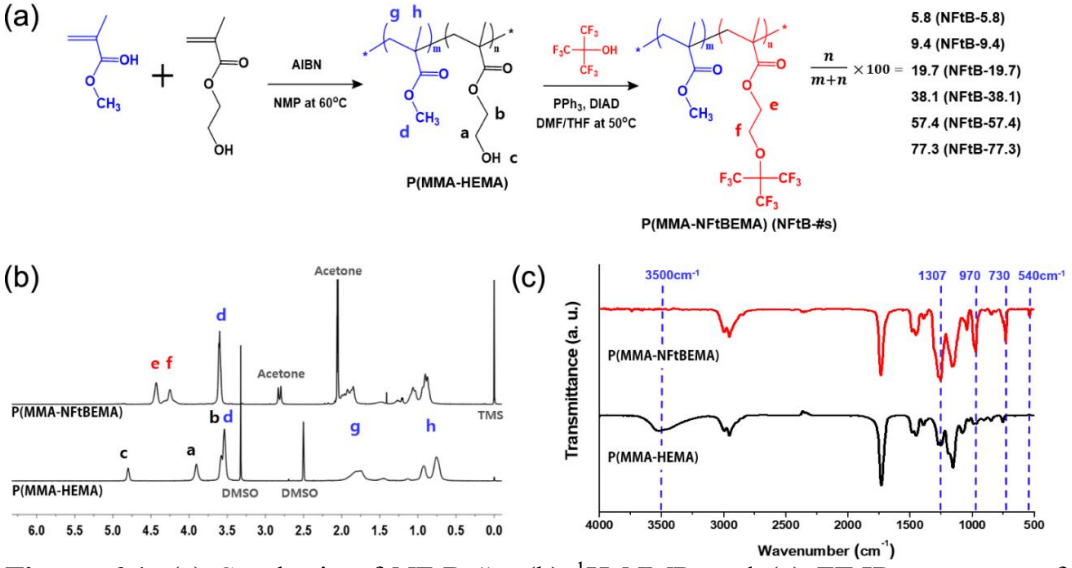

Figure 6.1. (a) Synthesis of NFtB-#s. (b) ^{1}H NMR and (c) FT-IR spectrum of NFtB-38.1 and the corresponding P(MMA-HEMA) copolymer

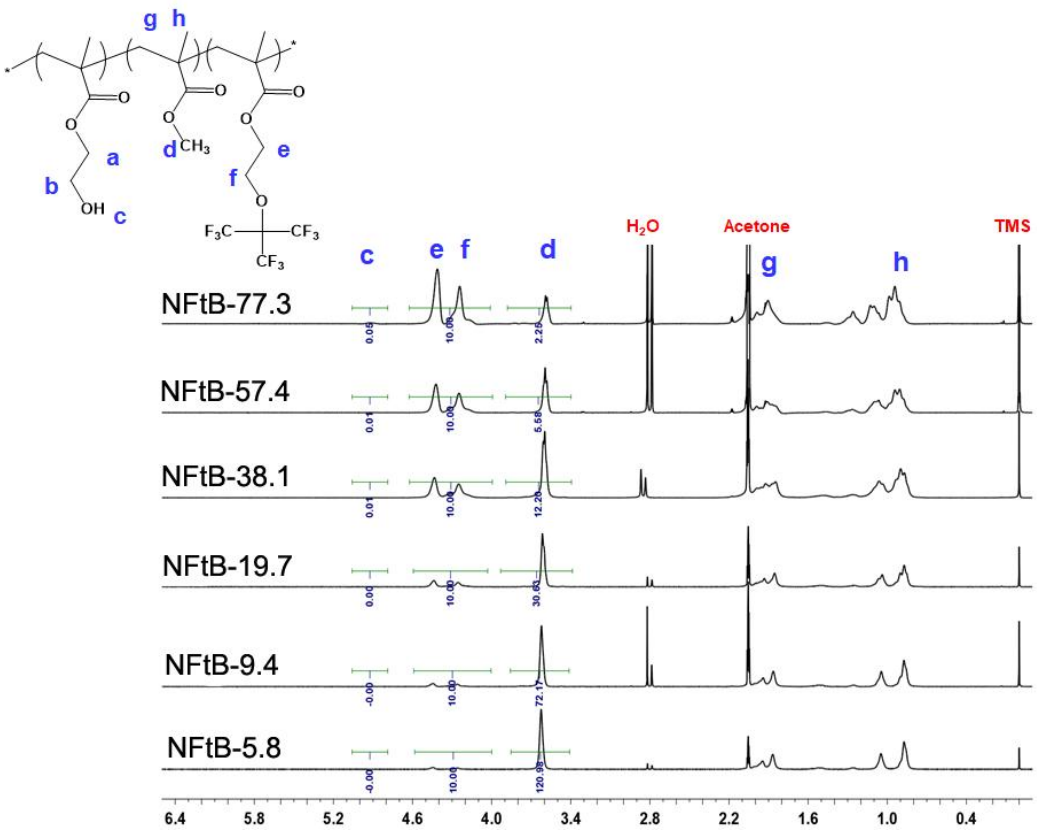

Figure 6.2. ^{1}H NMR spectra of NFtB-#s

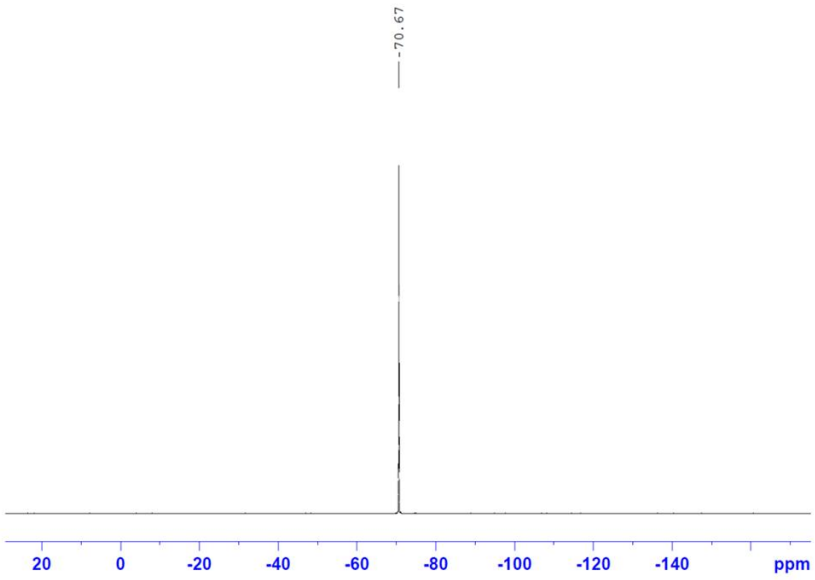

Figure 6.3. ^{19}F NMR spectrum of NFtB-77.3

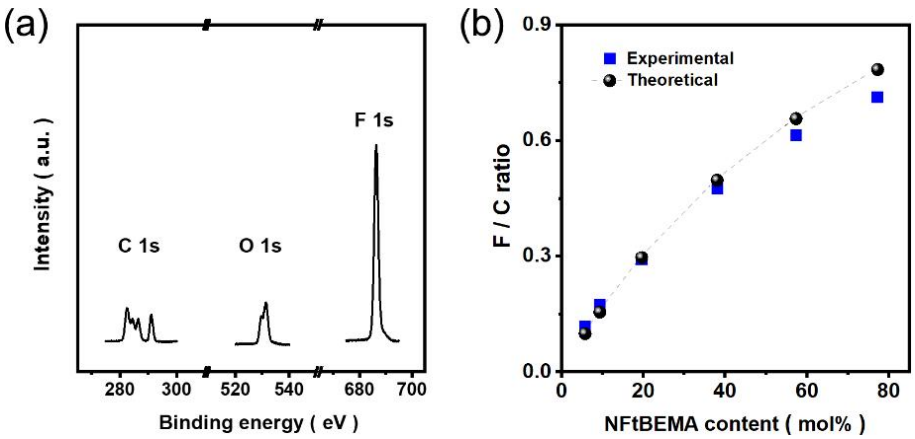

Figure 6.4. (a) Representative C_{1s}, O_{1s}, and F_{1s} spectra and (b) F/C ratios of NFtB-# film surfaces

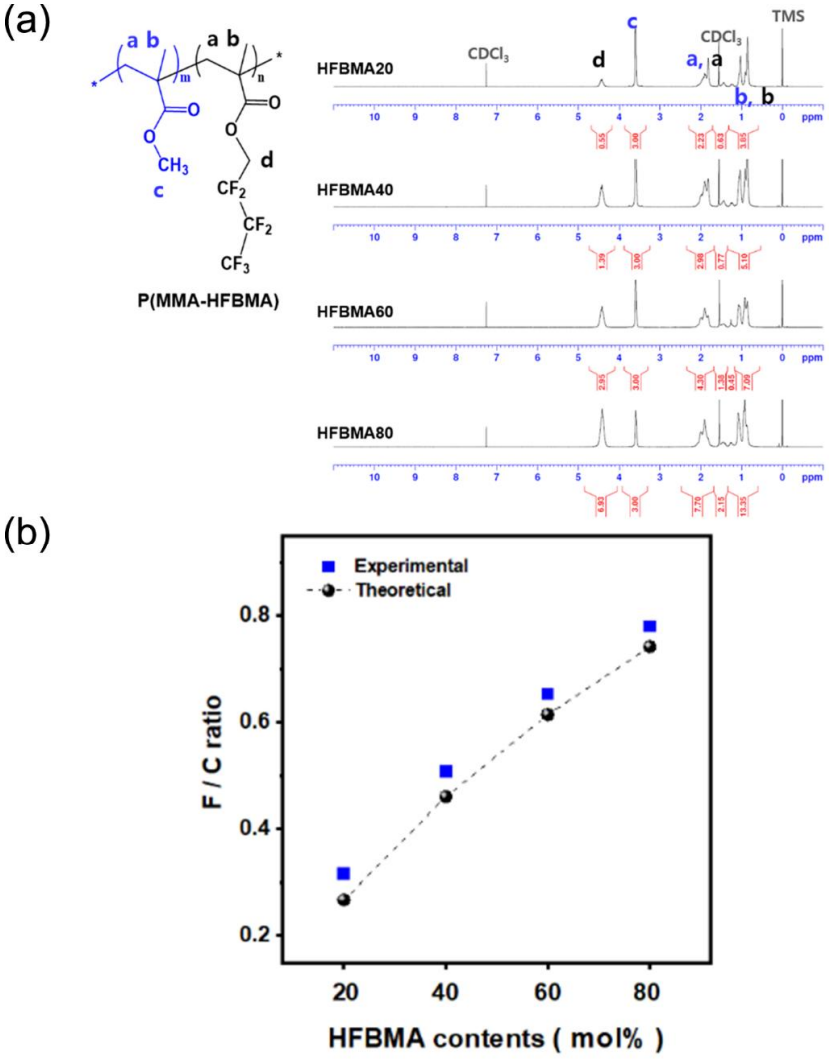

Figure 6.5. (a) ^{1}H NMR spectra of HFBMA-#s and (b) F/C ratios on their film surfaces

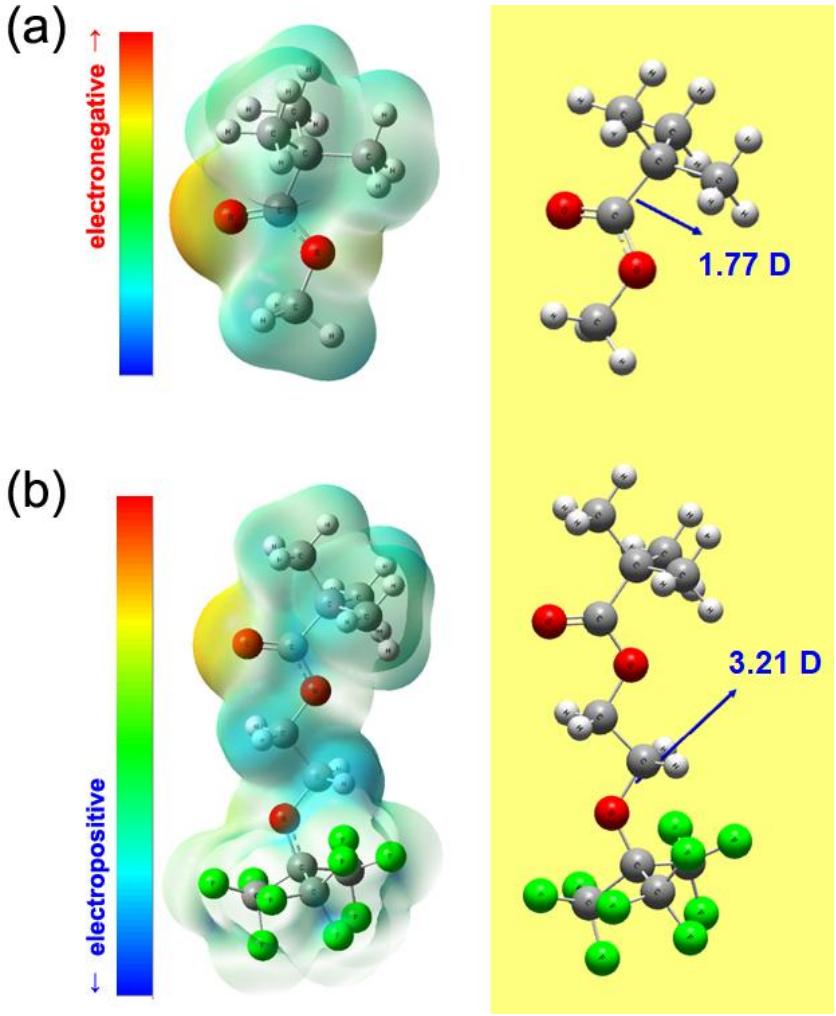

Figure 6.6. Electrostatic potential map (left) and atomic model (right) of in-polymer analogues of (a) PMMA and (b) NFtBEMA. The arrow indicates the direction of the net dipole moment

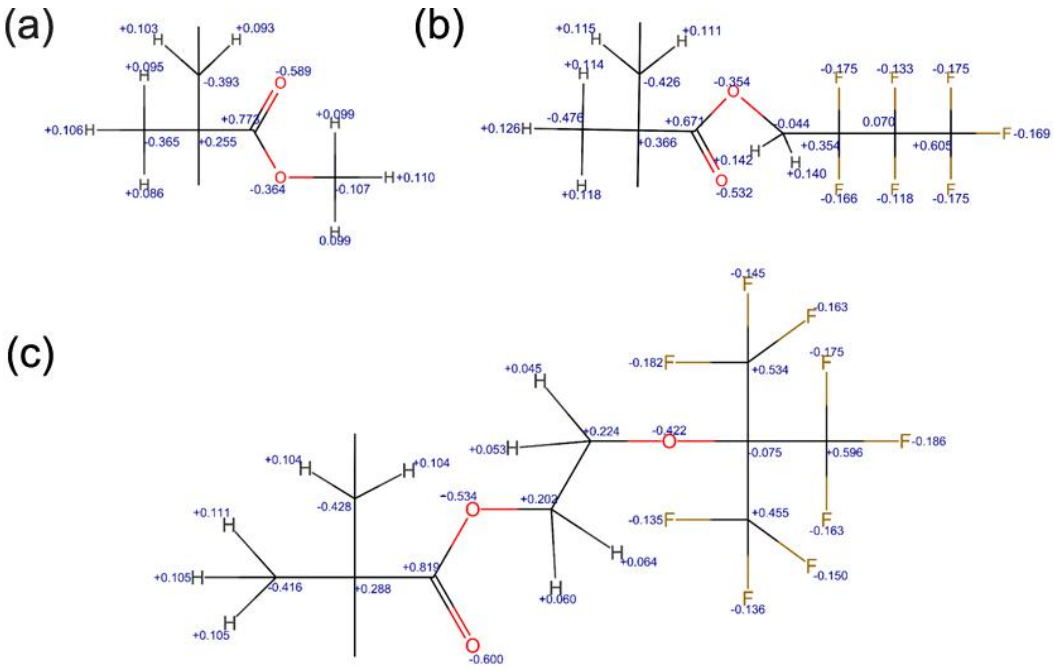

Figure 6.7. Merz-Kollman charge distribution of in-polymer analogues of (a) MMA, (b) HFBMA, and (c) NFtBEMA

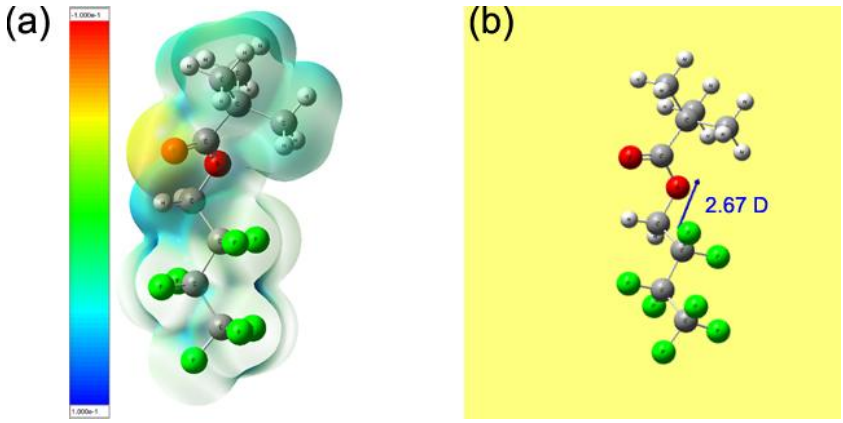

Figure 6.8. Electrostatic potential map and (b) atomic model structure of in-polymer analogue of HFBMA. The arrow indicates the direction of the net dipole moment

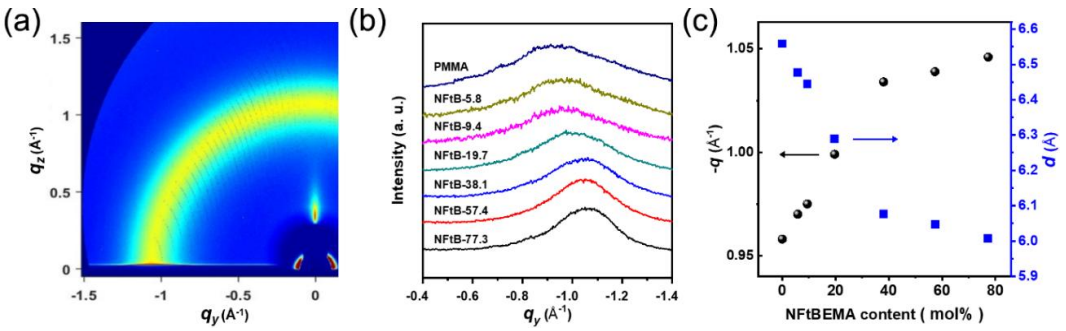

Figure 6.9. (a) Representative 2D GIWAXD diffractogram (NFtB-38.1) (b) Line profiles of the 2D GIWAXD diffractogram (in-plane direction) (c) *q*-values and *d*-spacings of NFtB-#s and PMMA

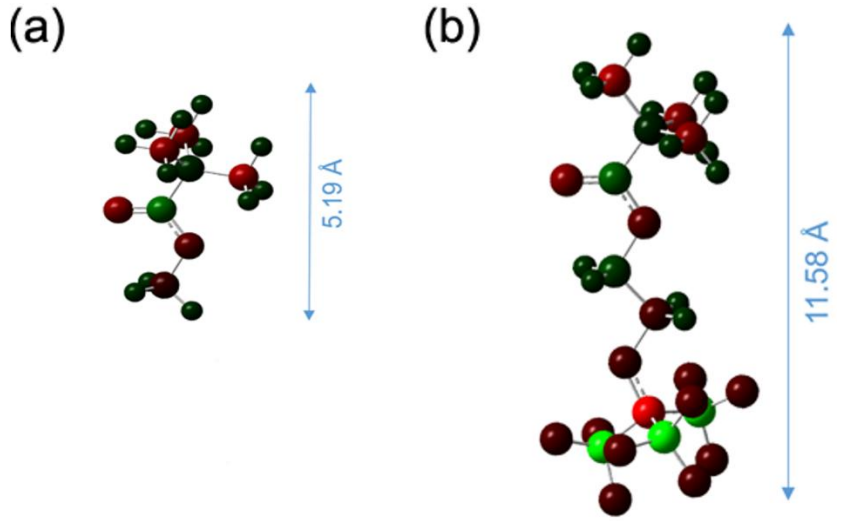

Figure 6.10. Molecular dimension of analogous (a) MMA and (b) NFtBEMA

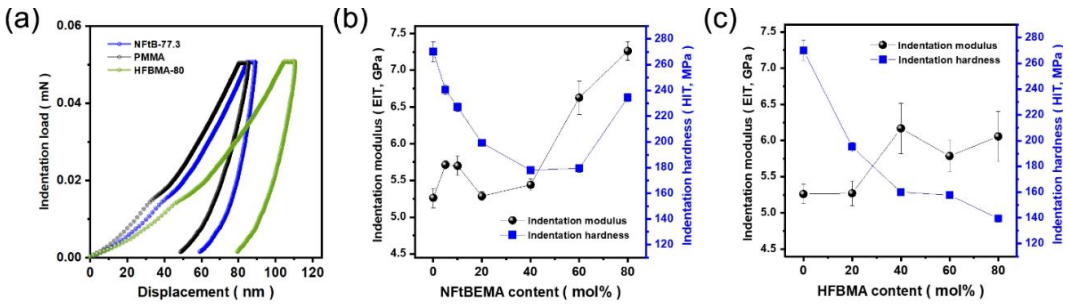

Figure 6.11. (a) Representative load-displacement curves of PMMA, NFtB-77.3, and HFBMA-80 films. Indentation modulus and indentation hardness profiles of (b) NFtB-# and (c) HFBMA-# films

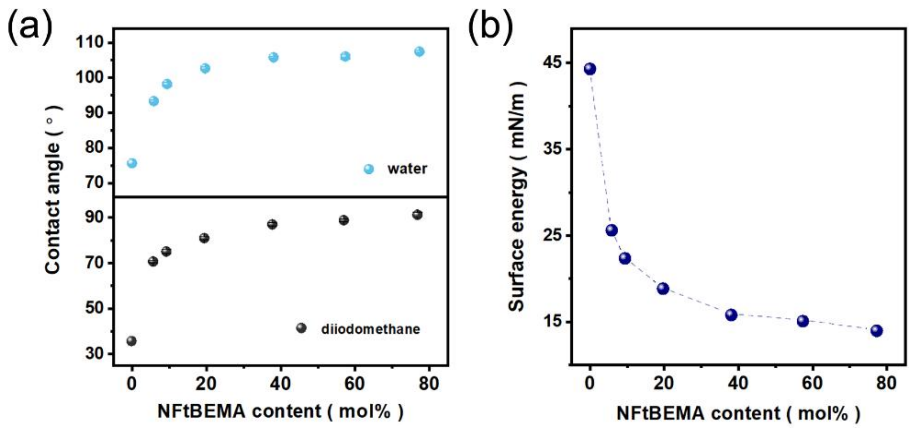

Figure 6.12. (a) Advancing water and DIM contact angles and (b) surface energies of NFtB-#s and PMMA

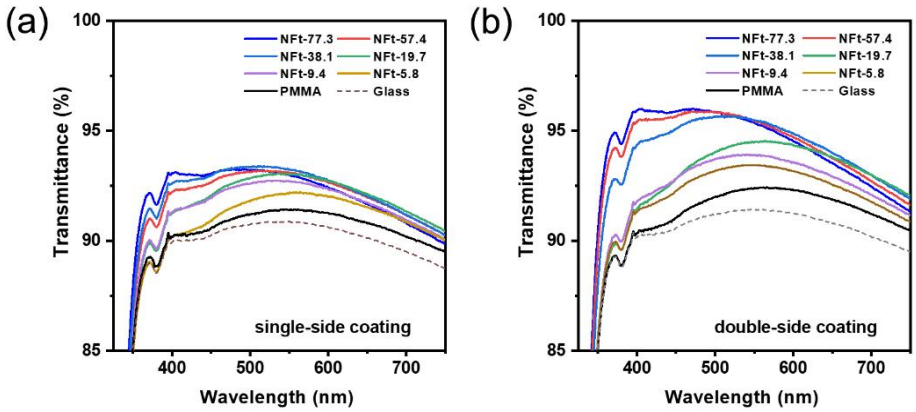

Figure 6.13. UV-vis transmittance spectra of a bare glass slide and glass slides coated with PMMA or NFtB-#s on one (a) or both (b) sides

초 록

본 연구에서는 불소계 고분자의 합성과 개질을 통해 새로운 불소계 고분자를 개발하였고 이의 바이오-메디컬, 수처리 분리막 및 코팅 소재로의 응용에 대하여 기술하였다. 첫째로, 짧은 측쇄 ($-CF_2CF_2CF_3$, $-CF_2CF_3$ 그리고 $-CF_3$) 를 가지는 불화 메타아크릴레이트를 비닐리덴플루오라이드와 클로로트리플루오로메틸렌의 공중합체에 그라프트 중합하여 세 가지의 신규 불소계 고분자를 합성하였다. 그라프트 중합은 원자 이동 라디칼 중합의 단일 과정으로 이루어졌으며, 합성된 고분자의 표면에너지는 그라프트된 단량체에 따라 11.1-18.7 mN m^{-1}의 범위에서 조절되었다. 혈장단백질인 알부민의 처리를 통해, $-CF_2CF_2CF_3$ 그룹을 가지는 고분자 표면에서는 5.6 ng cm^{-2}의 매우 낮은 피브리노겐 흡착량이 나타났으며, 혈소판 흡착 시험에서도 혈소판이 다른 표면보다 적게 붙는 결과가 관찰되었다. 피브리노겐과 혈소판의 흡착은 혈액을 응고시키는 주요한 원인이기 때문에, 본 연구에서 개발된 합성고분자 및 알부민 처리 기법은 혈액 적합성 표면으로 이용될 수 있다고 할 수 있다.

둘째로, 비닐리덴플루오라이드와 클로로트리플루오로메틸렌의 공중합체에 양이온성 고분자를 그라프트하여 항균성 및 항곰팡이성이 있는 불소계 고분자를 합성하였다. 4급 암모늄염과 4급 피리디늄 염을 가지는 단량체가 그라프트 되었으며, 합성된 고분자는 그람 양성균인 황색포도상구균과 그람 음성균인 대장균을 99.99% 이상 사멸시키는 것으로 확인되었다. 경제적 관점에서의 효율성 증대를 위해, 합성된 양이온성 고분자들은 같은 주쇄구조를 가지는 불소계 고분자인 폴리비닐리덴플루오라이드 와 블렌드되었다. 1중량% 혹은 5중량% 정도로 작은 양의 양이온성 고분자가

혼입되었음에도, 블렌드 필름은 대조군으로 이용된 폴리비닐리덴플루오라이드 필름보다 확연히 향상된 항균성 및 항곰팡이성을 보이는 것이 확인되었다. 또한 블렌드 필름의 기계적 특성 혹은 생체적합성은 대조군 필름보다 같거나 우수한 특성을 나타내었다.

셋째로, 양이온성 단량체와 그라프트된 고분자와, 양이온성 단량체와 양쪽이온성 단량체가 함께 그라프트된 이온성 고분자 두 종류가 폴리비닐리덴플루오라이드 기반으로 합성되어 분리막 첨가제로 이용되었다. 5중량% 혹은 10중량%의 각 이온성 고분자 첨가제가 블렌드되어 폴리비닐리덴플루오라이드 수처리 분리막이 제조되었으며, 물을 비용매로, 디메틸설폭사이드를 용매로 사용한 비용매유도 상분리법이 이용되었다. 제조된 분리막의 형태와 표면 거칠기, 친수성, 표면 전하 등의 물리 화학적 특성이 먼저 연구되었으며, 이어서 분리막의 방오성과 항균특성이 평가되었다. 결과적으로, 첨가제의 종류와 양에 따른 분리막의 물리 화학적 특성과 분리막의 방오성 및 항균성의 사이의 상관관계가 연구되었다. 제조된 분리막 중에서, 양쪽이온성 단량체가 포함된 고분자가 10중량% 포함된 분리막은 방오성 (투과회복률 ~ 100%) 및 항균성 (> 99.9%) 모두에서 뛰어난 성능을 나타내었다.

넷째로, 비닐리덴플루오라이드와 클로로트리플루오로메틸렌의 공중합체를 기능기를 도입하여 개질하였다. 다양한 기능기 (하이드록실, 알킬, 아릴, 술폰산, 카르복실, 아미노 및 과불화 작용기) 를 가지고 있는 티올을 비닐리덴플루오라이드 기반 주쇄에 도입하였으며, 이 반응은 3차 아민을 촉매로 이용하여 한 공정으로 진행되었다. 반응 시, 주쇄의 탈염산 및 이중결합 형성반응이 먼저 일어나며, 형성된 이중결합에 티올-마이클 첨가반응을 통하여 혹은 할로겐 원소의 친핵성 치환반응을 통하여 기능기가

주쇄에 도입된다. 시약의 투입량, 반응 시간, 용매 등의 반응 조건을 변화시켜 기능기가 주쇄에 도입되는 양을 조절할 수 있었으며, 티올의 종류를 바꾸어, 주쇄에 다양한 기능성을 도입할 수 있다는 것을 확인하였다. 또한, 만들어진 기능화 고분자를 이용하여 고분자 필름을 제조하였으며, 제조된 필름의 기계적 특성과 친수성 등의 특성이 연구되었다.

마지막으로, 가지형 불소계 그룹인 노나플루오로-*tert*-부틸(NFtB) 그룹이 메타아크릴계 고분자 주쇄에 도입되었고, 그 도입 효과에 대한 연구가 진행되었다. 먼저 라디칼 중합을 통하여 메틸메타아크릴레이트 와 2-하이드록시에틸메타아크릴레이트의 공중합체를 만들고, 공중합체의 하이드록실 그룹과 NFtB 알코올을 반응하여 NFtB 그룹을 도입하였다. 반응은 높지 않은 온도에서도 효율적으로 일어났으며, 도입되는 NFtB 그룹의 양은 선행 공중합체의 단량체의 비율을 통하여 조절하였다. 합성된 고분자는 필름으로 만들어졌고, 그 필름의 화학적 조성, 분자간 거리 및 기계적 특성 등이 도입된 불소계 그룹의 비율과 연관되어 조사되었다. 결과적으로, NFtB 그룹이 고분자 필름 특성에 상당한 영향을 준다는 것이 확인되었으며, NFtB 그룹이 포함된 단량체를 77.3 몰% 포함하는 고분자 필름의 경우 대조군으로 사용된 폴리메틸메타아크릴레이트보다 우수한 기계적 특성, 높은 투명성 및 낮은 표면 에너지를 나타내었다.

주요어: 불소고분자, 그라프트고분자, 폴리비닐리덴플루오라이드, 혈액 적합성, 항균성, 수처리 분리막, 기능화, 표면 특성

학 번 : 2017-29807